DYNAMICS OF THE ARECIBO RADIO TELESCOPE

Ramy Rashad

110030106

Department of Mechanical Engineering

McGill University

Montreal, Quebec, Canada

February 2005

Under the supervision of Professor Meyer Nahon

Abstract

The following thesis presents a computer and mathematical model of the dynamics of the tethered subsystem of the Arecibo Radio Telescope.

The computer and mathematical model for this part of the Arecibo Radio Telescope involves the study of the dynamic equations governing the motion of the system. It is developed in its various components; the cables, towers, and platform are each modeled in succession. The cable, wind, and numerical integration models stem from an earlier version of a dynamics model created for a different radio telescope; the Large Adaptive Reflector (LAR) system.

The study begins by converting the cable model of the LAR system to the configuration required for the Arecibo Radio Telescope. The cable model uses a lumped mass approach in which the cables are discretized into a number of cable elements. The tower motion is modeled by evaluating the combined effective stiffness of the towers and their supporting backstay cables. A drag model of the triangular truss platform is then introduced and the rotational equations of motion of the platform as a rigid body are considered. The translational and rotational governing equations of motion, once developed, present a set of coupled non-linear differential equations of motion which are integrated numerically using a fourth-order Runge-Kutta integration scheme. In this manner, the motion of the system is observed over time.

A set of performance metrics of the Arecibo Radio Telescope is defined and these metrics are evaluated under a variety of wind speeds, directions, and turbulent conditions. The general configurations of the Arecibo Radio Telescope, before and after its two major upgrades, are also compared.

Finally, a sensitivity analysis is carried out in order to identify which physical parameters of the system, if changed or redesigned, could improve the system's performance. The following six parameters are investigated: number of mainstay cables, tower radius (cable length), effective tower stiffness (number of backstay cables), platform mass, cable-platform attachment points, and mainstay cable properties.

Acknowledgements

I would like to sincerely thank Professor Meyer Nahon, my supervisor and mentor throughout this thesis. I would like to thank him for his excellent guidance and advice, as well as for his patience, motivation, and resolve. For always giving me the time of day, and for accepting to supervise my project, I am in his debt.

I would also like to extend my thanks to Dr. Steve Torchinsky, the Head of Astronomy at the Arecibo Observatory, for providing invaluable information needed throughout the course of this project.

Contents

Abstract **i**

Acknowledgments **iii**

List of Figures **vii**

List of Tables **x**

Chapter 1 Introduction **1**

1.1 Radio Telescopes …….…… 1

1.2 Radio Telescope Simulations……..……..2

1.3 Arecibo Construction Overview……... 3

1.4 Arecibo Upgrades…..…….. 5

1.5 LAR Model and Previous Work……... 7

1.6 Scope of Thesis……9

Chapter 2 The Arecibo Model **11**

2.1 Overview……...11

2.2 Lumped Mass Approach……... 12

2.3 Simulation Basics……. 14

2.3.1 State Vector……..……..14

2.3.2. Numerical Approach……..16

Chapter 3 Cable Model **19**

3.1 Cable Properties..……... 19

3.2 Coordinate Systems….…….…… 20

3.3 Cable Kinematics……...21

3.4 Cable Dynamics……22

3.4.1 Internal Forces…….. 22
3.4.2 External Forces…….. 26
3.4.3 Translational Equations of Motion…… 27

Chapter 4 Tower Model 29

4.1 Construction Details……..29
4.2 Tower Properties……...31
4.3 Effective Stiffness……32
4.3.1 Tower Contribution……33
4.3.2 Backstay Cable Contribution…… 34
4.3.3 Combined Effective Stiffness…… 36
4.3.4 Tower-Top Motion……36

Chapter 5 Platform Model 40

5.1 Construction Details……..40
5.2 Coordinate Systems…….. 41
5.3 Platform Properties……... 42
5.4 Cable Attachment Points…….. 45
5.5 Platform Drag……46
5.5.1 Factors Affecting Drag..…… 47
5.5.2 Side View of Truss……...……..48
5.5.3 Top View of Truss…… 51
5.5.4 Platform Angle of Attack……..……54
5.5.5 Drag of Gregorian System..……... 57
5.6 Translational Motion……..…59
5.7 Rotational Motion…… 60
5.7.1 The Z-Y-X Euler Angles……... 61
5.7.2 Transformations…… 62
5.7.3 Rotational Equations of Motion……65

Chapter 6 Performance Evaluation 68

6.1 Introduction……...68

6.2 Performance Metrics……68

6.3 Additional Parameters of Interest…… 72

6.4 Indicators…….. 72

6.5 Arecibo Model Configuration……...73

6.6 Equilibrium Condition…….. 74

6.7 Dynamic Runs…….. 76

6.7.1 Effect of Wind Speed……77

6.7.2 Effect of Wind Direction……... 81

6.7.3 Effect of Turbulence…….. 83

6.8 Upgraded Arecibo Configuration...…….. 86

6.9 Selected Cases…….. 89

Chapter 7 Sensitivity Analysis 95

7.1 Test Matrix……96

7.2 Number of Mainstay Cables…… 97

7.3 Tower Radius……99

7.4 Effective Tower Stiffness……. 100

7.5 Platform Mass…….. 102

7.6 Cable-Platform Attachment Points……... 105

7.7 Mainstay Cable Properties: Plasma Rope……107

7.8 Summary……... 111

Chapter 8 Conclusion 112

8.1 Final Remarks……... 112

8.2 Future Recommendations……. 113

References 115

List of Figures

1.1 Single-Dish Radio Telescopes Located Around the World……..2

1.2 The Arecibo Radio Telescope…….. 4

1.3 Tower Base and the Welcome Center …….……4

1.4 The LAR and the Arecibo Radio Telescope……. 8

2.1 The Lumped Mass Approach in the LAR and the Arecibo…….…… 13

2.2 Node and Element Numbering Scheme…… 13

2.3 Flowchart of Simulation Overview……...18

3.1 Body-Fixed Coordinate System for a Cable Element……...20

3.2 Unstretched Length Configuration……23

3.3 Schematic Representation of the Internal Forces……..25

3.4 Nodal Force Body Diagram…….. 28

4.1 Tower and Backstay Cable Configurations…….. 30

4.2 Tower Cross Section…… 31

4.3 View of Tower-Top, Mainstay and Backstay Cables……... 33

4.4 Effective Tower Stiffness Model…….. 33

4.5 Geometry of the Perturbation Approach……...35

4.6 Tower Orientation in the Inertial Frame of Reference……..37

5.1 A Picture of the Arecibo Platform…… 41

5.2 The Platform Model's Body-Fixed Coordinate System……... 42

5.3 Cable-Platform Attachment Points……... 45

5.4 Flat Plate Normal to the Flow……...46

5.5 Drag Component Breakdown……48

5.6 Truss Pair Correction Factors……... 50

5.7 Finite to Infinite Aspect Ratio Correction Factors……51

5.8 Plan View Photograph of the Arecibo Platform……... 52

5.9 Correction Factors for Adjacent Truss Frames Used for the Top View of the Platform…….53
5.10 Angle of Attack…….55
5.11 Platform Cd*A versus Angle of Attack…… 57
5.12 Flow Around Sphere for Low Reynolds Number & High Reynolds Number..58
5.13 Using the Z-Y-X Euler Angle Set…….61
5.14 Angular Velocities in the Platform's Body-Fixed Frame…… 62
5.15 Dynamics Model Flowchart……..67

6.1 The Focal Plane and Hemisphere……...…….. 69
6.2 Tilt Angle Performance Metric……..….. 70
6.3 Performance Metrics to Equilibrium…….75
6.4 Tower-Top Positions to Equilibrium…… 76
6.5 Wind Direction and Tower Numbering…… 77
6.6 (a) Error in the Focal Plane vs Wind Speed……..…79
6.6 (b) Error Out of the Focal Plane vs Wind Speed…….. 79
6.6 (c) Platform Tilt Angle vs Wind Speed…… 80
6.7 (a) Error In the Focal Plane vs Wind Direction…… 81
6.7 (b) Error Out of the Focal Plane vs Wind Direction…….81
6.7 (c) Platform Tilt Angle vs Wind Direction……... 81
6.7 (d) Average Cable Tension vs Wind Direction…….82
6.7 (e) Average Tower Deflection vs Wind Direction……83
6.8 (a) Error in the Focal Plane vs Turbulent Mean Wind Speed……...84
6.8 (b) Error out of the Focal Plane vs Turbulent Mean Wind Speed…… 84
6.8 (c) Platform Tilt Angle vs Turbulent Mean Wind Speed……. 85
6.9 Average Error in the Focal Plane vs Wind Speed…….88
6.10 Average Platform Tilt Angle vs Wind Speed……... 88
6.11 Case A Performance Metrics…… 90
6.12 Case A Platform Rotation……91
6.13 Case A Platform Translation…….91
6.14 Case B Performance Metrics…….92

6.15 Case B Platform Rotation……. 93
6.16 Case B Platform Translation……93
6.17 Case B: Tower-Top Motion……..94

7.1 Equilibrium Platform Height vs No. of Mainstay Cables……97
7.2 Equilibrium Tensions per Cable vs Number of Cables……98
7.3 Error in the Focal Plane vs Tower Radius…… 99
7.4 (a) Error in the Focal Plane vs Number of Backstay Cables...……. 101
7.4 (b) Platform Tilt Angle vs Number of Backstay Cables……... 101
7.4 (c) Average Tower Deflection vs Number of Backstay Cables……102
7.5 Equilibrium Platform Height vs Platform Mass……103
7.6 Platform Tilt Angle vs Platform Mass…….. 104
7.7 Cable-Platform Attachment Points……... 105
7.8 Error in the Focal Plane vs Platform-Cable Attachment Radius…….. 106
7.9 Platform Tilt Angle vs Platform-Cable Attachment Radius……. 107
7.10 (a) Average Error in the Focal Plane vs. Wind Speed for Plasma Rope……...109
7.10 (b) Average Error out the Focal Plane vs. Wind Speed for Plasma Rope…… 110
7.10 (c) Tilt Angle vs. Wind Speed for Plasma Rope……...110

List of Tables

1.1 Summary of Construction Details…….6

3.1 Mainstay Cable Properties…… 19

4.1 Tower and Backstay Cable Configurations…….. 30
4.2 Tower Properties…….. 32

5.1 Physical Properties of Platform…….43
5.2 Summary of Drag Parameters……... 54

6.1 The Original Arecibo Configuration……73
6.2 Wind Speed Test Matrix……... 78
6.3 The Upgraded Arecibo Configuration…….. 86
6.4 Upgraded Platform Mass Moment of Inertias……...87

7.1 Test Matrix for the Sensitivity Analysis……... 96
7.2 Mainstay Cable Effective Areas……... 97
7.3 Average Tower Effective Stiffness……... 100
7.4 Platform Mass-Moment of Inertia…….103
7.5 Minimum Breaking Strength of Cables…… 104
7.6 Plasma Rope Properties…… 108
7.7 Qualitative Summary of Sensitivity Analysis…….. 111

Chapter 1 – Introduction

1.1 Radio Telescopes

Radio telescopes are used to detect and image electromagnetic radiation in the radio wave range. They generally consist of some components that collect the radiation and a receiver to detect the radiation [1]. Radio telescopes are used by radio astronomers to study our planet's atmosphere as well as asteroids and even distant galaxies [2]. A radio telescope has the difficult task of collecting and detecting very weak radio wave signals and hence, bigger is better when it comes to the collecting area of the telescope [1]. Some examples of the various shapes and sizes of radio telescopes from around the world are shown in Figure 1.1. In order to be of practical use in detecting the electromagnetic radiation from celestial bodies, a radio telescope's receiver must be very accurately held in position and orientation.

Located on the island of Puerto Rico, the Arecibo Radio Telescope (commonly called the "Arecibo Observatory" and often refereed to herein as simply "Arecibo") is the largest single-dish radio telescope in the world [3].

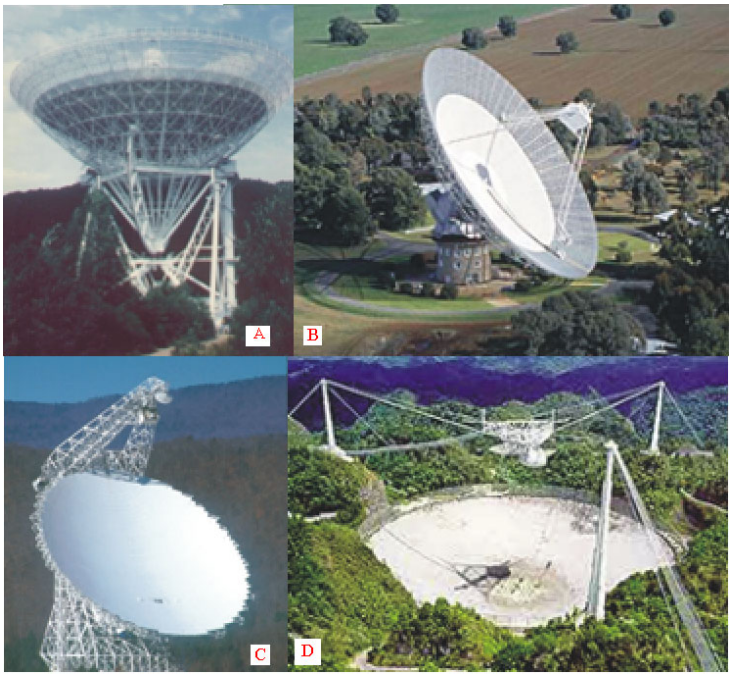

Figure 1.1 – Single-Dish Radio Telescopes Located Around the World.
A) 100 m Effelsberg in Germany B) 64 m Parkes in Australia
C)100 m Green Bank in U.S.A. D) 305 m Arecibo in Puerto Rico

1.2 Radio Telescope Simulations

When a new radio telescope is to be designed and constructed in this day in age, the structural and mechanical design process often calls on computer models and dynamic simulations; a cost-efficient and convenient tool. With the advance of computer models, it is of particular interest to model a design already in use, namely the Arecibo Radio Telescope. The Arecibo Radio Telescope was designed and constructed in the early 1960's [4] and with no use of dynamic simulation whatsoever. In developing a computer simulation, the system's behavior and performance may be observed over time, under various wind and turbulence conditions, without the expense and complications of experimental work. A sensitivity analysis may also be carried out in order to identify the parameters that may improve or deteriorate the system's performance, and all of this done on a personal computer workstation.

1.3 Arecibo Construction Overview

The Arecibo Radio Telescope was conceived by William E. Gordon who at the time was a professor at Cornell University [5]. The original Arecibo configuration became operational in November of 1963 [5]. Since that time the telescope has seen two major upgrades (one in 1974 and the other in 1997), which will be described in the next section. Figure 1.2 shows a photograph of the Arecibo Radio Telescope next to a close up of one the supporting towers. To observe the enormity of the structure notice, in Figure 1.3, the doorway entrance to the Welcome Center that is found at the base of one of the towers.

Arecibo's structural configuration consists of a 305 m diameter reflector dish; of spherical shape, with a radius of curvature of 265 m [2]. The spherical reflector always points straight up and unlike many other radio telescopes; it cannot be steered to a different direction. A natural bowl in the landscape of the region was found to aid in the construction effort of the enormous mesh surface dish.

The telescope's triangular feed support structure (referred to herein as the "platform") is suspended approximately 150 m above the surface of the reflector [5]. In the original configuration, the triangular platform had a mass of 550 tons, and was suspended by 12 main cables (each of 3 inch diameter - braided steel) from 3 towers. The 3 towers, whose tops are all of equal elevation, are positioned at a radial distance of 213 m from the center of the receiver. Due to the region's landscape, two of the three towers are of an equal length, 76.2 m, with the third having a length of 111.2 m. Supporting each tower, 5 backstay cables (each of 3.5 inch diameter - braided steel) run from the tower tops to concrete anchorages in the ground. Running from each corner of the platform are two 1.5 inch cables called tie downs (functioning as catenaries) which are anchored to the ground just along the rim of the reflector [5].

Figure 1.2 – The Arecibo Radio Telescope

Figure 1.3 – Tower Base and the Welcome Center

1.4 Arecibo Upgrades

The Arecibo Radio Telescope has undergone two major upgrades since it was first constructed. The first upgrade, completed in 1974, was carried out to improve the smoothness of the reflecting surface to an accuracy of 2.5 mm r.m.s [2]. Upgrades at that time also included "the addition of a powerful transmitter at 2380 MHz designed for radar studies of the solar system." [2].

The second Arecibo upgrade, completed in 1997, was the implementation of the new Gregorian system (receiver/transmitter), whose weight and additional structure increased the total mass of the platform form 550,000 kg to 815,000 kg. [2]. To support this much heavier platform, using the same three towers, additions to the number of cables were made: 6 auxiliary mainstay cables (each of $3\,{}^{1}\!/_{4}$ inch diameter) were added from the tower tops (2 per tower) to the platform and 6 auxiliary backstay cables (each of $3\,{}^{5}\!/_{8}$ inch diameter) were added from the tower tops to the ground. A new Gregorian system was installed on the triangular platform which brings rays from the spherical primary reflector to a point focus through a series of reflections [2]. The entire Gregorian enclosure is spherical in shape (as can be seen in Figure 1.2).

Finally, to meet the new pointing requirements of the telescope beam, three new pairs of vertically-oriented tiedown cables [2] were added at each corner of the triangular platform, anchored to the ground below the reflector. These new tiedown cables replaced the existing catenaries. Each tiedown is anchored to controllable jacks which can provide active control (using computer models) to the tiedown by exerting up to a "60 tons of vertical force" cables [2]. Table 1.1 summarizes and compares some of the important construction details of the Arecibo Radio Telescope. Throughout this work the "original" Arecibo will refer the state of the Arecibo upon initial construction and the "upgraded" Arecibo will refer the state of the Arecibo as it is found today (after both major upgrades).

	Construction of the Original Arecibo	**Construction of the Upgraded Arecibo**
platform mass	550 000 kg	815 000 kg
receiver drag	Line Feeds	Gregorian System
Mainstay Cables	4 cables per tower d = 3"	4 cables per tower d = 3"
Backstay Cables	5 cables per tower d = 3.25"	5 cables per tower d = 3.25"
Main Auxiliary Cables	N/A	2 cables per tower d = 3.25" Attached 2/3 of the way along the sides of the triangular truss
Backstay Auxiliary Cables	N/A	2 cables per tower d = 3.625"
Tie Down Cables	6 cables total d=1.5" Two off-vertical cables (functioning as catenaries) run from each corner of the platform and anchored to the ground near the rim of the reflector	6 cables total d = 1.5" Two cables run vertically from each corner of the platform and are anchored directly below the dish. Active Control Jacks which can exert up to 60 tons of vertical force.

Table 1.1 - Summary of Construction Details

1.5 LAR Model and Previous Work

The Arecibo dynamics model stems from an earlier version of a model created for the proposed "Large Adaptive Reflector (LAR)" [6]. The LAR dynamics model, developed by Dr. Meyer Nahon, includes the entire cable and wind models as well as the numerical integration scheme (all developed in C++). The following is a brief description of the LAR system and its various differences with the Arecibo Radio Telescope.

The particular version of the LAR model used in the conversion includes the following physical components: 3 plasma rope tethers, a payload (the telescope's receiver), a leash, and a lifting aerostat (balloon). The aerostat's buoyancy provides enough lifting force (approximately 40 kN) [6] to keep the telescope's receiver in its elevated position and hence the three tethers (which are anchored to the ground) in tension. Figure 1.4 shows the LAR system (shown with 6 tethers) and its various components along side the Arecibo Radio Telescope.

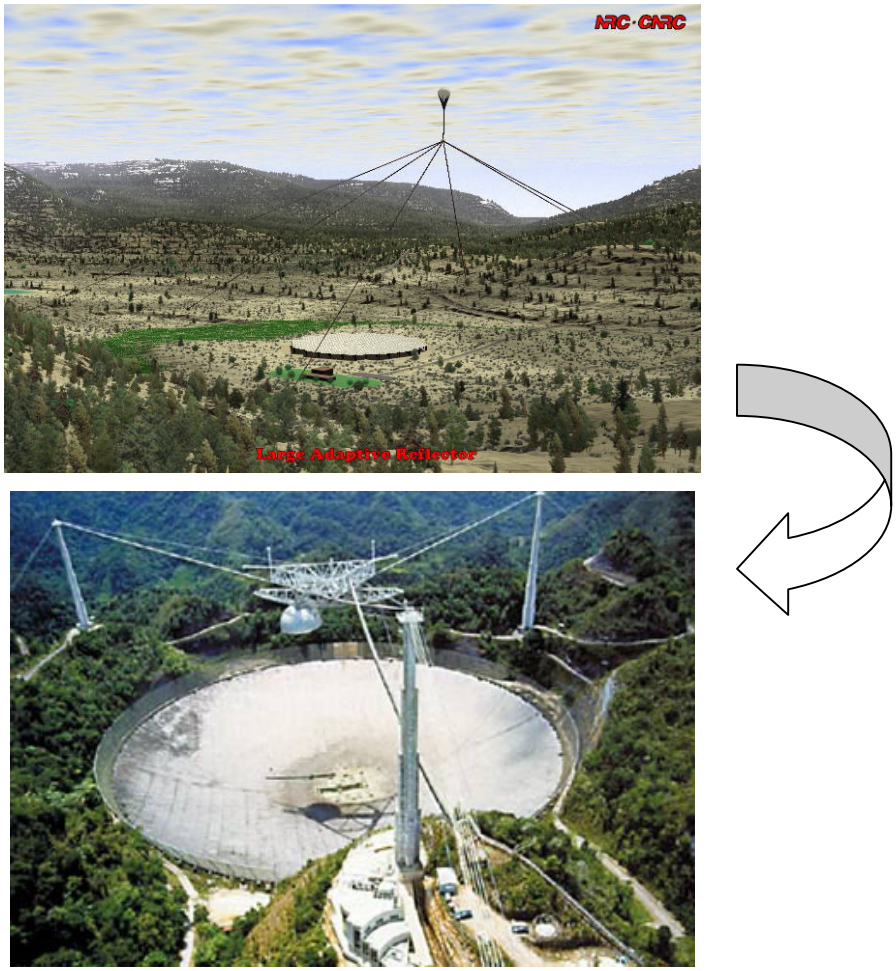

Figure 1.4 – The LAR (above) and the Arecibo Radio Telescope (below).

The basic differences between the two systems, among factors affecting the dynamics, are summarized as follows:

(i) The LAR tether base points are at *fixed* locations (anchored to the ground), whereas the high tower tops of the Arecibo cannot be assumed stationary, and in fact may sway as the tensions in the cables change.

(ii) The LAR design calls for lightweight materials in order to minimize the buoyancy requirements of the aerostat. On the other hand, the Arecibo platform was originally constructed having a mass of 550 tons.

(iii) The large platform - a triangular truss structure to which Arecibo's cables are attached - is to be considered a rigid body subject to the rotational equations

of motion. On the contrary, in the version of the LAR model used here, the LAR payload and aerostat are both considered subject to translational motion only.

(iv) In the version of the LAR model used here, the LAR payload and aerostat are both considered spherical for the purposes of their drag models. A new drag model for Arecibo's large triangular truss platform is required.

1.6 Scope of Thesis

In the context of this undergraduate honours thesis, a basic model for the dynamics of the tethered subsystem of the Arecibo Radio Telescope is first developed. The computer model of this subsystem is then subjected to a performance evaluation and a sensitivity analysis. In Chapters 2 to 5 the dynamics model is described in detail. We begin the model description with an overview and introduction to the modeling techniques and the simulation basics. In Chapter 3, the cable properties, kinematics and dynamics model are discussed. Chapter 4 deals with the tower model, construction details, properties, effective tower stiffness, and tower-top motion. Finally, in Chapter 5 the platform model is described which includes the platform drag model and the rotational equations of motion.

In Chapter 6, the various performance metrics of the Arecibo system are defined, and the motion and performance of the "original" Arecibo system are observed and evaluated under a variety of wind conditions (specifically wind speed, wind direction, and turbulence). Also in Chapter 6 is a general comparison between the "original" and "upgraded" configurations of the Arecibo Radio Telescope. In Chapter 7, a sensitivity analysis is carried out on the "original" Arecibo configuration. The sensitivity analysis involves changing the system's configuration one parameter at a time. Six different physical parameters are discussed, including: the number of mainstay cables, the tower radius, the effective tower stiffness, the platform mass, the cable-platform attachment points, and the mainstay cable properties. In closing, Chapter 8 contains the final remarks

and conclusions, as well as the recommendations for future work and development of the Arecibo model.

The modeled configurations of the Arecibo radio telescope are simplified in that they do not include the tiedown cables (neither the off-vertical catenaries in the original configuration nor the vertically oriented cables in the upgraded configuration). A large effort was indeed made to incorporate the tiedown cables into the model, and although we were close, it was decided that the tiedowns were beyond the scope of this thesis and consequently they have been left to future work.

Chapter 2 – The Arecibo Model

2.1 Overview

A dynamics model of the Arecibo Radio Telescope has been developed in Visual Studio C++. The model is described in several sections, which come together to form the 3-dimensional non-linear dynamics simulation. The Arecibo model will be presented in the following sections:

(i) Lumped Mass Approach
(ii) Simulation Basics
(iii) Cable Model (Chapter 3)
(iv) Tower Model (Chapter 4)
(v) Platform Model (Chapter 5)

To make the development of the Arecibo dynamics model tractable requires the use of certain assumptions and approximations. The kinematics and dynamics of Arecibo's physical components (which include the cables, the towers, and the platform) will be described in detail with attention drawn to the various assumptions and approximations. In terms of the overall dynamics of the system; the development of the translational equations of motion is governed by Newton's second Law, $\vec{F} = m\vec{a}$; while the development of the rotational equations of motion follow Euler's equations, $\vec{M} = \vec{I}\dot{\vec{\omega}} + \vec{\omega} \times \vec{I}\vec{\omega}$.

2.2 Lumped Mass Approach

The kinematics and dynamics of the Arecibo Radio Telescope are modeled using the same approach as that of the LAR system; the so-called "lumped-mass approach". This model has been validated for the LAR tethered aerostat system, as well as a number of underwater applications [6]. The basic principle is to divide the total unstretched length of the cables into a number of discrete cable elements, forming a set of nodes bounding each element. The mass of each cable element is then lumped into its end nodes, which are in turn treated as point masses. Further details of how we use the lumped mass approach in developing the governing equations of motion are discussed throughout this section. For now it suffices to become comfortable with the geometry and methodology used in the numbering of the nodes and cable elements. Figure 2.1 shows the geometry of the lumped mass approach as used in both the LAR and Arecibo models.

The numbering system for the nodes *and* the cable elements is very important to the organization within the code of the dynamics model. Figure 2.2 shows the numbering system for the Arecibo model as used in the performance evaluation, that is, with 5 nodes used for each of the 3 cables (Section 3.1 will rationalize the use of only 3 cables). Notice that the tower-top positions are in fact *not* considered to be nodes, in that they are not included in the node numbering system. The equations governing the motion of the tower-tops are determined separately from the other nodes and are discussed in detail in the tower model (Chapter 4). Also notice the very important shared confluence point, which is actually the center of mass of the Arecibo platform. In terms of the numbering system, the confluence point is considered to be the last node (#15). However, also sharing this location are the nodes #5 and 10. With the number of nodes per cable chosen as 5 here, the number of discrete cable elements is 5 per cable with numbering as shown in Figure 2.2.

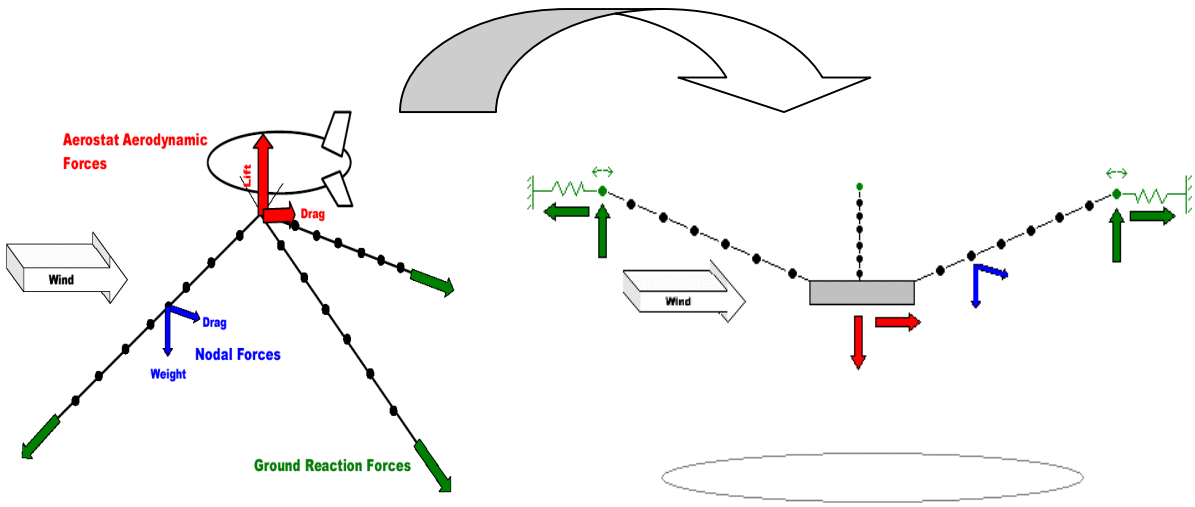

Figure 2.1 – The Lumped Mass Approach in the LAR (left) and the Arecibo (right)

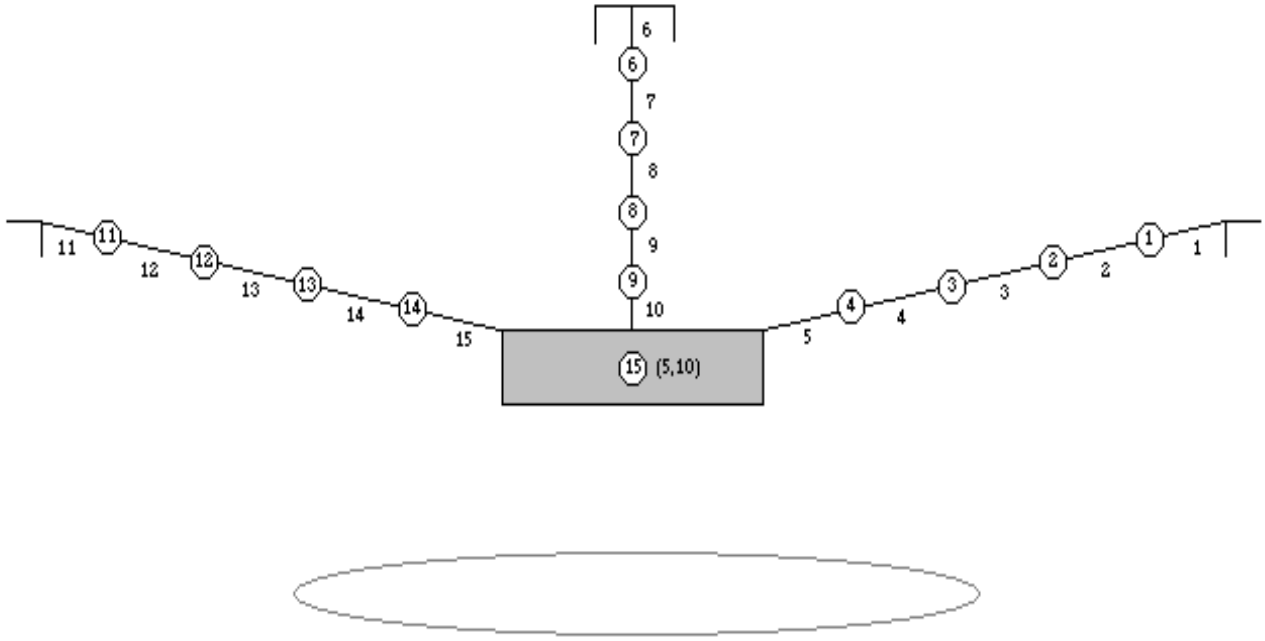

Figure 2.2 – Node and Element Numbering Scheme

2.3 Simulation Basics

Our goal is to develop a model capable of simulating the motion of the Arecibo system over a given period of time while under particular wind and turbulence conditions. The dynamics model of the Arecibo Radio Telescope has been reduced – through the lumped mass approach – to the dynamics of a finite number of point masses, subject to translational motion, and a rigid body platform, subject also to rotational motion. We begin by defining the state vector for the system and then present an overview of the numerical approach to solving the resulting non-linear, second order, differential equations of motion. The basics of the simulation are being presented early on, so that we may have a clear understanding of the overall modeling process involved.

2.3.1 The State Vector

The state of the Arecibo system may be completely defined at any time by the position and the velocity of its "n" nodes, in addition to the orientation and angular velocity if its platform. We define the first 6n elements of the state vector as follows [7]:

$$\mathbf{X}(t) = \begin{Bmatrix} \dot{x}_1(t) \\ x_1(t) \\ \dot{y}_1(t) \\ y_1(t) \\ \dot{z}_1(t) \\ z_1(t) \\ \vdots \end{Bmatrix} \tag{2.1}$$

Where $\mathbf{x}(t)$ gives the position of the nodes and $\dot{\mathbf{x}}(t) = \dfrac{d\mathbf{x}(t)}{dt}$ gives the velocity of the nodes. The very last 6 elements of the state vector define the platform's orientation and angular velocity in the inertial frame:

$$\mathbf{X}(t) = \begin{Bmatrix} \dot{\phi}(t) \\ \phi(t) \\ \dot{\theta}(t) \\ \theta(t) \\ \dot{\Psi}(t) \\ \Psi(t) \end{Bmatrix} \tag{2.2}$$

Where ϕ, θ, Ψ form the Z-Y-X Euler angle set which will be described in more detail in the platform model description (Chapter 5).

The length of the state vector depends on the number of individual nodes that must be described. We must be careful to subtract the nodes which are shared at the platform's centre of mass (recall Figure 2.2). We must also add the 6 rotational state variables required to describe the rotational motion of the platform. The total length of the state vector array is thus given by:

$$nodes = \#\, of\ nodes\ per\, cable = 5$$

$$cables = 3$$

$$\begin{aligned} length(\mathbf{X}) &= 6 \cdot [nodes \cdot cables - (cables - 2) + 1] \\ &= 6 \cdot [5 \cdot 3 - (3 - 2) + 1] \\ &= 84 \end{aligned} \tag{2.3}$$

2.3.2 Numerical Approach

The non-linear, second order differential equations of motion that result from the analysis in Chapter 3, are integrated numerically in order to observe the state of the Arecibo system over time. Any second order differential equation may be reduced to a system of first order differential equations by introducing a new variable [8]. The new variable in our case is the velocity. We then have a set of coupled first order differential equations that may be written in their most general form as follows [8]:

$$\mathbf{v}_i(t) = \frac{d\mathbf{x}_i(t)}{dt} \tag{2.4}$$

$$\frac{d\mathbf{v}_i(t)}{dt} = f_i(t, \mathbf{x}, \mathbf{v}) \tag{2.5}$$

In order to implement a numerical integration scheme, we must know the initial values of the state vector at some time t_o, and also the functions on the right hand side of Equation 2.5. The Arecibo model uses a fourth order Runge-Kutta integration scheme, which was already implemented in the LAR dynamics model by Nahon [6]. The Runge-Kutta scheme requires the following as input: the start and stop times (t_o and t_f), the initial state vector $\mathbf{X}$ and derivative of the state vector $\dot{\mathbf{X}}$ at time t_o, and the time step Δt. The integration scheme will then return the state vector values for each time step until t_f. In a step-wise manner, we can observe the state of the Arecibo system over time. Figure 2.3 shows a flow chart of the overall process by which the simulation runs.

The remaining sections describing the Arecibo model (Chapters 3 to 5) will focus primarily on how to determine the functions on the right hand side of the general Equation 2.5. In other words, we must evaluate the kinematics and dynamics of the system to develop the governing equations of motion that will determine the accelerations of the system (which will be used as input to the Runge-Kutta integration scheme).

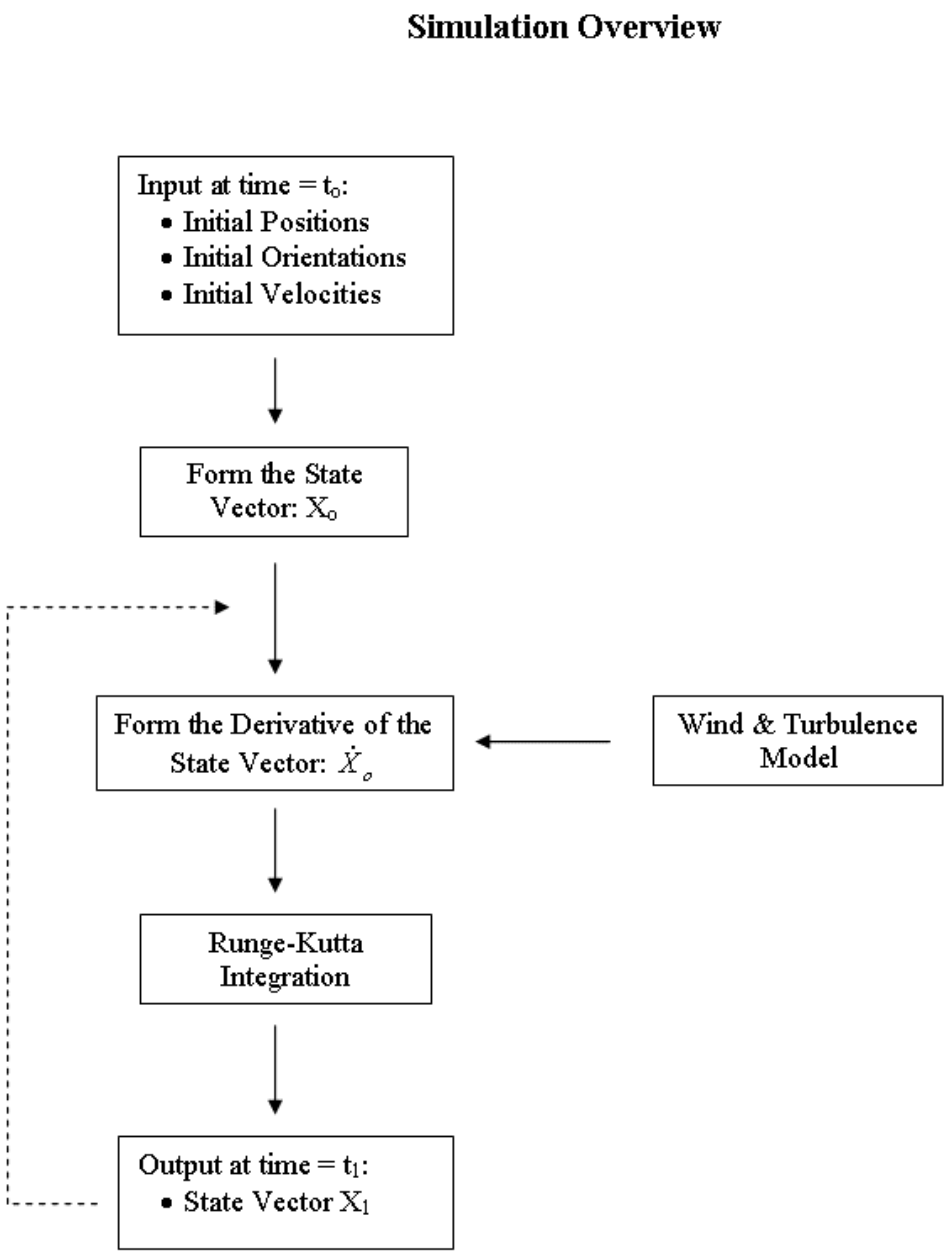

Figure 2.3 – Flowchart of Simulation Overview

Chapter 3 – Cable Model

As discussed in Section 2.2, the lumped mass approach is used to model the Arecibo cable dynamics. The cable properties, coordinate systems, kinematics and dynamics are all discussed in this section. Much of what follows may be found in more detail in Nahon's work on the LAR system [6]. The final results and equations from [6] are presented here in order to demonstrate the basics of the cable dynamics model and its use for the Arecibo Radio Telescope.

3.1 Cable Properties

The "original" Arecibo cable configuration consists of 12 braided steel cables, each of 3-inch diameters. Each tower-top (considered the cable base points) has 4 of these closely spaced cables running toward the near corners of the triangular platform. These 4 mainstay cables are modeled together as one cable having an equivalent effective area given by:

$$A_{eff} = \frac{n_c \pi (d_c)^2}{4} \tag{3.1}$$

Where A_{eff} is the effective area of the cable, n_c is number of actual mainstay cables per tower and d_c is the diameter of each actual mainstay cable. Hence the system is immediately simplified to one in which only 3 main cables are supported by the 3 towers. Other cable properties include the modulus of elasticity for braided steel cables. This is taken to be half of the modulus of elasticity for steel, as is commonly used for braided cable construction [9]. The cable properties used in the Arecibo model are given in the Table 3.1.

Mainstay Cable Properties			
Parameter	**Symbol**	**Value**	**Units**
Individual cable Diameters	d_c	0.0762	m
Density	ρ	7850	kg/m^3
Elastic Modulus	E	1.00E+02	GPa

Table 3.1 - Mainstay Cable Properties

3.2 Coordinate Systems

There are two different frames of reference used when describing the position of the cable nodes and the orientation of the cable elements. The first is the inertial frame of reference, in which the orthogonal coordinate axes are considered to be fixed with respect to the Earth. The origin is located at the bottom-centre of the collector dish (i.e. at an elevation equal to the lowermost point of the collector dish). The Z_i-axis points vertically toward the sky, while the X_i-axis points toward one of the three towers and the Y_i-axis completes the coordinate system by the right-hand-rule. The second frame of reference will be called the "body-fixed" frame which is fixed relative to each cable element. The q-axis is tangential and in the direction of the cable element itself, while the p1 and p2-axes complete the orthogonal coordinate system by forming a plane whose normal is a vector in the direction of the q-axis. The body-fixed coordinate system is shown for a given cable element in Figure 3.1.

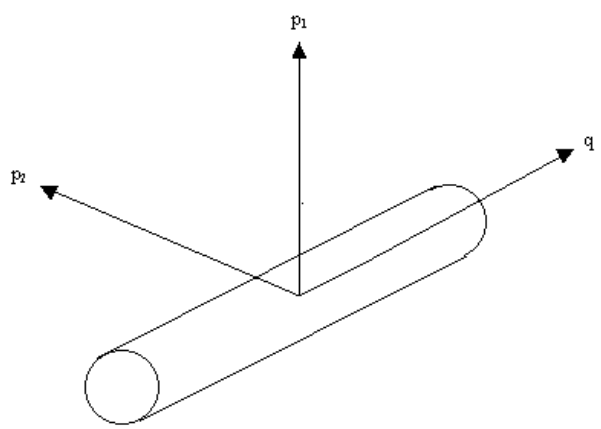

Figure 3.1 – Body-Fixed Coordinate System for a Cable Element

3.3 Cable Kinematics

The positions of the nodes are described using the inertial frame and the corresponding (x,y,z) coordinates. The orientations of the elements are described using an Euler angle set. Specifically, the Z-Y-X Euler angle set is used with the angles denoted by (Ψ, θ, ϕ). For a more thorough explanation of the Z-Y-X Euler angle set, and how it is to be used, the reader is referred to the platform model description in Section 5.7.1. The rotation matrix that brings any vector from the body-fixed frame to the inertial frame is given by [6].

$$R^i = \begin{bmatrix} \cos\theta^i & \sin\theta^i \sin\phi^i & \sin\theta^i \cos\phi^i \\ 0 & \cos\phi^i & -\sin\phi^i \\ -\sin\theta^i & \cos\theta^i \sin\phi^i & \cos\theta^i \cos\phi^i \end{bmatrix} \tag{3.2}$$

The following equations [6] are used to calculate the Euler angles. The superscript i and i-1 refer to the two nodes bounding the ith element:

$$\theta^i = a\tan 2(x^i - x^{i-1}, z^i - z^{i-1}) \tag{3.3}$$

$$\Phi^i = a\tan 2\left[-(y^i - y^{i-1}), \frac{(z^i - z^{i-1})}{\cos\theta^i}\right] \text{ if } \cos\theta \geq \sin\theta^i \tag{3.4}$$

$$\Phi^i = a\tan 2\left[-(y^i - y^{i-1}), \frac{(x^i - x^{i-1})}{\sin\theta^i}\right] \text{ if } \cos\theta < \sin\theta^i \tag{3.5}$$

The angle Ψ (a rotation about the Z-axis) is taken as zero since the torsion in the elements is neglected (as discussed in the next section).

3.4 Cable Dynamics

The forces acting on the cable elements must be applied to the point masses located at the cable nodes. It is important to distinguish that although the forces are applied throughout the continuous cable, they are treated as acting only at the nodes. The various forces acting *on* the cable elements (but acting *at* the nodes) are:

(i) Cable Tension
(ii) Cable Damping
(iii) Aerodynamic Drag
(iv) Gravity

The above forces are divided into the internal (tension and damping) and external (aerodynamic drag and gravity) forces acting on the cables. The effect of the bending stiffness in the cables is much smaller in magnitude than the tensile stresses and axial stiffness [9] and is therefore neglected. An important result of this, to the cable kinematics, is that the angle of rotation about the inertial Z-axis, Ψ, is always equal to zero [6].

3.4.1 Internal Forces

The internal forces are those forces that are generated within the braided cables. The first force to consider is the tension. Each individual cable element is treated as an elastic element [6] subject only to axial deformation. To calculate the unstretched lengths of the elements, we consider the platform's centre of mass to be at equal elevation as the tower tops, and take the distance from the 'cable-platform' attachment points to the 'cable-tower' attachment points, as shown in Figure 3.2

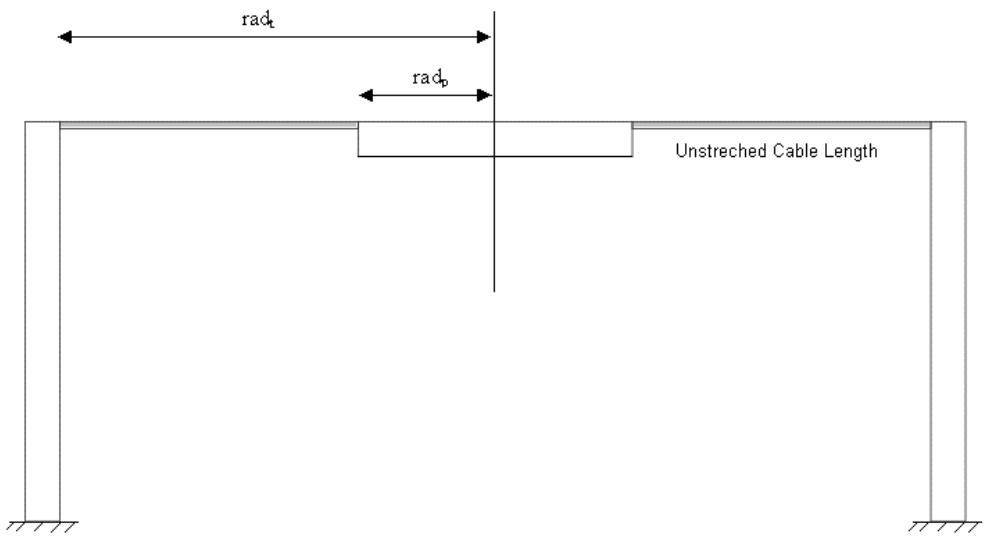

Figure 3.2 – Unstretched Length Configuration

The unstretched length of the entire cable is found to be:

$$\begin{aligned} l_u &= rad_t - rad_p \\ &= 213.36\ m - 38.01\ m \\ &= 175.35\ m \end{aligned} \tag{3.6}$$

With 5 elements per cable the unstretched length of each element is taken to be:

$$l_u^{\ i} = \frac{l_u}{No.\ of\ \ elements} = 35.07\ m \tag{3.7}$$

At equilibrium the elevation of the platform's centre of mass is approximately 35 m below the tower tops. The actual lengths of the cable elements, at a given instant, must now be determined in order to calculate the strain. The length of the ith cable element is given by:

$$l^i = \sqrt{(x^i - x^{i-1})^2 + (y^i - y^{i-1})^2 + (z^i - z^{i-1})^2} \tag{3.8}$$

Where x, y, z are the components of the position vector $\vec{r}$ which spans from the inertial origin to the given node. The exceptions to the above length calculation are the

first or uppermost cable elements (#1, 6, 11) and the last or lowermost cable elements (#5, 10, 15). The length calculations for the last elements are based on the second-last nodes (#4, 9, 14) and the cable-platform attachment points (see platform model Section 5.4 for details). The cable-platform attachment points are not explicitly considered nodes; however the inertial coordinates of these "fictitious nodes" are used to determine the lengths and Euler angles of the lowermost elements. The length calculations for the uppermost elements are based on the tower-top locations and the first node locations.

Once the lengths have been calculated, the axial tension forces in the cable elements may be found as [6]:

$$T_q^{\,i} = A_{eff} E \varepsilon^i \qquad where \;\; \varepsilon^i = \frac{l^i - l_u^{\,i}}{l_u^{\,i}} \tag{3.9}$$

The exception to using Equation 3.9 directly is only in the first cable elements of each cable; the tower-top positions and the tension in elements (#1, 6, 11) depend implicitly on each other. The equations for the tower-top motion and the first element tensions are explained and solved simultaneously in the Tower Model section.

The second internal force to be considered is the damping generated in the cables. "The energy dissipation in the cables is due primarily to the friction generated in their braided construction" [6]. The viscous damping is considered proportional to the tangential velocity of one bounding node relative to the element's other bounding node. The damping force is calculated as [6]:

$$P_q^{\,i} = C_v^{\,i}(v_q^{\,i} - v_q^{\,i-1}) \tag{3.10}$$

Where $P_q^{\,i}$ is the damping force in the ith element, C_v is the damping coefficient, and $v_q^{\,i}$ is the tangential velocity of the ith node. The damping coefficient, as compared to the mass and the stiffness of a system, is generally a more difficult parameter to measure directly [10]. Taken from Nahon's work, the damping coefficients used in the Arecibo cable elements are not considered constant, but rather depend on the tension force in each cable element:

$$C_v^{\,i} = 2\xi\sqrt{\frac{T_q^{\,i} A_{eff} E\varepsilon^i}{g}} \quad where \;\; \xi = 0.015 \tag{3.11}$$

Where T denotes the tension, g is the gravitational constant (taken as $9.81 m/s^2$), and ξ is the damping ratio taken as 0.015 [11]. Figure 3.3 shows a schematic of the spring-damper system in which the spring represents the cable stiffness and the dashpot is used to indicate the presence of the damping force [10].

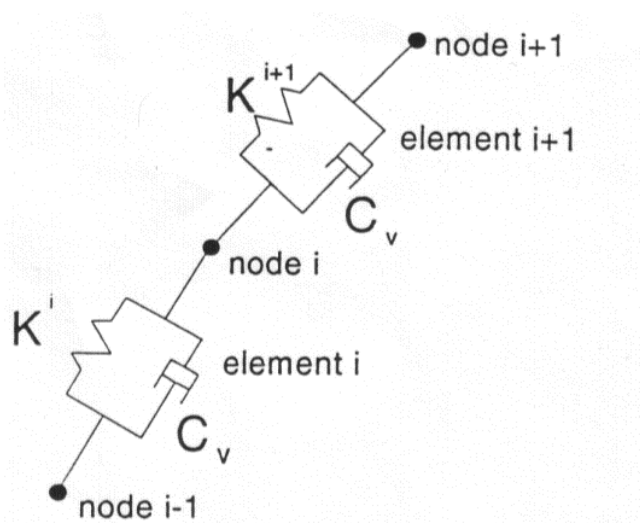

Figure 3.3 – Schematic Representation of the Internal Forces [6].

Finally, a condition is imposed in the dynamics model that will always set the tension and damping forces equal to zero if or when the tension is calculated as negative. That is, if the cable element is physically slack then there will be no tension or damping forces in that cable element. In reality the cable elements should never be slack, however in the simulation, as the system comes to a static equilibrium from its unstretched length configuration, slack cable elements may be found.

3.4.2 External Forces

The external forces acting on the cable system are the aerodynamic drag and the Earth's gravity [6]. First considering the gravitational forces, we calculate the weight acting in the negative inertial Z direction. The lumped mass approach requires the calculation of the mass of each cable element:

$$m_c^{\ i} = \rho_{steel} V_c^{\ i} \text{ where: } V_c^{\ i} = A_{eff} l_u^{\ i} \tag{3.12}$$

Where $V_c^{\ i}$ is the volume of the cable element calculated based on the unstretched length of the element, $l_u^{\ i}$. The gravitational force acting on the ith cable element is calculated using the gravitational constant as:

$$W^i = m_c^{\ i} \cdot g \tag{3.13}$$

Where W^i and $m_c^{\ i}$ refers to the weight and mass of the ith element respectively. However, it is important to note (as will be discussed later) that the gravitational force acts at the nodal points bounding each cable element.

The aerodynamic drag acting on the cables is found as a function of the relative velocities of the cable element midpoints to that of the surrounding air. The coefficient of drag for the cylindrical cable is taken as, $C_{dc} = 1.2$ [6]. The drag force acting on the ith cable element is calculated as follows [6]:

$$D^i = \sqrt{D_{p1}^{i\ 2} + D_{p2}^{i\ 2} + D_q^{i\ 2}} \tag{3.14}$$

Where the components are calculated as:

$$D_{p1}^i = -\left(\frac{1}{2}\rho_{air} C_d d_c l_u^{\ i}\right) f_p \left|v^i\right|^2 \frac{v_{p1}^i}{\sqrt{(v_{p1}^i)^2 + (v_{p2}^i)^2}} \tag{3.15}$$

$$D_{p2}^{i} = -\left(\frac{1}{2}\rho_{air} C_d d_c l_u^{\ i}\right) f_p \left|v^i\right|^2 \frac{v_{p2}^{i}}{\sqrt{(v_{p1}^{i})^2 + (v_{p2}^{i})^2}} \tag{3.16}$$

$$D_{q}^{i} = -\left(\frac{1}{2}\rho_{air} C_d d_c l_u^{\ i}\right) f_q \left|v^i\right|^2 \tag{3.17}$$

Where v^i (and its components $v_{p1}^{i}, v_{p2}^{i}, v_{q}^{i}$) refers to the velocity of the cable element's midpoint relative to the surrounding air. The f_p and f_q are the required loading functions that "account for the nonlinear breakup of drag between the normal and tangential directions"[6]. For a more rigorous description of the loading functions and the relative velocity calculations the reader is referred to [6].

3.4.3 Translational Equations of Motion

We are now ready to set-up the translational equations of motion for the nodal point masses, which follow Newton's second law; $\mathbf{F} = m\mathbf{a}$. The approach is to apply the external and internal forces at the nodes. In order to apply the drag and weight to the nodes, we must take only half of the drag and weight of the cable elements to the right, and similarly from the cable element to the left of the given node. For example, the mass of the ith node is equal to half of the mass of the element to its right plus half of the mass of the element to its left. The approach is more easily understood by observing the force body diagram of a given node as shown in Figure 3.4.

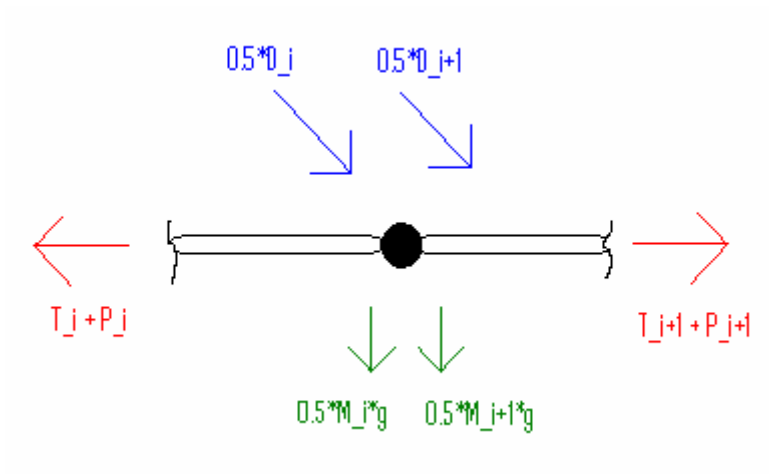

Figure 3.4 – Nodal Force Body Diagram

The equations governing the motion of the cable nodes follow Newton's second law, such that:

$$M^i \ddot{\mathbf{r}}^i = (\mathbf{T}^{i+1} + \mathbf{P}^{i+1}) - (\mathbf{T}^i + \mathbf{P}^i) + \frac{1}{2}(\mathbf{D}^{i+1} + m_c^{\ i+1}\mathbf{g}) + \frac{1}{2}(\mathbf{D}^i + m_c^{\ i}\mathbf{g}) \qquad (3.18)$$

Where $\mathbf{M}^i$ is the mass of the ith node and $\ddot{\mathbf{r}}^i$ is the acceleration vector of the ith node. The following points should be noted regarding the governing equations of motion:

(i) The tension, damping, and aerodynamic drag forces must be transformed into the inertial frame of reference.

(ii) The governing equation is a vector equation which represents 3 equations in the inertial frame of reference

(iii) The governing equation is a non-linear second order differential equation that must be solved using numerical techniques (as discussed in Section 2.3.2)

Chapter 4 – Tower Model

The Arecibo Radio Telescope, being the largest single-dish radio telescope in the world, employs the distinct tower support structure. In this section, the construction details of the towers are discussed and their properties determined. In modeling the towers we first calculate their effective stiffness while keeping in mind that our final goal is to solve the equations of motion for the tower-tops (cable base points) to be implemented in the dynamics model.

4.1 Construction Details

The three tall towers are each made of reinforced concrete with a cross-shaped cross-sectional area. To keep the platform level, their tower-tops were designed to all be at the same elevation. Due to the uneven landscape, two of the towers are 250 ft in height and the third is 365 ft in height [12]. The construction of the towers themselves was a tedious task, rising at a slow rate of less than 10 inches per hour [13]. It took about 16 days of cement pouring to construct one of the two shorter towers [13]. To facilitate their construction, a concrete production plant was installed at the Arecibo construction site.

The original Arecibo construction includes 5 backstay cables running from the tower-tops to the ground where they are anchored to cement blocks. The main purpose of the backstay cables is to support the towers (in bending) while carrying the heavy load of the platform. The 5 backstay cables are each of diameter 3.25 inches. The anchorage locations (both in radius and elevation) are unique to each tower; again due to the uneven landscape. Figure 4.1 shows the general construction of the three towers with their backstay cables. "The towers are labeled as T4, T8, and T12 following the numbers on the face of a watch, T12 being the one due north." [13]. Table 4.1 gives the dimensions and angles of each tower-backstay configuration.

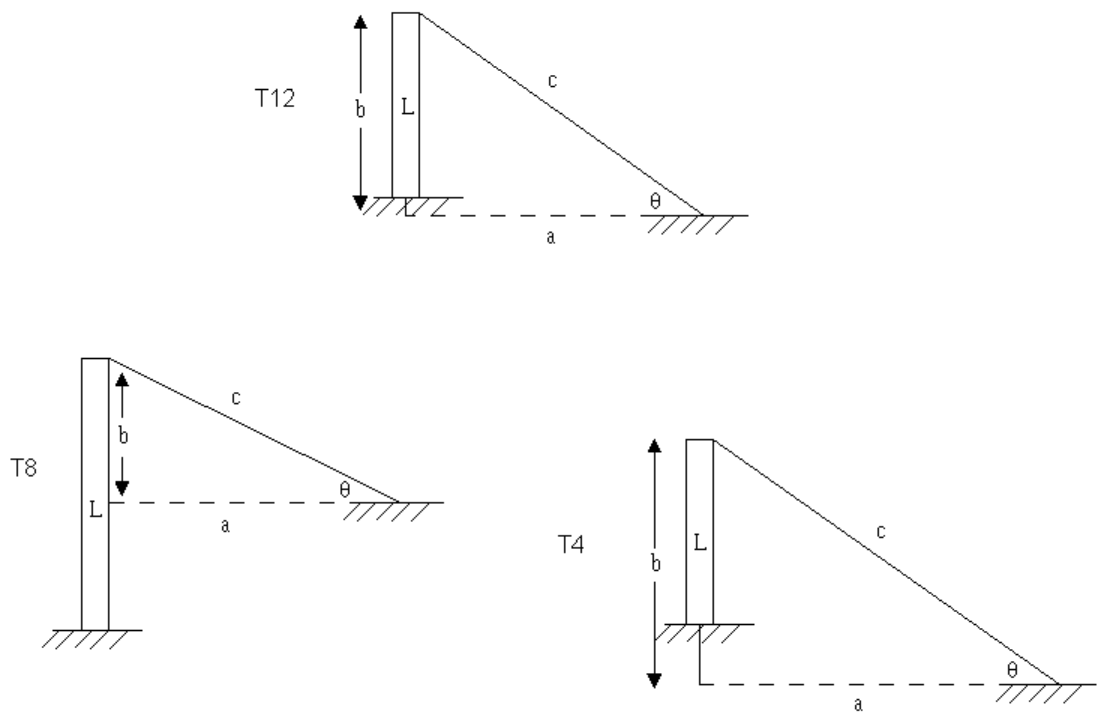

Figure 4.1 – Tower and Backstay Cable Configurations

Tower	Property	Symbol	Value	Units
T8	Tower Height	L	111.252	[m]
	Anchorage Radius	a	118.872	[m]
	Backstay Cable Length	b	58.3692	[m]
	Tower-Anchorage Elevation	c	132.4293	[m]
	Backstay Cable Angle	θ	26.1522	[deg]
T4	Tower Height	L	76.2	[m]
	Anchorage Radius	a	138.684	[m]
	Backstay Cable Length	b	99.5172	[m]
	Tower-Anchorage Elevation	c	170.6954	[m]
	Backstay Cable Angle	θ	35.6626	[deg]
T12	Tower Height	L	76.2	[m]
	Anchorage Radius	a	115.824	[m]
	Backstay Cable Length	b	83.058	[m]
	Tower-Anchorage Elevation	c	142.5266	[m]
	Backstay Cable Angle	θ	35.6445	[deg]

Table 4.1 – Tower and Backstay Cable Configurations

4.2 Tower Properties

The tower cross-sectional dimensions are not constant throughout their lengths. In fact, the cross sectional area decreases from base to top both continuously and in clearly visible increments at particular heights. The dimensions and geometry of the cross-section is required to determine the moment of inertia of the towers to be used in determining their stiffness in bending. As an approximation, the tower cross-section is assumed to be constant based on dimensions that are available from the AutoCAD drawings of the Towers [14]. Figure 4.2 shows the geometry of the tower cross section. Table 4.2 gives the constant tower properties as used in the Arecibo model

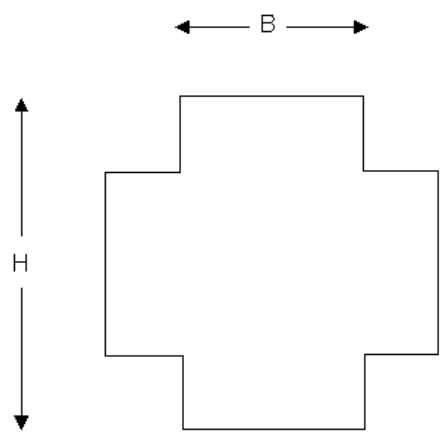

Figure 4.2 – Tower Cross Section

For the given cross-sectional geometry (which is symmetric) the area moment of inertia is given by: [15]

$$I = \frac{BH^3 + (H - B)B^3}{12} \tag{4.1}$$

Property	Symbol	Value	Units
Cross Sectional Dimension	H	2.74	[m]
Cross Sectional Dimension	B	1.83	[m]
Area Moment of Inertia	I	2.64	[m^4]
Concrete Elastic Modulus	E	25	[GPa]
Tower Height (2)	L	76.20	[m]
Tower Height (1)	L	111.25	[m]

Table 4.2 – Tower Properties

4.3 Effective Stiffness

Important to the cable and tower models is the fact that the 4 mainstay cables are completely different than the 5 backstay cables. "The reason for the different number of cables and diameter is related to the different angles at which the cables carry the loads" [13]. Figure 4.3 shows a photograph of one of the three tower-tops as seen from ground level. Notice the 5 backstay cables running to the right, the 4 mainstay cables to the left, as well as the main and backstay auxiliary cables installed during the second Arecibo upgrade. Since the mainstay cables are terminated at the tower-tops we may model the combined effect of both the tower itself and the backstay cables as one. For the purpose of modeling the system, the tower and backstay cables are replaced by a single-degree-of-freedom spring with an effective stiffness, k_{eff}, and no damping, as shown in Figure 4.4. In order to calculate the effective stiffness, we first separate the physical problem into two parts: the contribution of the tower's stiffness in bending and the contribution of the backstay cables.

Figure 4.3 – View of Tower-Top, Mainstay and Backstay Cables.

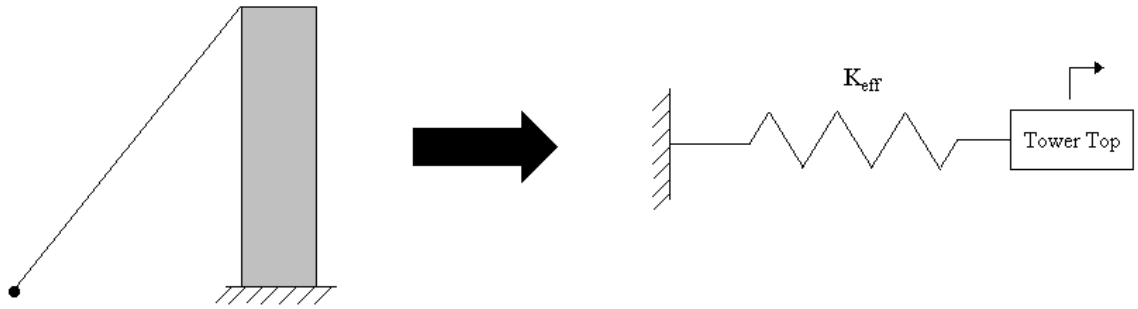

Figure 4.4 – Effective Tower Stiffness Model

4.3.1 Tower Contribution

To calculate the contribution of the tower's stiffness in bending, we treat the tower as a simple beam subject to the transverse load of the mainstay cable tension. The deflection of the cantilever beam is given by the following equation [16]:

$$\Delta x_{top} = \frac{TL^3}{3EI} \tag{4.2}$$

Where L is the length or total height of the towers, E is the modulus of elasticity of the concrete material, and I is the area moment of inertia of the towers. In treating the tower-tops as 1-dimensional springs, whose motion is constrained to the horizontal plane, the contribution of the stiffness may be calculated using Hook's Law:

$$T = k_{tower} \Delta x_{top} \tag{4.3}$$

$$k_{tower} = \frac{T}{\Delta x_{top}} = \frac{3EI}{L^3} \tag{4.4}$$

4.3.2 Backstay Cable Contribution

In order to determine the contribution of the backstay cables to the overall effective stiffness, we use a perturbation approach. The problem is that of solving the angles and lengths of the backstay cables geometrically before and after a horizontal perturbation of the tower-top. The perturbation acts to stretch the backstay cables from their initial length, thus creating a reaction force (a tension) from which the effective stiffness may be calculated. Figure 4.5 is a schematic of the geometry. The initial length, L_1, and angle to the horizontal, θ_1, of the backstay cables are found using the design details of the AutoCAD drawings [14]. The cosine law is used to calculate the length of the backstay cables after the tower-top is displaced horizontally by a distance $\Delta x_{top.}$. The actual magnitude of the perturbation has no effect on the final backstay cable contribution (so long as the perturbation is small, i.e. less than 1 m)

$$L_2 = \sqrt{L_1^{\ 2} + \Delta x_{top}^2 - 2L_1 \cos\alpha} \qquad where \;\; \alpha = 180 - \theta_1 \tag{4.5}$$

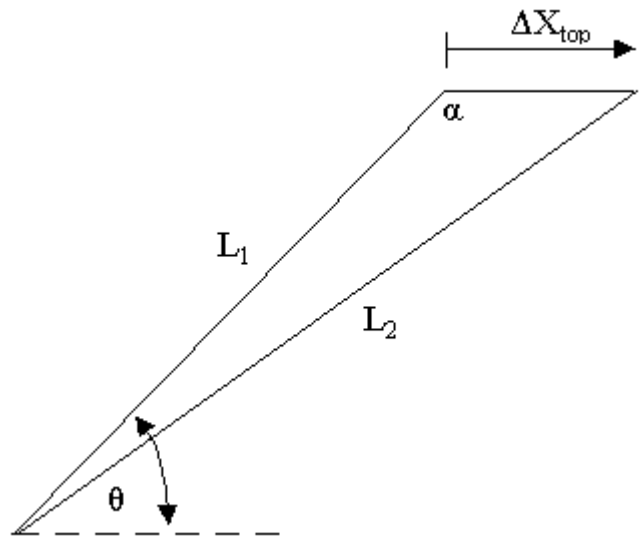

Figure 4.5 – Geometry of the Perturbation Approach

The 5 backstay cables are treated as one cable whose area is calculated by:

$$A_{eff} = \frac{n_{bc}\pi(d_{bc})^2}{4} \tag{4.6}$$

The change in tension as a result of the tower-top moving a distance $\Delta x_{top.}$ may then be found using:

$$\Delta T = A_{eff} E\varepsilon \qquad where \;\; \varepsilon = \frac{L_2 - L_1}{L_1} \tag{4.7}$$

In the horizontal direction:

$$\Delta T_x = \Delta T \cos\theta_1 \tag{4.8}$$

Finally the contribution of the backstay cables to the overall effective stiffness may be found using:

$$k_{bc} = \frac{\Delta T_x}{\Delta x} \tag{4.9}$$

4.3.3 Combined Effective Stiffness

We may now calculate the combined effective stiffness of the towers and the backstay cables. The springs are taken as acting in parallel such that the total effective stiffness is the sum of the two parts:

$$k_{eff} = k_{bc} + k_{tower} \tag{4.10}$$

As an example, the values found for tower T4 are $k_{bc} = 1.03 \times 10^7 N/m$, $k_{tower} = 4.57 \times 10^5 N/m$ and $k_{eff} = 1.08 \times 10^7 N/m$. It should be noted that the contribution of the backstay cables is 2 orders of magnitude greater than the tower itself. As shown in Figure 4.1 and Table 4.1 the geometry of each tower and its backstay cables are each unique. This implies that the amount of tower deflection for each tower, under the static loads would each be different. In reality the tensions in the backstay cables are pre-tensioned such that, upon initial erection, the platform's position and orientation is centered and level above the dish. In the Arecibo model, for all three tower-top locations, an average of the three cases is used as the overall effective stiffness. The final combined and averaged effective stiffness is presented in table 7.1 of the sensitivity analysis (Section 7.4).

4.3.4 Tower-Top Motion

As mentioned in Section 3.4.1, the tension in the first (uppermost) elements of each cable and the length of the first cable elements depend implicitly on each other. That is, we need to know the length, relative to the unstretched length, in order to calculate the tension force, however the tension force must be used to determine the tower-top location and hence the length, as per Equation 3.8. Simply put, at a given instant, they both must be calculated simultaneously. A system of equations is set-up and

solved analytically, in closed form, to arrive at a new expression for the tension in the first elements and to govern the tower-top motion. The following equations describe the tension and the tower-top locations.

$$T = EA_{eff}\frac{(l - l_u)}{l_u} \tag{4.11}$$

$$\text{where} \quad l = \sqrt{(x_t - x_n)^2 + (y_t - y_n)^2 + (z_t - z_n)^2} \tag{4.12}$$

$$x_t = rad_t \cos\theta - \frac{T\cos\theta}{k_{eff}} \tag{4.13}$$

$$y_t = rad_t \sin\theta - \frac{T\sin\theta}{k_{eff}} \tag{4.14}$$

In the above system of equations, the unknown quantities are the tension, T, and the positions of the tower-tops in the horizontal plane of motion, x_t and y_t (in the inertial frame of reference). All other quantities are considered known. An increase in the mainstay cable tension acts to move the tower-tops closer to the centre of the collector dish, or in other words, it acts to decrease the tower-top radial distance in the horizontal plane. The angle θ is calculated in the plan view of the Arecibo, based on the tower orientation, as shown in Figure 4.6.

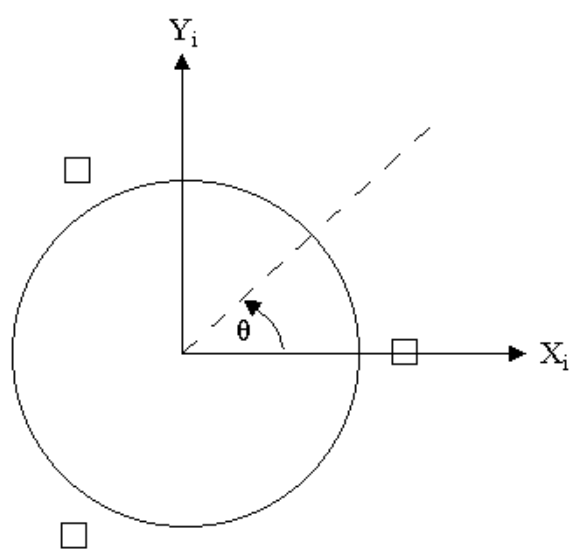

Figure 4.6 – Tower Orientation in the Inertial Frame of Reference

After some lengthy algebra, we arrive at a quadratic equation of T in terms of the known quantities. The final solution is of the form:

$$AT^2 + BT + C = 0 \xrightarrow{quadratic\ formula} T = \frac{-B - \sqrt{B^2 - 2AC}}{2A} \tag{4.15}$$

Where:

$$A = \frac{1}{k_{eff}^{\ 2}} \tag{4.16}$$

$$B = -\frac{2rad_t}{k_{eff}} + \frac{2x_n}{k_{eff}}\cos\theta + \frac{2y_n}{k_{eff}}\sin\theta \tag{4.17}$$

$$C = rad_t^{\ 2} - 2x_n rad_t \cos\theta - 2y_n rad_t \sin\theta + x_n^{\ 2} + y_n^{\ 2} + (z_1 - z_2)^2 \tag{4.18}$$

It turns out that the negative square-root of the quadratic equation yields tensions that make sense physically with the actual Arecibo system, whereas the positive square-root yields unreasonable magnitudes. We may now back-substitute, using Equations 4.13 and 4.14, to calculate the tower-top inertial coordinates in the horizontal plane.

As an approximation, the angle that the mainstay cables make with the horizontal plane of motion of the tower-tops is not taken into account. In reality, the angles at equilibrium are in fact small (i.e. less than 10 degrees), the cosine of the angle is always greater than 0.98, and we make the assumption it is approximately 1.0. This simplification in the model, allows for a closed form solution, but introduces a small error in the final equilibrium position of the tower-tops. In fact, the difference in the equilibrium position of the tower-tops (when making this simplification) is approximately 1.8 cm of a total 94 cm deflection from the tower-tops initial start position being that of zero cable tension. Note that when the Arecibo was initially constructed, the cables were all pre-tensioned and the towers did not deflect more than 2 inches throughout the process [13]. The percent error in the equilibrium position may be calculated as:

$$\%Error = \frac{1.8cm}{94cm} \times 100\% = 1.9\% \tag{4.19}$$

To eliminate this simplification, the angle that the first cable elements make with the horizontal plane of the tower-top motion would also have to be solved simultaneously with the tensions and tower-top positions, making the problem (specifically the mathematics) even more difficult. Currently, the angles of *all* the elements must be calculated using the *known* positions of each end of the elements (as is done for the LAR system). With the effect of the towers and backstay cables combined as an effective stiffness and the tower-top equations of motion derived, we move onto the final physical component of the Arecibo Telescope; the platform.

Chapter 5 – Platform Model

The receiver of the Arecibo Radio Telescope is held aloft by a very large triangular truss section, which will be referred to herein as the "platform". The motion of the receiver, which is important to the astronomer (see performance metrics Section 6.2), will in fact be modeled by evaluating the dynamics of the platform's centre of mass. To begin, the construction details and the platform properties will be discussed. Next a model for the aerodynamic drag experienced by the platform will be presented. Finally, the platform will be treated as a rigid body, and the rotational equations of motion governing its orientation in space will be discussed.

5.1 Construction Details

The platform is a very heavy structure which upon initial erection had a total suspended mass of approximately 550 000 kg (or 550 tons). After the second upgrade the platform's mass was increased to 815 tons [2]. The platform is constructed as a truss structure on which the receiver may be positioned with millimeter precision [2]. The receiver may move along an azimuth arm which may rotate about a circular track in order to take on various zenith and azimuth angles. Since Arecibo's collector dish is spherical, the incident radiation does not reflect to a single focal point, but rather reflects onto a line [5]. For the Arecibo Radio Telescope, the receivers/transmitters are either in the form of a line feed or a set of enclosed secondary and tertiary reflectors, known as the Gregorian (as was implemented in the second Arecibo Upgrade completed in 1997) [2]. Important to the model is the fact that Arecibo's platform does not itself take on different azimuth and zenith angles; meaning that there is no need to consider these angles in the cable model (unlike the LAR in which the cable lengths are changed using winches to allow the receiver to take on different azimuth and zenith positions). Figure 5.1 shows a picture of

the rather complex truss structure. The azimuth arm and circular track can be seen, along with the two types of receivers/transmitters (the line feed on the left and the spherical Gregorian on the right).

Figure 5.1 – A Picture of the Arecibo Platform

5.2 Coordinate Systems

In order to model the platform, we first define the coordinate systems used to describe its position and orientation in space. Similar to the cable model we use the inertial frame of reference with axes X_i-Y_i-Z_i (as defined in Section 3.2). We also use the "body-fixed" frame oriented such that the Z_b-axis points upward (toward the sky) in a

direction normal to the plane of the triangular shape truss. The X_b-axis points towards one of the corners of the isosceles triangle and the Y_b-axis completes the orthogonal coordinate system using the right-hand-rule. The origin of the body-fixed coordinate system is located at the platform's centre of mass. The centre of mass will be defined in the next section. Figure 5.2 shows the body-fixed coordinate system.

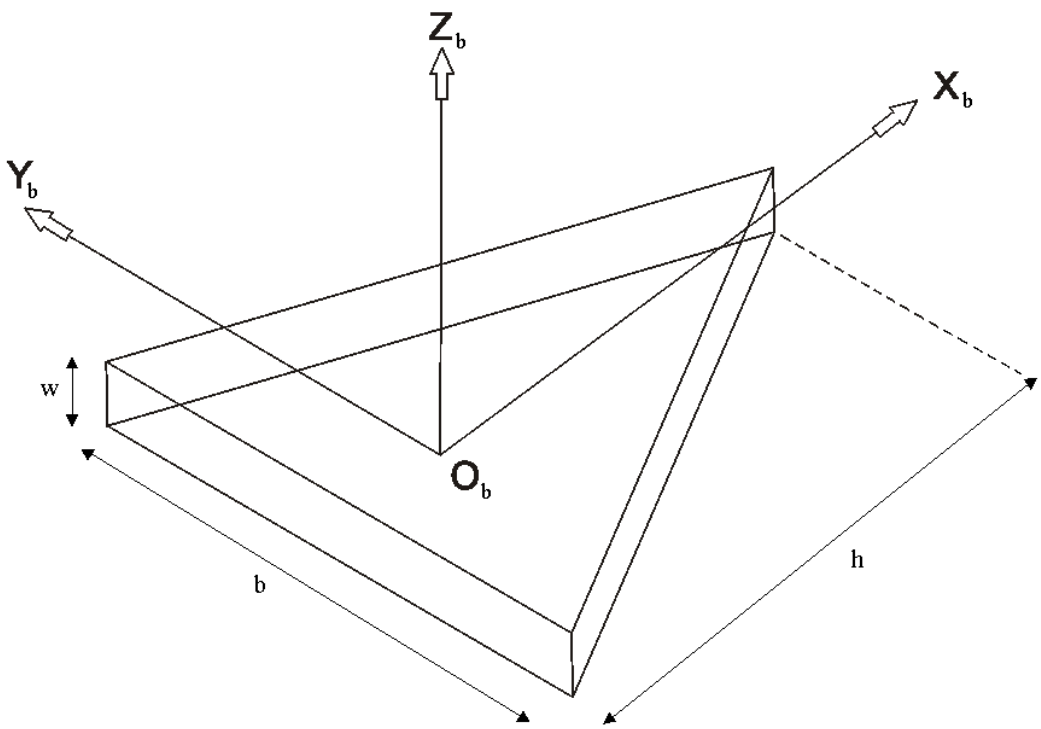

Figure 5.2 – The Platform Model's Body-Fixed Coordinate System

5.3 Platform Properties

The following simplifications are imposed on the complex truss structure in order to model the platform and evaluate its properties.

(i) The platform's structure (which includes the azimuth arm is reduced to a slice of an isosceles triangular shaped section. The section is of equal dimensions to the outer triangular truss frame of the actual Arecibo platform (may be seen in Figure 5.1).

(ii) The centre of mass is considered to be at the geometric centre of the triangular section. Important to the dynamics model is the fact that the lower-most node (i.e. the confluence point #15) is located at this centre of mass of the modeled platform.

(iii) The platform is of uniform density such that its mass (defined as the total suspended mass – including the receivers) is evenly distributed over its volume.

Table 5.1 gives the platform's physical dimensions and properties as used in the Arecibo Model:

Property	Symbol	Value	Units
Mass	m_p	550 000	[kg]
Base	b	65.84	[m]
Height	h	57.02	[m]
Vertical width	w	9.14	[m[
Gross Volume	V	34 313	[m^3]
Uniform Density	ρ	16.03	[kg/m^3]

Table 5.1 – Physical Properties of Platform

In the Section 5.7 we will treat the platform as a rigid body subject to both translational and rotational motion. The rotational equations of motion require that we know the platform's mass moment of inertia. The mass moment of inertia of any 3-dimensional body is a measure of the body's resistance to angular accelerations [17] and is given by [7].

$$I_{xx} = \int_M (y^2 + z^2)dm \qquad I_{xy} = I_{yx} = \int_M xydm$$

$$I_{yy} = \int_M (z^2 + x^2)dm \qquad I_{xz} = I_{zx} = \int_M xzdm \tag{5.1}$$

$$I_{zz} = \int_M (x^2 + y^2)dm \qquad I_{yz} = I_{zy} = \int_M yzdm$$

The mass moment of inertia of the platform is conveniently expressed in a 3x3 matrix, known as the inertia matrix (or tensor), for use in the rotational equations of motion [18]:

$$\mathbf{I} = \begin{bmatrix} I_{xx} & -I_{xy} & -I_{xz} \\ -I_{yx} & I_{yy} & -I_{yz} \\ -I_{zx} & -I_{zy} & I_{zz} \end{bmatrix} \tag{5.2}$$

Rather than trying to evaluate the above integrals analytically, and with no success in finding expressions for the mass moment of inertia of a common triangular shaped section such as the platform, our attention was turned to available CAD software. The platform was created as a 3-dimensional part in ProE® software, into which the uniform density of the platform could be entered as a material property. The resulting inertia matrix, for the properties in Table 5.1, is found to be:

$$\mathbf{I} = \begin{bmatrix} 1.032\times10^{8} & 0 & 0 \\ 0 & 1.032\times10^{8} & 0 \\ 0 & 0 & 1.987\times10^{8} \end{bmatrix} \tag{5.3}$$

The cross terms in the above inertia matrix are all zero, implying that there are two planes of symmetry in the modeled platform. This is indeed the case with one plane of symmetry being the x-z plane and the second being the x-y plane. It should also be noted that when the sensitivity analysis is performed (Chapter 7), and the platform mass is changed, the mass moment of inertia must be recalculated for each case.

5.4 Cable Attachment Points

The mainstay cable attachment points are considered to be in line with the platform's centre of mass, as previously defined. That is, they are considered to be located at $Z_b = 0$ in the body-fixed coordinate system and at a radius of $rad_p = 38.01\ m$ in the direction of the three towers. As per the Arecibo AutoCAD drawings, the mainstay cable attachment points are in fact in line with the platform's arm, the receiver, and in fact all other extruding truss sections into the simpler triangular section. Figure 5.3 shows the cable attachment points in the actual platform vs. the model.

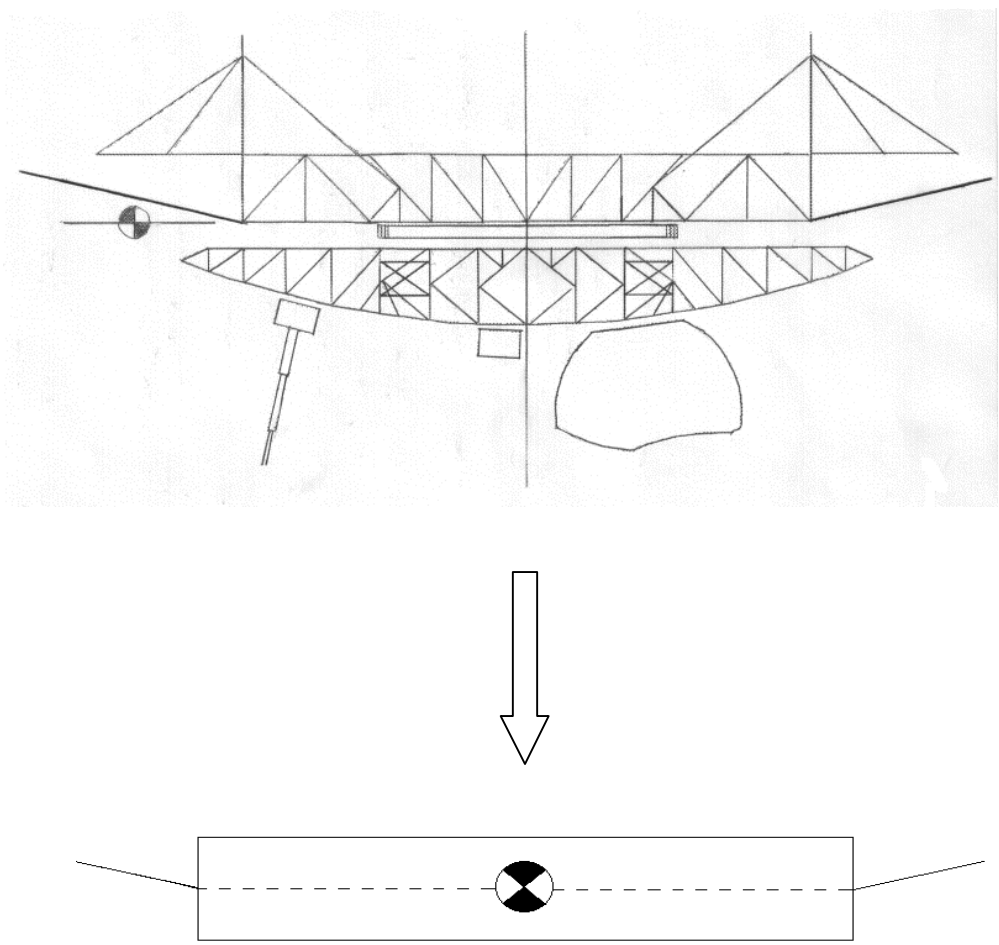

Figure 5.3 – Cable-Platform Attachment Points

5.5 Platform Drag

The model for evaluating the aerodynamic drag forces acting on the triangular truss platform is here described. In general, despite the wide applications of truss frameworks subjected to wind forces, calculating the drag coefficients of such structures is in some cases "inconsistent and in disagreement with experimental results" [19]. In other words, without experimental results, obtaining accurate drag coefficients of a specific or a particular truss structure can be a very difficult task. That being said, we must still attempt to at least approximate the drag forces acting on the platform and to do this we make various simplifying assumptions to the structure itself.

Arecibo's platform although a huge structure is composed of largely spaced truss members. The platform is treated as being very poor at generating a lift force. So much so, that the induced drag (the component of drag due to lift generation) and the lift force itself may be neglected. Hence, the drag acting on the platform is assumed to be caused entirely by form type drag. In general, form drag results from the pressure distribution normal to the body's surface [20]. The case of pure form drag acting on a flat plate normal to the flow is shown in Figure 5.4. In the case of bluff bodies with sharp edges, such as this, the drag coefficients tends to be approximately constant over a large range of Reynolds numbers [20].

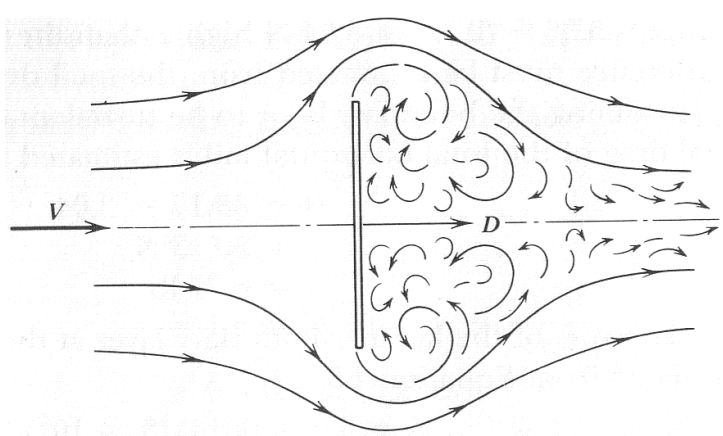

Figure 5.4 – Flat Plate Normal to the Flow [20].

5.5.1 Factors Affecting Drag

The main factors to be considered when determining the drag force acting on a trussed framework in general, at a given wind speed, are listed in Simiu and Scanlan [19].

i) The aspect ratio, λ: the ratio of the length of the overall framework to its width. Which is used to consider either the two-dimensional $(\lambda = \infty)$ or three-dimensional $(\lambda = finite)$ nature of the truss section

ii) The solidity ratio of the trussed framework, ϕ: the ratio of the effective area to the gross area (bounded by the outer truss members). The effective area is here defined as the area that the shadow of the truss members would project onto a plane which is behind the framework and perpendicular to the airflow.

$$A_{eff} = \phi \cdot A_{gross} \tag{5.4}$$

iii) The angle of attack, α, of the platform with respect to the oncoming wind

iv) Truss frame shielding: the shielding of portions of the framework by other portions of the framework located upwind. We will consider the effects of having two adjacent truss frames normal to the wind.

The first step in approximating the drag coefficients of the platform is to separate the horizontal and vertical sides of the platform and consider them separately with respect to the oncoming wind direction. The spherical Gregorian receiver (introduced after the second upgrade) is also considered separately (in a later section) and added to the overall drag force only when considering the "upgraded" Arecibo configuration. Figure 5.5 shows the decomposition of the various components of the platform. For the truss frames we use Equation 5.4 to calculate the effective area of the given truss face. Considering the wind direction normal to the given truss face, we consider its drag coefficient equal to that of a 3-dimensional flat plate (also oriented normal to the wind). The area of the 3-dimensional flat plate is considered equal to the effective area of the given truss face. When we take the angle of attack of the two truss faces into consideration (Section 5.5.4),

we will see how the drag forces of the two platform faces are combined to find the overall platform drag.

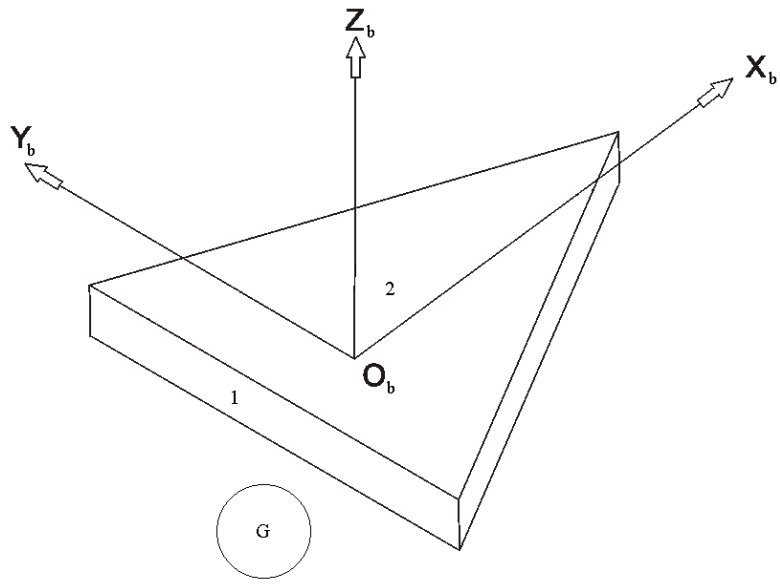

Figure 5.5 – Drag Component Breakdown

The coefficient of drag for a 3-dimensional flat plat, with an aspect ratio of 1, normal to the wind is taken from [20] as:

$$C_D^{(1)} = 1.18 \tag{5.5}$$

Where the superscript (1) indicates that this is the drag coefficient for a single truss frame normal to the wind (i.e. no truss frame shielding is taken into account).

5.5.2 Side View of Truss

To obtain the drag coefficient of the vertical face, #1 of Figure 5.5, we consider the wind force to act normal to the vertical truss face of the platform. The solidity ratio was approximated using the available AutoCAD drawings [14] and various photographs of the truss structure. Figure 5.3 shows an AutoCAD drawing of the platform's vertical face with the azimuth arm perpendicular to the wind direction (which is always assumed).

For the vertical truss face, #1, the solidity ratio is taken as $\phi = 0.3$. The effective area is then calculated as:

$$\begin{aligned} A_{1eff} &= \phi \cdot A_{1gross} = \phi \cdot (b \cdot w) \\ &= 0.3 \cdot (65.84 \cdot 9.14) \\ &= 180.53\ m^2 \end{aligned} \tag{5.6}$$

Where, the dimensions of the platform (b, h, and w) are defined by Figure 5.2 and Table 5.1. The aspect ratio of the vertical truss face is given by:

$$\begin{aligned} \lambda_1 &= \frac{b}{w} \\ &= \frac{65.84}{9.14} \\ &= 7.2 \end{aligned} \tag{5.7}$$

As a first approximation to the effects of truss frame shielding (factor iv as listed above) we model the vertical face as consisting of two parallel truss frameworks adjacent to one another and separated by a distance "e". The separation of the two vertical truss frames is taken as h/2 of the platform; $e = \frac{h}{2} = \frac{57.02}{2} = 28.51m$. Both truss frames are considered normal to the wind. The ratio of the spacing to the width of the truss frames, will prove to be useful, and is denoted by e/d [19]. The width of the truss frames is taken as the dimension w of the platform, $d = w = 9.14m$. Taking the width as 'w' rather than 'b' (as per Figure 5.2), we more closely represent an infinite aspect ratio truss; a correction factor for the infinite aspect ratio assumption will later be considered. For the vertical face the ratio e/d is thus given by:

$$\frac{e}{d} = \frac{28.51}{9.14} = 3.12 \tag{5.8}$$

In Simiu and Scanlan [19] this problem was looked at by considering that the overall drag coefficient of the two vertical trusses (denoted $C_D{}^{(2)}$) may be obtained from the drag coefficient of a sing truss frame, when multiplied by some correction factor, k:

$$C_D{}^{(2)} = k \cdot C_D{}^{(1)} \tag{5.9}$$

The approximate correction factors are presented in Figure 5.6, which plots the correction factor $k = \frac{C_D{}^{(2)}}{C_D{}^{(1)}}$ versus the solidity ratios ϕ for various ratios of $\frac{e}{d} > 1$. For the vertical face of the platform, we find that the correction factor is given approximately by: $k = 1.7$. Therefore, we find the drag coefficient of the side view of the platform when normal to the wind is approximated by:

$$\begin{aligned} C_{D1}{}^{(2)} &= k \cdot C_D{}^{(1)} \\ &= 1.7 \times 1.18 \\ &= 2.0 \end{aligned}$$

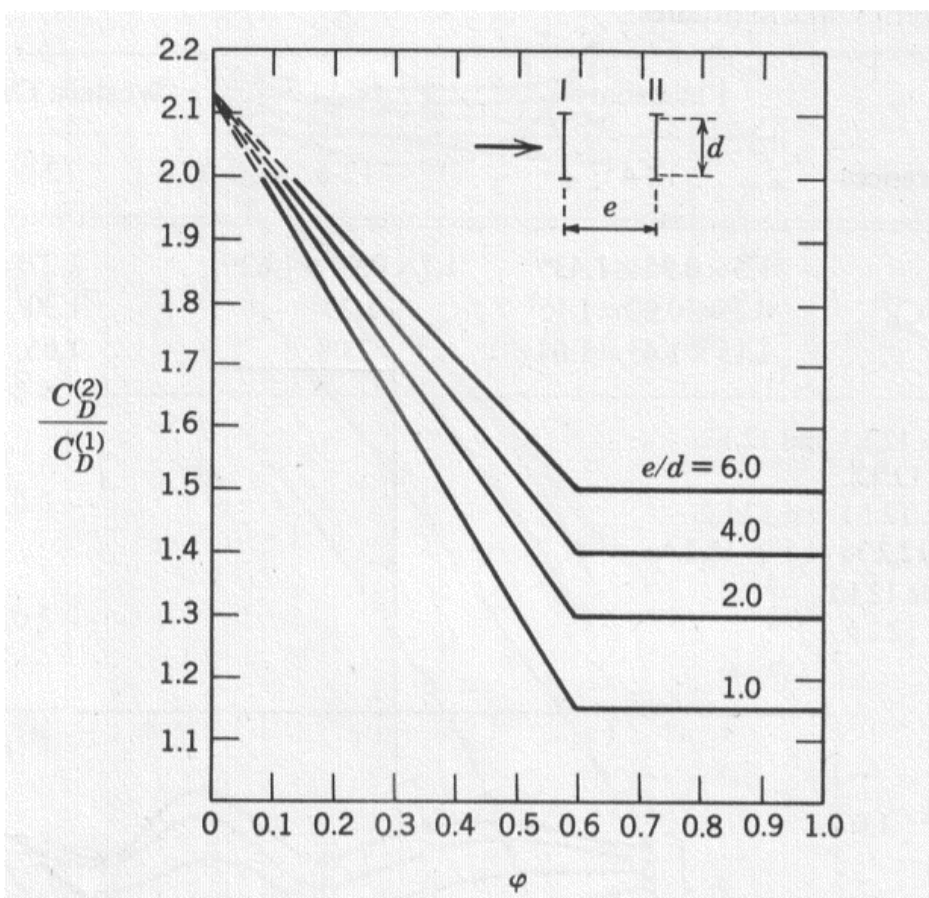

Figure 5.6 – Truss Pair Correction Factors [19].

The values of $C_D^{(2)}$ obtained by Figure 5.6 are given for infinite aspect ratio truss frames. It has been found in [19] that for small solidity ratios, the ratio of $\frac{C_D(\lambda)}{C_D(\lambda=\infty)}$ is very nearly constant (and close to one) for a wide range of aspect ratios. Figure 5.7 is used to find a second correction factor that will give us the final combined drag coefficient for the side view of the platform:

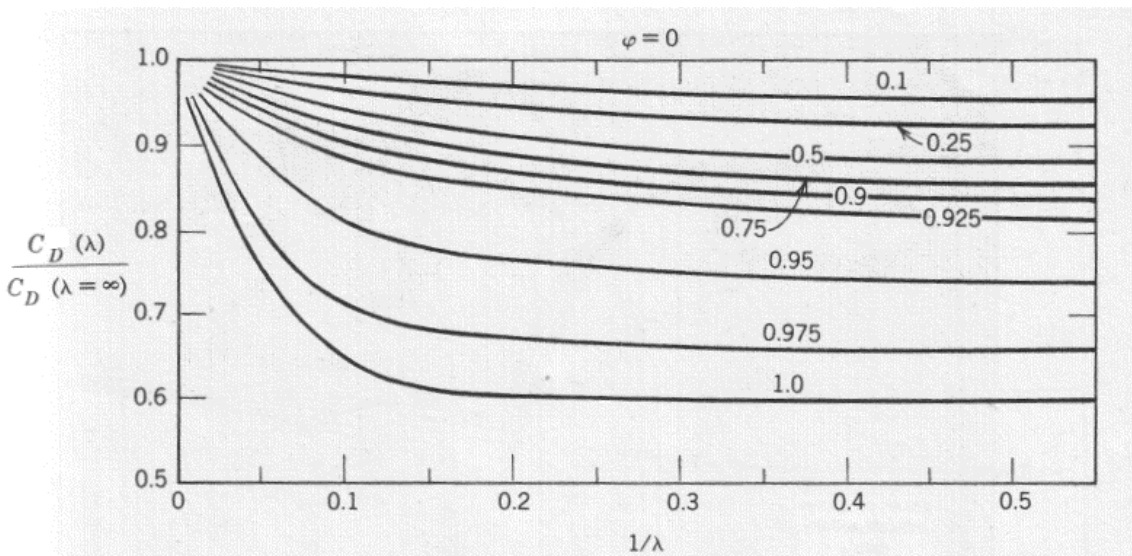

Figure 5.7 – Finite to Infinite Aspect Ratio Correction Factors [19].

Therefore the final drag coefficient for the vertical face of the platform is given by:

$$\begin{aligned} C_D^{(2)} &= 0.96 * 2.0 \\ &= 1.9 \end{aligned} \tag{5.10}$$

5.5.3 Top View of Truss

The top side of the platform is considered to be far less "solid" than the vertical side. It has a much larger gross area and smaller aspect ratio than the vertical surface of the platform. To approximate the drag coefficient of the top face of the truss, we assume that it is placed normal to the wind (it should be noted that this condition is never realized by the Arecibo platform). For the top truss face, the solidity ratio is taken as $\phi = 0.1$. A photograph of the plan view of the platform is shown in Figure 5.8.

Figure 5.8 – Plan View Photograph of the Arecibo Platform

The effective area of the top face is calculated as:

$$\begin{aligned} A_{2_{eff}} &= \phi \cdot A_{2_{gross}} = \phi \cdot (\frac{bh}{2}) \\ &= 0.1 \cdot (\frac{65.84 \cdot 57.02}{2}) \\ &= 187.71\, m^2 \end{aligned} \tag{5.11}$$

We model the vertical face as consisting of two parallel truss frameworks adjacent to one another and separated by a distance $e = w = 9.14\, m$, equal to the vertical width of the platform, w. The length and width of the truss frame are approximatly equal, as if it where a square. Hence the aspect ratio is taken as 1, with $d = \frac{2}{3} b = 43.89\, m$. The ratio of the spacing between truss fames to the width of the truss frames is given by:

$$\frac{e}{d} = \frac{9.14}{43.89} = 0.2$$

For ratios of $\frac{e}{d} < 1$ we find the coefficient of drag of the pair of trusses using the same principle as the vertical side of truss, that is:

$$C_D{}^{(2)} = k \cdot C_D{}^{(1)}$$

Where k is given here by the sum of two correction factors plotted in Figure 5.9

$$k = (\Psi_I + \Psi_{II}) \tag{5.12}$$

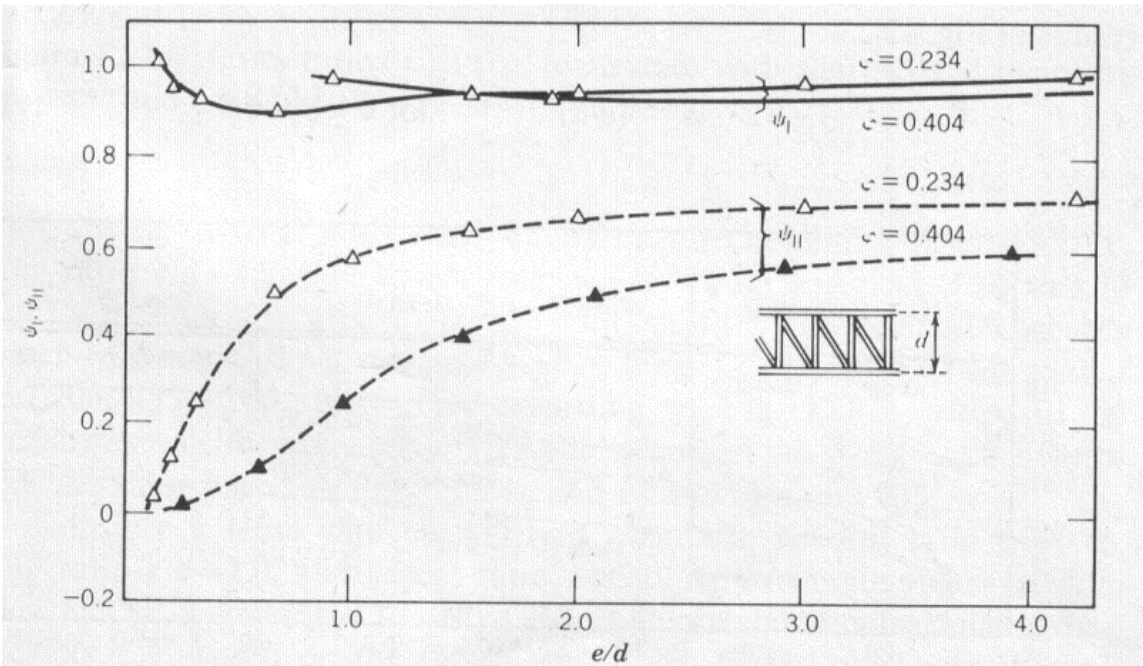

Figure 5.9 – Correction Factors for Adjacent Truss Frames Used for the Top View of the Platform [19].

As can be seen for the vertical face having a solidity ratio less than 0.2 and $e/d = 0.2$, the correction factors are taken as:

$$\begin{aligned} \Psi_1 &\approx 1 \\ \Psi_{II} &\approx 0 \end{aligned} \tag{5.13}$$

$$k = 1 + 0 = 1 \tag{5.14}$$

Therefore the combined drag coefficient of the top truss face pair is given by:

$$C_D{}^{(2)} \approx C_D{}^{(1)} \approx 1.18 \tag{5.15}$$

Correcting for the infinite aspect ratio, for which the correction factors are based, and using Figure 5.7, we obtain:

$$\begin{aligned} C_{D2}{}^{(2)} &= 0.97 \times 1.18 \\ &= 1.14 \end{aligned} \tag{5.16}$$

In summary, Table 5.2 gives the final drag properties of both the side and top faces of the platform:

Property	Side View	Top View
Coefficient of Drag, $C_D^{(2)}$	1.9	1.14
Effective Area, A_{eff} [m^2]	180.53	187.71
Solidity Ratio, φ	0.3	0.1
Aspect Ratio, λ	7.2	1
e/d	3.12	0.2

Table 5.2 – Summary of Drag Parameters

5.5.4 Platform Angle of Attack

The wind and turbulence model used in the Arecibo model was previously developed and used by Nahon in his model of the LAR system [6]. It considers the mean wind to move only in the horizontal plane, such that the Z_i - component of the mean wind velocity is always zero. The magnitude of the wind velocity may be calculated as:

$$|\mathbf{V}_w| = \sqrt{V_{Wx}{}^2 + V_{Wy}{}^2} \tag{5.17}$$

So far we have found approximate values for the platform truss section given two particular cases: the wind is normal to either the top of the platform or the sides of the platform. In order to calculate the angle of attack at any instant in time, we need to know the orientation of the platform and the components of the wind velocity vector. The components of the wind velocity vector are known from the wind model (developed for the LAR system). The unit vector in the direction of the wind velocity (which does not consider the Z-component of the wind that would be introduced by the turbulence model) is given by:

$$\hat{\mathbf{V}}_w = \frac{V_{wx}}{|\mathbf{V}_w|}\hat{\mathbf{i}} + \frac{V_{wy}}{|\mathbf{V}_w|}\hat{\mathbf{j}} + 0\hat{\mathbf{k}} \tag{5.18}$$

With regards to the orientation of the platform, we need to know the components of the unit vector in the same direction as the platform's body-fixed Z_b – axis. Here we introduce the rotation matrix that brings a vector's components in the body-fixed frame to components in the inertial frame as [24]:

$$ {}^{I}_{B}\mathbf{T} = \begin{bmatrix} \cos\theta\cos\Psi & \sin\theta\sin\phi\cos\Psi - \cos\phi\sin\Psi & \cos\phi\sin\theta\cos\Psi \\ \cos\theta\sin\Psi & \sin\phi\sin\theta\sin\Psi - \cos\phi\cos\Psi & \cos\phi\sin\theta\sin\Psi - \sin\phi\cos\Psi \\ -\sin\theta & \cos\theta\sin\phi & \cos\theta\cos\phi \end{bmatrix} \quad (5.19) $$

The 3rd column of the above rotation matrix gives the direction of the Z_b axis in the inertial frame [7], which is exactly what we need. The unit vector, in the direction of the Z_b axis, is given in the inertial frame of reference as:

$$ \hat{\mathbf{Z}}_B = (\cos\phi\sin\theta\cos\Psi)\hat{\mathbf{i}} + (\cos\phi\sin\theta\sin\Psi - \sin\phi\cos\Psi)\hat{\mathbf{j}} + (\cos\theta\cos\phi)\hat{\mathbf{k}} \quad (5.20) $$

The angle of attack of the platform is defined relative to the vertical sides of the platform (i.e. the side view) as shown in Figure 5.10.

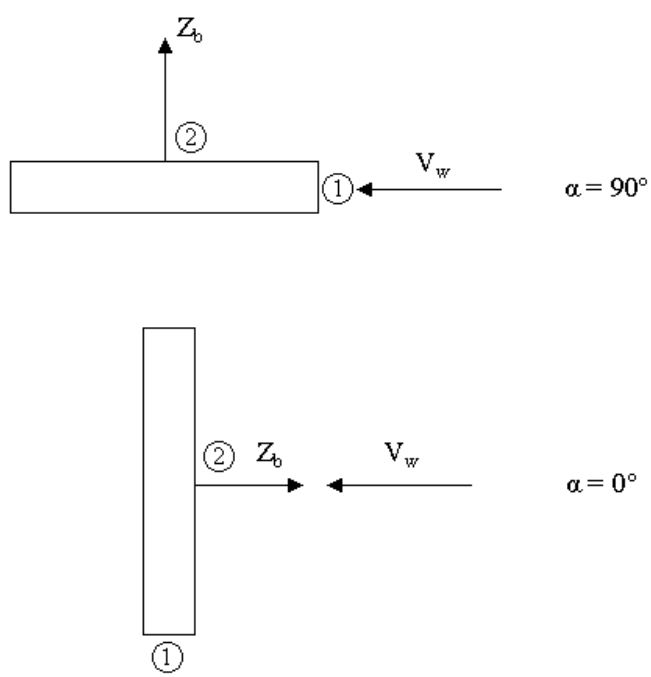

Figure 5.10 – Angle of Attack

The angle of attack is calculated as the angle between the unit vectors $\hat{\mathbf{Z}}_B$ and $\hat{\mathbf{V}}_w$. This angle is found by taking the dot product of the two unit vectors such that:

$$\alpha = \cos^{-1}\left(\frac{\hat{\mathbf{Z}}_B \bullet \hat{\mathbf{V}}_w}{\left|\hat{\mathbf{Z}}_B\right|\left|\hat{\mathbf{V}}_w\right|}\right) \tag{5.21}$$

We are now ready to evaluate the overall drag force acting on the platform at any given angle of attack. In theory, the angle of attack of the platform covers the range of 90 to 0 degrees. In reality the angle of attack relative to the vertical face of the truss is always very close to 90°. In other words, the drag of the platform will be due mainly to the vertical face of the platform normal to the wind. However we have still created a model capable of taking into account the entire range of angles of attack. This is done by varying the product of the coefficients of drag times their respective effective areas from one extreme value of α to the next. The reason for doing this is because the drag coefficients, $C_{D1}{}^{(2)}$ (for the side view) and $C_{D2}{}^{(2)}$(for the top view), are based on different effective areas. The way in which we vary this product of $C_D A$ is such that a smooth curve is generated by the following relation [21]. Figure 5.11 shows the variation of the product of $C_D A$ with angle of attack.

$$C_D A = (C_{D1}{}^{(2)} A_{1_{eff}})\sin^2\alpha + (C_{D2}{}^{(2)} A_{2_{eff}})\cos^2\alpha \tag{5.22}$$

The drag force acting on the platform at all angles of attack is treated as acting through the platform's centre of mass. Finally, for the "original" Arecibo configuration, the drag acting on the platform is given by:

$$D_{c\,of\,M} = D_p = \frac{1}{2}\rho_{air} V_w{}^2 (C_D A) \tag{5.23}$$

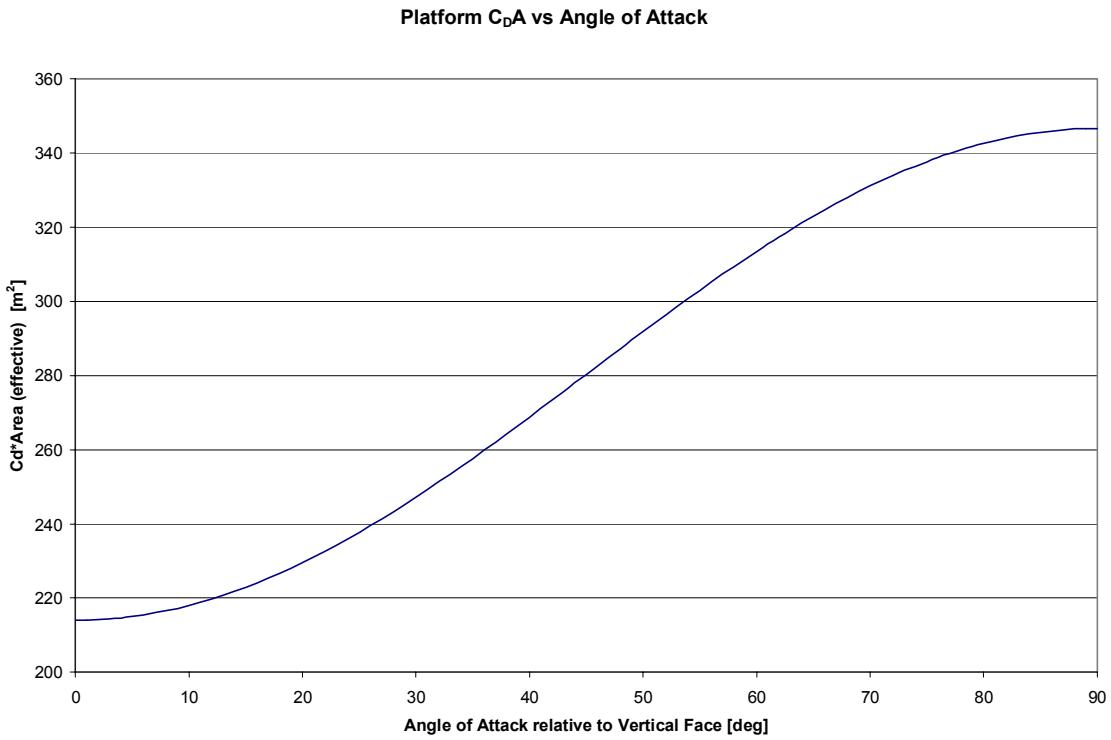

*Figure 5.11 – Platform Cd*A versus Angle of Attack*

5.5.5 Drag of Gregorian System

The drag coefficient of the Gregorian receiver is calculated based on the drag around a sphere. The model is used from Nahon's previous model of the LAR payload treated as a sphere. The Reynolds number (based on the diameter of the sphere) is important to the drag coefficients in this case, since the separation point of the flow may change with Reynolds number as shown in Figure 5.12.

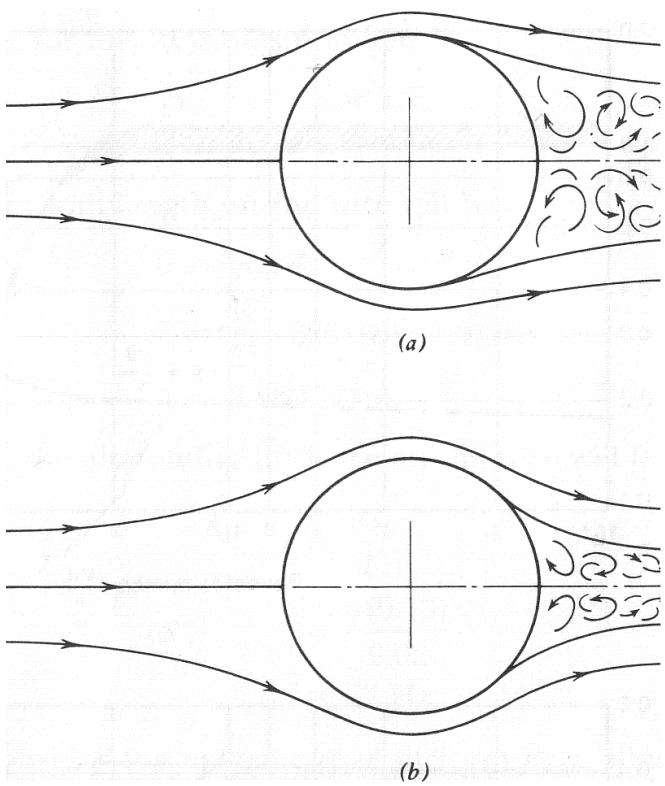

Figure 5.12 – Flow Around a Sphere for (a) Low Reynolds Number and (b) High Reynolds Number [20].

For the various ranges of Reynolds number (corresponding to laminar, transition, and turbulent flow) the following drag coefficients are used to calculate the drag force acting on the Gregorian receiver:

For $\mathrm{Re} > 631000$: $$C_{DG} = 0.15 \tag{5.24a}$$

For $251000 \le \mathrm{Re} \le 631000$: $$C_{DG} = 0.4 - 0.25 \times \frac{\log(\mathrm{Re}) - 5.4}{0.4} \tag{5.24b}$$

For $\mathrm{Re} < 251000$: $$C_{DG} = 0.4 \tag{5.24c}$$

The drag force on the Gregorian is then calculated based on:

$$D_G = \frac{1}{2} C_{DG} A_G \rho V_w^{\,2} \tag{5.25}$$

Where A_G is the cross sectional area of the sphere with diameter $d_G = 19.81m$:

$$\begin{aligned} A_G &= \frac{\pi d_G^{\ 2}}{4} \\ &= \frac{\pi(19.81m)^2}{4} \\ &= 308.22m^2 \end{aligned} \tag{5.26}$$

We only consider the drag of the Gregorian receiver when we are modeling the "upgraded" Arecibo configuration. For the "original" Arecibo configuration the drag caused by the narrow line feed is neglected as compared to the drag caused by the rest of the platform structure. A final note regarding the Gregorian drag is that it is treated as acting through the platform's centre of mass, thereby causing no moments on the platform. When modeling the "upgraded" Arecibo, the total drag force acting on the node located at the platform's centre of mass is given by:

$$D_{C\,of\,M} = D_P + D_G \tag{5.27}$$

5.6 Translational Motion

The translational motion of the platform is defined by the acceleration of its centre of mass, denoted here with the subscript G, in the inertial frame. The centre of mass of the platform is node #15 according to Figure 2.2. The equations of motion are governed by Newton's second law such that [22]:

$$\sum \mathbf{F} = m\mathbf{a}_G = \begin{cases} \sum F_x = m(a_G)_x \\ \sum F_y = m(a_G)_y \\ \sum F_z = m(a_G)_z \end{cases} \tag{5.28}$$

The sum of the forces acting on the centre of mass is the vector summation of the components of the forces acting on the platform. The forces acting on the platform include the cable forces (as considered in the cable dynamics section), the platform's

weight, and the aerodynamic drag (which is assumed to act through the platform's centre of mass). The cable forces are taken as those forces that would be acting at the nodes #5, 10, and 15 if they were each considered the last node of their respective cables. The last (and shared) node being the centre of mass of the platform is taken as having a mass equal to that of the entire platform; 550 000 kg. The acceleration of the platform's centre of mass, at a given instant in time, is then calculated by dividing the sum of the forces at that instant in time by the total platform mass. These accelerations are entered into the appropriate elements of $\dot{\mathbf{X}}(t)$; the derivative of the state vector.

5.7 Rotational Motion

The LAR model, from which the Arecibo model is developed, considers its "payload" (equivalent to Arecibo's platform) to be spherical and subject only to translational motion. We will now consider the effect of the moments caused by the forces acting at a particular location on the platform. In order to do so, the platform is first converted from a point mass to a rigid body, and the cable-platform attachment points are defined (Section 5.4). A rigid body is such that its changes in shape may be neglected as compared to the overall dimensions of the body [17]. The platform is defined in space by not only the position of its centre of mass, but also by its orientation. The platform must satisfy Euler's rotational equations of motion given by [25]:

$$\vec{M}_{CM} = \vec{I}_{CM}\dot{\vec{\omega}} + \vec{\omega} \times \vec{I}_{CM}\vec{\omega} \tag{5.29}$$

Before discussing the strategy for setting up and numerically solving Euler's rotational equations of motion, we will first consider the definition of the Euler angle set as well as the transformations required between the body-fixed and inertial coordinate systems.

5.7.1 The Z-Y-X Euler Angles

A new set of state variables, in the inertial frame, are defined to account for the platform's orientation and rotational motion in space; $(\dot{\Phi},\Phi,\dot{\theta},\theta,\dot{\Psi},\Psi,)$. That is, the platform's state (in general) is completely defined by its position and velocity, and also by its orientation, and angular velocity. As is commonly used in Aeronautics and Flight Mechanics [20], the Z-Y-X Euler angle set is used in the Arecibo model. The main difference from the Z-Y-X angle set as used in flight mechanics is the orientation of the Z-axis (which is pointed toward the earth in flight mechanics [23] but is pointed toward the sky for the Arecibo Radio Telescope). The orientation of the platform is given by the Z-Y-X Euler angles of Φ,θ,Ψ using the following procedure (taken directly from [24]) and is also shown schematically in Figure 5.13

(i) Rotation by an angle Ψ about the inertial Z-axis

(ii) Rotation by an angle θ about the resulting Y-axis (from the previous rotation)

(iii) Rotation by an angle Φ about the resulting X-axis (from the previous rotation)

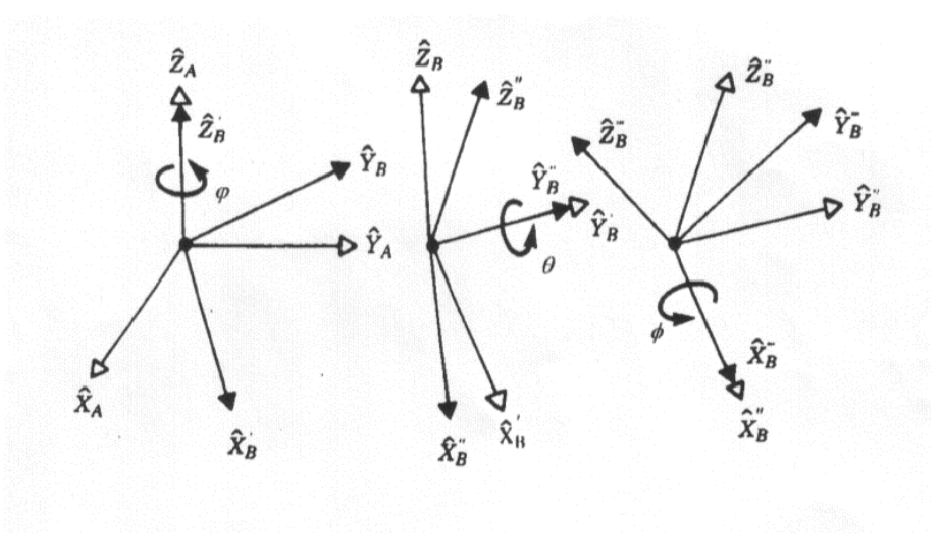

Figure 5.13 – Using the Z-Y-X Euler Angle Set [24]

Note that using the right hand rule gives the directions for positive angles of rotation. Care should be taken here since the final orientation of the platform does in fact depend on which order these rotations take place. With no aerodynamic forces or initial perturbations acting on the platform the inertial and body-fixed frames will remain aligned and the Euler angles will all be zero [20].

5.7.2 Transformations

In the body-fixed frame the angular velocities are defined as p, q, and r as shown in Figure 5.14. We must define the transformation matrices for both vector and rotational parameters in order to allow us to move back and forth from the body-fixed to the inertial frame as required. For example, this is necessary when the cable-platform attachment points are defined in the body-fixed frame and their coordinates are required in the inertial frame of reference. Since the platform is treated as a rigid-body, these inertial coordinates are determined from the Euler angle set. The transformation matrices have been used in the simulation of a multi-tethered aerostat system by Zhao [24]. The following equations, transformations, and conventions are taken directly from this work.

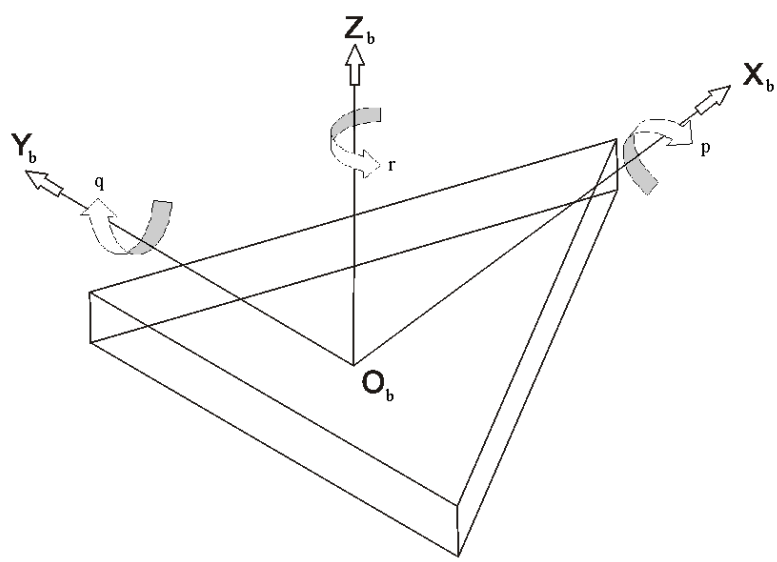

Figure 5.14 – Angular Velocities in the Platform's Body-Fixed Frame

The rotation matrix that brings a vector's components in the body-fixed frame to components in the inertial frame is given by [24]:

$$\begin{bmatrix} x_i \\ y_i \\ z_i \end{bmatrix} = {}^{I}_{B}\mathbf{T} \begin{bmatrix} x_b \\ y_b \\ z_b \end{bmatrix} \tag{5.30}$$

Where:

$${}^{I}_{B}\mathbf{T} = \begin{bmatrix} \cos\theta\cos\Psi & \sin\theta\sin\phi\cos\Psi - \cos\phi\sin\Psi & \cos\phi\sin\theta\cos\Psi \\ \cos\theta\sin\Psi & \sin\phi\sin\theta\sin\Psi - \cos\phi\cos\Psi & \cos\phi\sin\theta\sin\Psi - \sin\phi\cos\Psi \\ -\sin\theta & \cos\theta\sin\phi & \cos\theta\cos\phi \end{bmatrix} \tag{5.31}$$

The lower and upper subscripts of B and I indicate that the given rotation matrix is used when going from the body-fixed to the inertial coordinate systems. Notice that the rotation matrix used in the cable model Equation 3.2 is obtained from the above rotation matrix, Equation 5.31, by setting $\Psi = 0$ [24].

To move from vector components in the inertial frame to the body-fixed frame the inverse of the rotation matrix is required and obtained by the transpose of ${}^{I}_{B}\mathbf{T}$, since the rotation matrix is orthogonal:

$${}^{B}_{I}\mathbf{T} = {}^{I}_{B}\mathbf{T}^{-1} = {}^{I}_{B}\mathbf{T}^{T} \tag{5.32}$$

$${}^{B}_{I}\mathbf{T} = \begin{bmatrix} \cos\theta\cos\Psi & \cos\theta\sin\Psi & -\sin\theta \\ \sin\theta\sin\phi\cos\Psi - \cos\phi\sin\Psi & \sin\phi\sin\theta\sin\Psi - \cos\phi\cos\Psi & \cos\theta\sin\phi \\ \cos\phi\sin\theta\cos\Psi & \cos\phi\sin\theta\sin\Psi - \sin\phi\cos\Psi & \cos\theta\cos\phi \end{bmatrix} \tag{5.33}$$

Finally, we must also form the transformation matrix that will allow us to move back and forth between the time derivatives of the Euler angles in the inertial frame and the angular velocities p, q, and r of the platform in the body-fixed frame.

$$\begin{bmatrix} \dot{\phi} \\ \dot{\theta} \\ \dot{\Psi} \end{bmatrix} = \mathbf{T}_w \begin{bmatrix} p \\ q \\ r \end{bmatrix} \tag{5.34}$$

Where:

$$\mathbf{T}_w = \begin{bmatrix} 1 & \sin\phi\tan\theta & \cos\phi\tan\theta \\ 0 & \cos\phi & -\sin\phi \\ 0 & \sin\phi/\cos\theta & \cos\phi/\cos\theta \end{bmatrix} \tag{5.35}$$

The inverse transformation, which allows us to obtain the angular velocities of the platform from the time derivative of the Euler angles, is given by:

$$\mathbf{T}_w^{-1} = \begin{bmatrix} 1 & 0 & -\sin\theta \\ 0 & \cos\phi & \cos\theta\sin\phi \\ 0 & -\sin\phi & \cos\theta\cos\phi \end{bmatrix} \tag{5.36}$$

A different set of Euler angles using the Z-Y-Z convention was initially developed for the Arecibo platform. However, since the transformation matrix, $\mathbf{T}_w$, in Z-Y-Z convention becomes degenerate whenever $\sin\theta = \theta = 0$, problems arose in trying to avoid that particular condition. If we instead use the Z-Y-X Euler angle set, we see that the transformation matrix, $\mathbf{T}_w$, in this case becomes degenerate whenever $\cos\theta = 0$ or $\theta = 90^\circ$, however this case is never physically realized by the Arecibo platform. Hence, the Z-Y-X convention has been chosen to model the platform's rotation.

5.7.3 Rotational Equations of Motion

The equation that governs the platform's rotation is known as Euler's equations of motion, and is given by [22]:

$$\vec{M} = \vec{I}\dot{\vec{\omega}} + \vec{\omega} \times \vec{I}\vec{\omega} \tag{5.37}$$

The moments acting on the Arecibo platform must be evaluated in order to solve Euler's rotational equations of motion numerically. As previously mentioned, the aerodynamic drag of the platform is assumed to act through the platform's centre of mass, meaning that the wind force on the truss section does not apply any moment to the platform. The cable-platform attachment points however do indeed cause a moment, which is taken into account in the following manner:

(i) Sum the cable forces acting along the q-axis in the *cable* body-fixed frame.

(ii) Transform these forces (acting along the cable q-axis) to the inertial frame of reference and resolve the forces of the three mainstay cables into their inertial components

(iii) Transform the resulting sum of inertial force components into the *platform's* body-fixed frame of reference.

(iv) Find the components of the moments acting on the platform (in the platform-fixed frame) using the components of $\mathbf{M} = \sum \mathbf{r}_i \times \mathbf{F}_i$.

We wish to calculate $\dot{\vec{\omega}}$, the time derivative of the angular velocity vector, which will be transformed into the second derivative of the Euler angles with respect to time. These accelerations along with first derivative of the Euler angles will form the last six elements of $\dot{\mathbf{X}}(t)$; the derivative of the state vector. As discussed in Section 2.3, the numerical integration scheme may then be applied in a step-wise manner in time, to observe the rotational motion of the platform. In order to calculate $\dot{\vec{\omega}}$ at a given instant, we first calculate the angular velocities of the platform in its body-fixed frame using the known first derivatives of the Euler angles (from the state vector):

$$\vec{\omega} = \mathbf{T}_w^{-1} \begin{bmatrix} \dot{\phi} \\ \dot{\theta} \\ \dot{\Psi} \end{bmatrix} \tag{5.38}$$

Rearranging Equation 5.37 we have:

$$\vec{I}\dot{\vec{\omega}} = \vec{M} - \vec{\omega} \times \vec{I}\vec{\omega} \tag{5.39}$$

The terms on the right hand side of the equation are known. Hence, we obtain:

$$\dot{\vec{\omega}} = \vec{I}^{-1}(\vec{I}\dot{\vec{\omega}}) = \vec{I}^{-1}(\vec{M} - \vec{\omega} \times \vec{I}\vec{\omega}) \tag{5.40}$$

Finally, the second derivatives of the Euler angles are found by applying the chain rule to Equation 5.34:

$$\begin{bmatrix} \ddot{\phi} \\ \ddot{\theta} \\ \ddot{\Psi} \end{bmatrix} = \mathbf{T}_w \dot{\vec{\omega}} + \dot{\mathbf{T}}_w \vec{\omega} \tag{5.41}$$

To summarize the entire dynamics model description of Chapters 3 to 5, Figure 5.15 shows a flow diagram of the overall process required to obtain the time derivative of the state vector $\dot{\mathbf{X}}(t)$, which is then sent to the Runge-Kutta integration scheme.

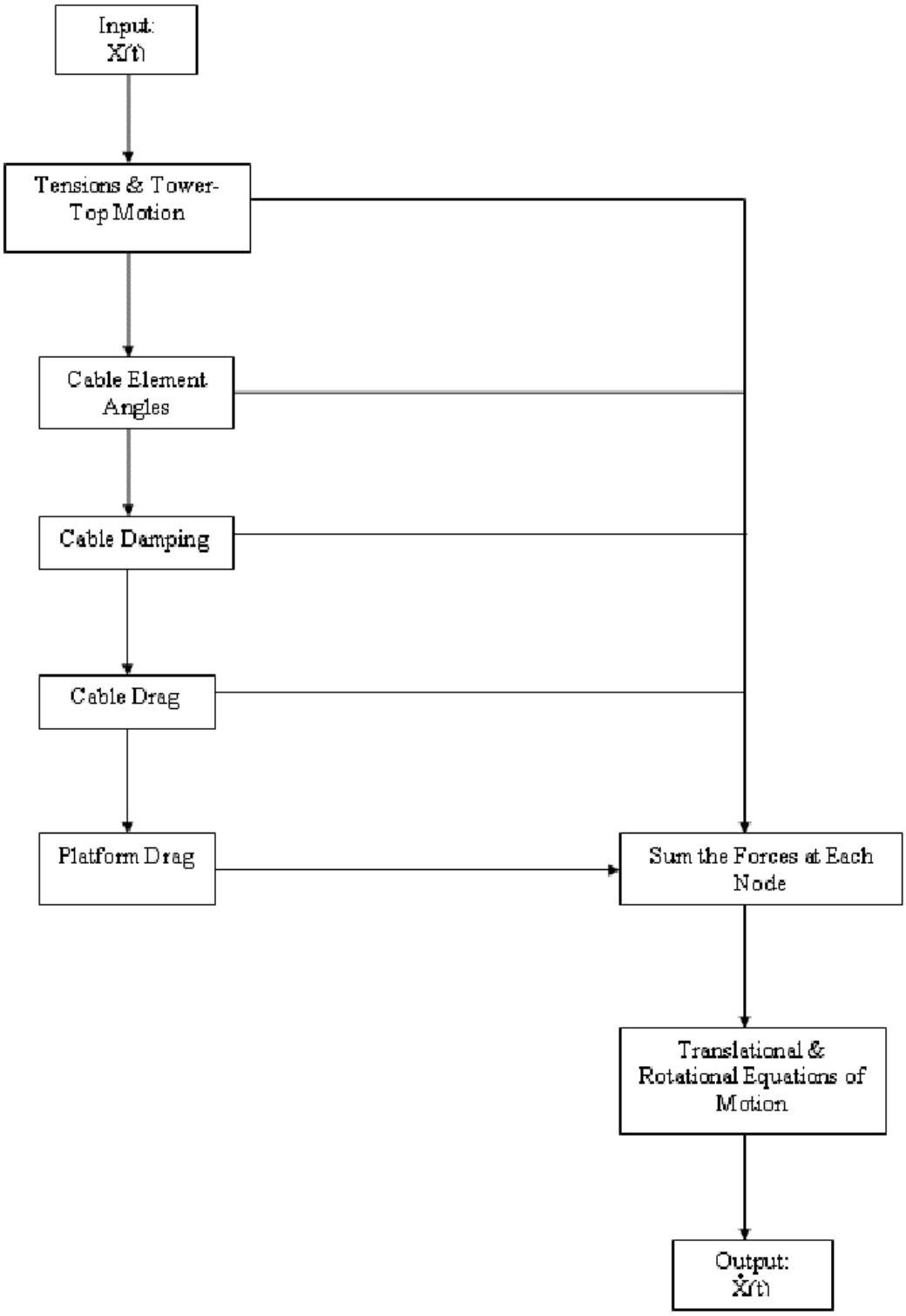

Figure 5.15 – Dynamics Model Flowchart

Chapter 6 – Performance Evaluation

6.1 Introduction

The performance evaluation of the Arecibo Radio Telescope is a most valuable exercise that will help us assess the dynamic performance of the system as well as demonstrate the capabilities of our computer model. We begin by explaining how the "performance" of the Arecibo Radio Telescope is defined. We may then use our model to observe (over time) the motion, performance metrics, and other parameters of interest of the Arecibo Radio Telescope under turbulent and non-turbulent wind conditions at a variety of wind speeds and directions. In fact, if we include the sensitivity analysis carried out in Chapter 7, the Arecibo model has been subjected to more than 80 different dynamic test cases which consider a variety of system configurations and wind conditions. The output and results will be presented in the form of tables and figures.

6.2 Performance Metrics

In order to evaluate the performance of the Arecibo system we must first understand what "performance" actually means in terms of the system's motion. A performance metric is defined as a parameter that allows us to quantitatively evaluate the system's performance. Important to the astronomer are the positional and rotational error of the system's receiver/transmitter (to and from which the electromagnetic radio waves reflect from the collector dish). The receiver is defined in our model as the centre of mass of the platform (node #15 in Figure 2.2). To the satisfaction of Steve Torchinsky [25] (Head of Astronomy at the Arecibo Observatory) the following parameters have been chosen to quantitatively define the dynamic performance of the Arecibo Radio Telescope:

(i) Error of the receiver position in the focal plane

(ii) Error of the receiver position out of the focal plane

(iii) Tilt angle of the receiver relative to the inertial Z-axis.

The so-called "focal plane" is defined as the plane locally tangent to a hemisphere [6] of radius equal to the platform's static equilibrium height above the bottom-centre of the collector dish (i.e. the origin in the inertial frame). Since the triangular truss platform does not itself take on any azimuth or zenith angles, the focal plane is in fact always horizontal. Figure 6.1 shows the hemisphere as defined.

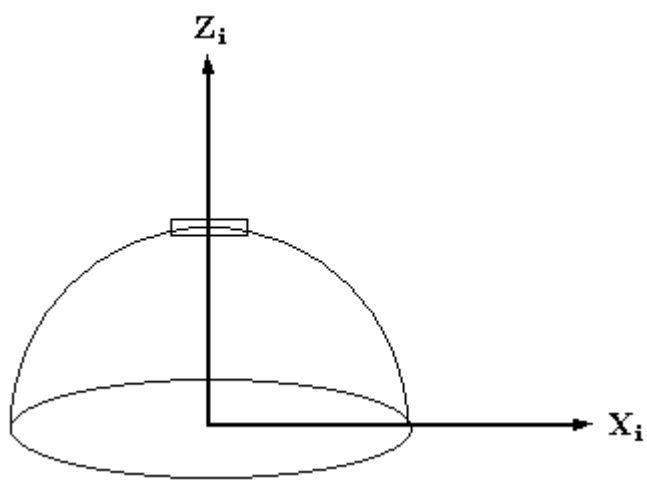

Figure 6.1 – The Focal Plane and Hemisphere

The error *out* of the focal plane at any instant is calculated based on the difference between the platform's actual height and the height of the focal plane (which, to re-emphasize, is the platform's height when resting at static equilibrium):

$$Error_{out} = Z_{CM} - Z_{focal\ plane} \tag{6.1}$$

The error out of the focal plane is taken as positive if the platform is outside of the hemisphere (above the focal plane) and negative when the platform is located inside the hemisphere (below the focal plane).

The error *in* the focal plane at any instant is calculated as the radius of the platform's horizontal displacement in the focal plane. The error in the focal plane is always a positive quantity and is best visualized if one where looking directly down on the platform from high above it.

$$Error_{in} = \sqrt{X_{CM}{}^2 + Y_{CM}{}^2} \tag{6.2}$$

Finally, we define the tilt angle (denoted by β) as the angle between the platform's Z_{ebu}-axis (in its own body-fixed frame) and the inertial Z_{ip}-axis (which always points straight up), as shown in Figure 6.2.

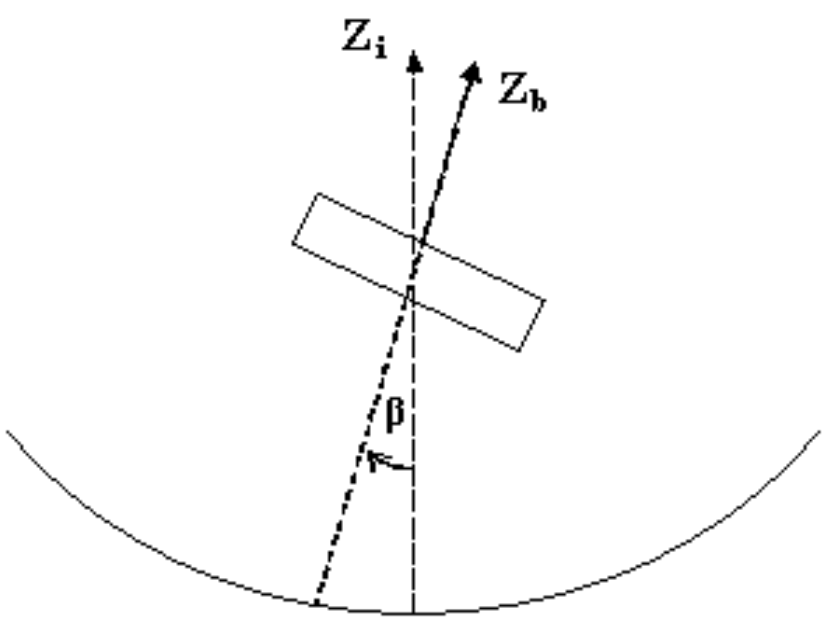

Figure 6.2 – Tilt Angle Performance Metric

In order to calculate β, we use the same technique as that used to calculate the platform's angle of attack in Section 5.5.2. That is, we use the rotation matrix that brings any vector from the body-fixed coordinate system to the inertial coordinate system. The third column of this rotation matrix represents the components of the unit vector in the direction of the platform's body-fixed Z_{ebu}-axis. This unit vector is given in the inertial frame by equation (5.20) as:

$$\hat{\mathbf{Z}}_B = (\cos\phi\sin\theta\cos\Psi)\hat{\mathbf{i}} + (\cos\phi\sin\theta\sin\Psi - \sin\phi\cos\Psi)\hat{\mathbf{j}} + (\cos\theta\cos\phi)\hat{\mathbf{k}} \qquad (6.3)$$

The unit vector in the direction of the inertial Z_{ip}-axis is given by:

$$\hat{\mathbf{Z}}_I = 0\cdot\hat{\mathbf{i}} + 0\cdot\hat{\mathbf{j}} + \hat{\mathbf{k}} \qquad (6.4)$$

The tilt angle is then found be evaluating the dot product of the above unit vectors:

$$\beta = \cos^{-1}\left(\frac{\hat{\mathbf{Z}}_B \bullet \hat{\mathbf{Z}}_I}{\left|\hat{\mathbf{Z}}_B\right|\left|\hat{\mathbf{Z}}_I\right|}\right) \qquad (6.5)$$

$$\beta = \cos^{-1}(\cos\theta\cos\phi) \qquad (6.6)$$

The tilt angle is directly related to the so-called "pointing accuracy" (PA) of the receiver using the following approximation:

$$PA = Z_{i_{CM}} \tan\beta \qquad (6.7)$$

Where $Z_{i_{CM}}$ is the elevation of the platform's center of mass in the inertial frame of reference. However, the tilt angle itself has been chosen as the performance metric, while the pointing accuracy may be subsequently found using equation 6.7 if so desired.

6.3 Additional Parameters of Interest

Aside from the performance metrics, there are often additional parameters that may be of interest, perhaps to a structural engineer, rather than to the astronomer. The parameters observed in addition to the performance metrics include the tension force in the cables as well as the tower-top deflections. All tensions, unless stated otherwise, are presented for the entire effective area of the mainstay cables. That is, the values in the plots that follow must be divided by the number of mainstay cables in order to find the tension per cable. Furthermore, the tension forces quoted are those acting specifically in the first cable elements (#1, 6, and 11 as per Figure 2.2). The tower deflections are given in the horizontal plane of motion of the tower-tops relative to their equilibrium position. The deflections are considered positive if the tower is brought closer to the centre of the system (i.e. due to an increase in tension) and negative if the opposite is true.

6.4 Indicators

There are three different indicators that are used in comparing the results of the various test cases. These indicators are the average, the root-mean-square, and the peak values of the performance metrics and/or additional parameters of interest over the total sampling time. The average value of a metric, X, is the sum of that metric from time t_o to t_f divided by the number of times it was sampled/stored.

$$X_{avg} = \frac{\sum_{1}^{n} X}{n} \tag{6.8}$$

For example, if the simulation run time is set for 10 seconds and the value of the metric is stored in an array every 0.1 seconds, then in this case the value of "n" would be equal to 100. Next we define the root-mean-square for our purposes to be:

$$X_{RMS} = \sqrt{\frac{1}{n}\sum_{1}^{n}(X - X_{avg})^2} \tag{6.9}$$

Finally, the peak value of the metric is simply defined as the maximum error encountered over the given period of time. If the max error is in fact negative, than the peak error is also taken as negative:

$$X_{peak} = X_{\max} \tag{6.10}$$

6.5 Arecibo Model Configuration

Before presenting any results from the test cases, it will be made clear exactly which physical configurations of the telescope are being simulated and how they differ from the actual Arecibo Radio Telescope. Table 6.1 gives the details of the "original" Arecibo model and how it differs from the actual Arecibo construction. The entire performance evaluation and sensitivity analysis has been performed on the original Arecibo configuration. The upgraded configuration is presented immediately following the performance evaluation (in Section 6.8) in order to assess the impact of some of the recent design changes made to the Arecibo Radio Telescope.

	Actual Construction of the Original Arecibo	**Model of the Original Arecibo**
platform mass	550 000 kg	550 000 kg
receiver drag	Line Feed	Line feed neglected
Mainstay Cables	4 cables per tower d = 3"	4 cables per tower d = 3"
Backstay Cables	5 cables per tower d = 3.25"	5 cables per tower d = 3.25"
Main Auxiliary Cables	N/A	N/A
Backstay Auxiliary Cables	N/A	N/A
Tie Down Cables	6 cables total d=1.5" Two off-vertical cables (functioning as catenaries) run from each corner of the platform and anchored near the rim of the reflector [5]	N/A

Table 6.1 – The Original Arecibo Configuration

6.6 Equilibrium Condition

An important feature of the Arecibo model is the equilibrium condition of the system. This condition must be reached before subjecting the system to various wind configurations. Given the specific physical parameters of a given configuration of interest, the system is initially (at time = 0 seconds) released from the unstretched length configuration shown in Figure 3.2. The system's motion will eventually damp out over time and settle at its equilibrium height and orientation. The following Figures show how the performance metrics vary over the first 400 seconds of the total 1500 seconds required for the original Arecibo configuration to come to equilibrium. The reason for letting the system run for 1500 seconds is to ensure that the vertical motion is of the order of millimeters or less (if possible) before subjecting the system to the various wind conditions. Notice that the platform remains level and centered as it oscillates in a vertical motion. In reality, upon initial construction, the supporting cables of the Arecibo structure were all pre-tensioned prior to lifting the platform into the desired position [13]. The tower-top radial distances from the centre of the collector dish are also plotted versus time as they reach their equilibrium values in the simulation. The tower numbering is explained in the next section through Figure 6.5

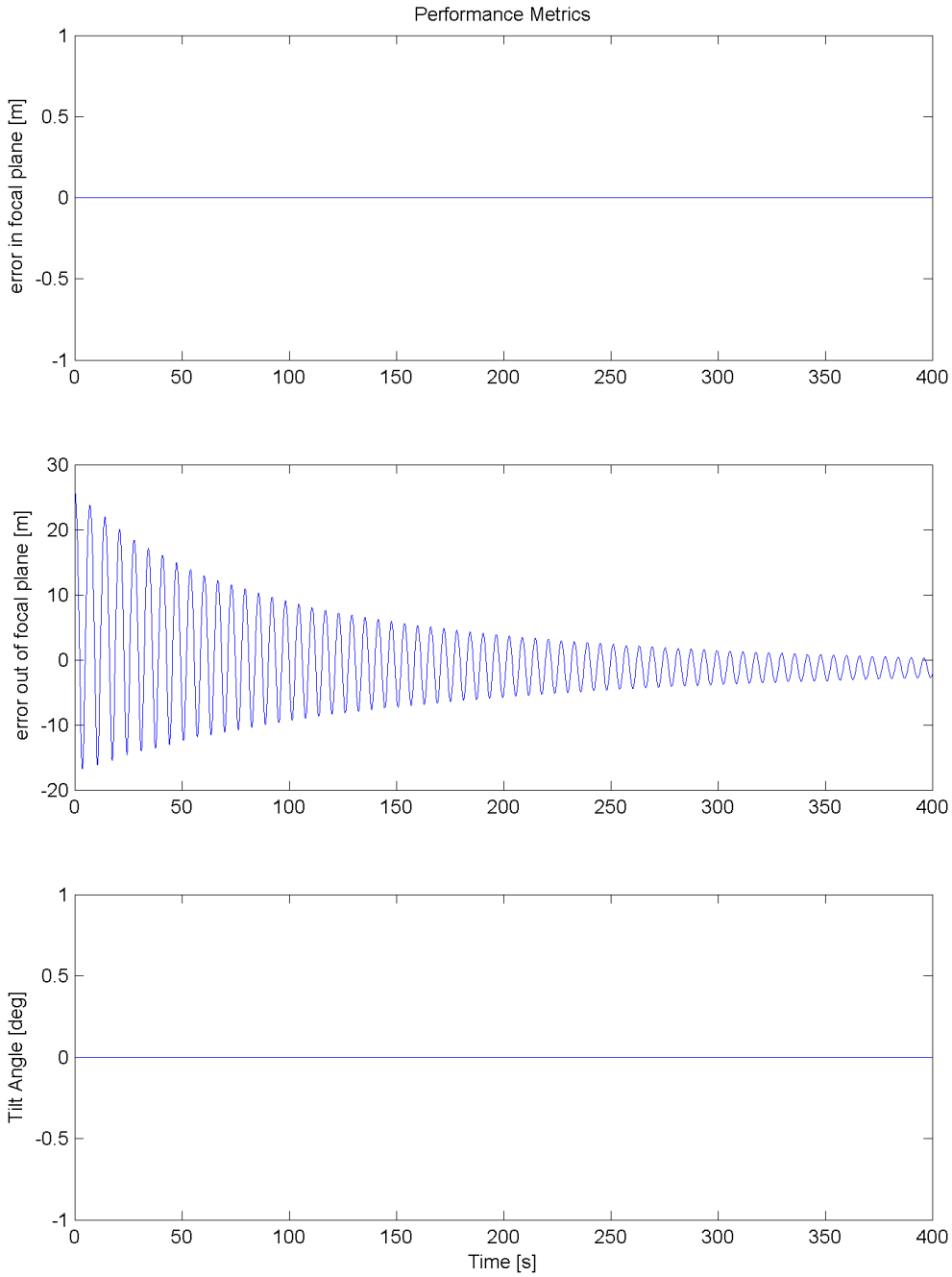

Figure 6.3 – Performance Metrics to Equilibrium

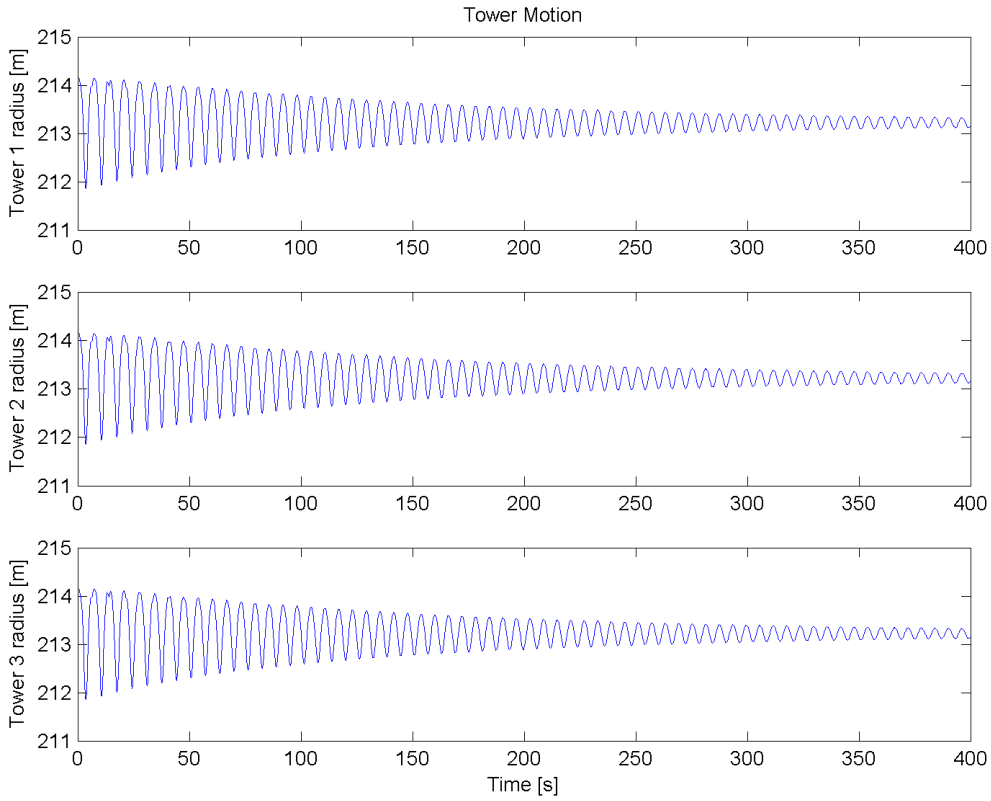

Figure 6.4 – Tower-Top Positions to Equilibrium

6.7 Dynamic Runs

In this section, we discover the quality and variation in the performance of Arecibo under a variety of wind speeds, wind directions, and turbulence. All test cases are carried out on the original Arecibo model. We define the wind direction as is shown in Figure 6.5. A wind direction of 0° implies the wind is directed toward positive infinity on the inertial X_i-axis.

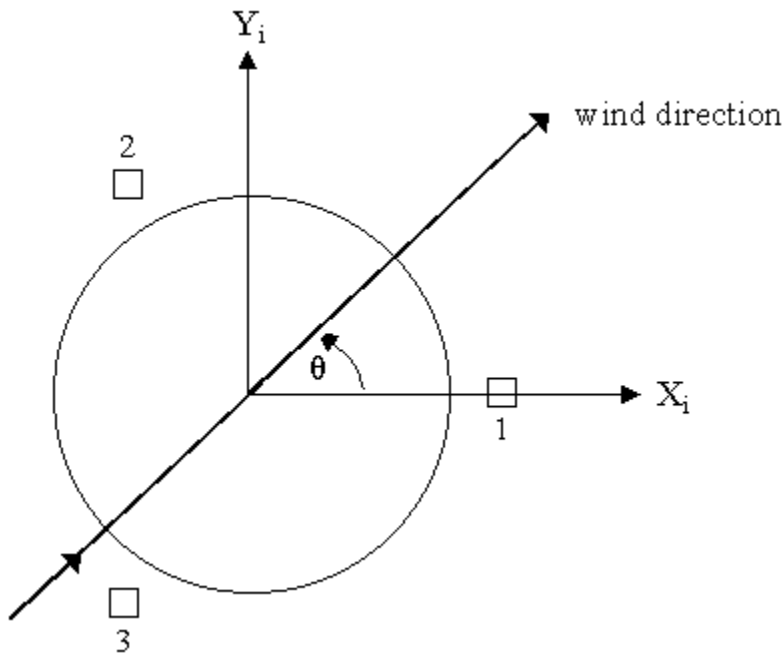

Figure 6.5 – Wind Direction and Tower Numbering

6.7.1 Effect of Wind Speed

In varying the wind speed, we keep the wind direction constant at 0° and consider no turbulent wind effects. We wish to determine the magnitude of motion and the performance metrics with increasing wind speeds. The range of wind speeds used was 0-30 m/s. The first real proof of the Arecibo Radio Telescope's stability was on August 28, 1966, when the system remained stable while encountered by up to 70 mile per hour (30 m/s) winds caused by the passing of Hurricane Inez [13]. We also know that wind speed of up to 17 miles per hour (7.6 m/s) cause "no significant displacement of the structure" [5]. Significant displacement of the structure is considered to be of the order of millimeters [2], which is quite impressive for such a massive structure. Table 6.2 shows the test matrix used for the wind speed evaluation.

Test #	Wind Speed	Wind Direction	Turbulence
	m/s	deg	
1	0	0	No
2	1	0	No
3	2	0	No
4	3	0	No
5	4	0	No
6	5	0	No
7	6	0	No
8	7	0	No
9	8	0	No
10	9	0	No
11	10	0	No
12	11	0	No
13	12	0	No
14	13	0	No
15	14	0	No
16	15	0	No
17	20	0	No
18	25	0	No
19	30	0	No

Table 6.2 – Wind Speed Test Matrix

For each of the above test cases, the simulation was run for 70 seconds and the wind was increased gradually to its full speed in the first second (t = 0.1 to 1.1 seconds). The following figures show the variation of the performance metrics with wind speed:

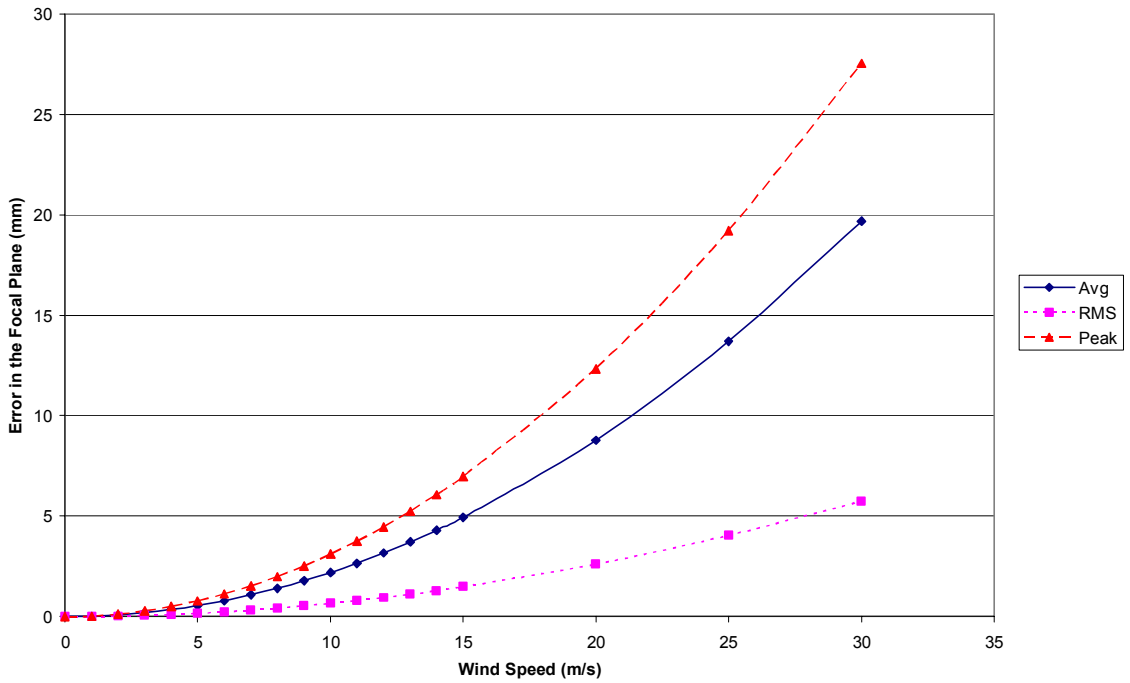

Figure 6.6a - Error in the Focal Plane vs Wind Speed

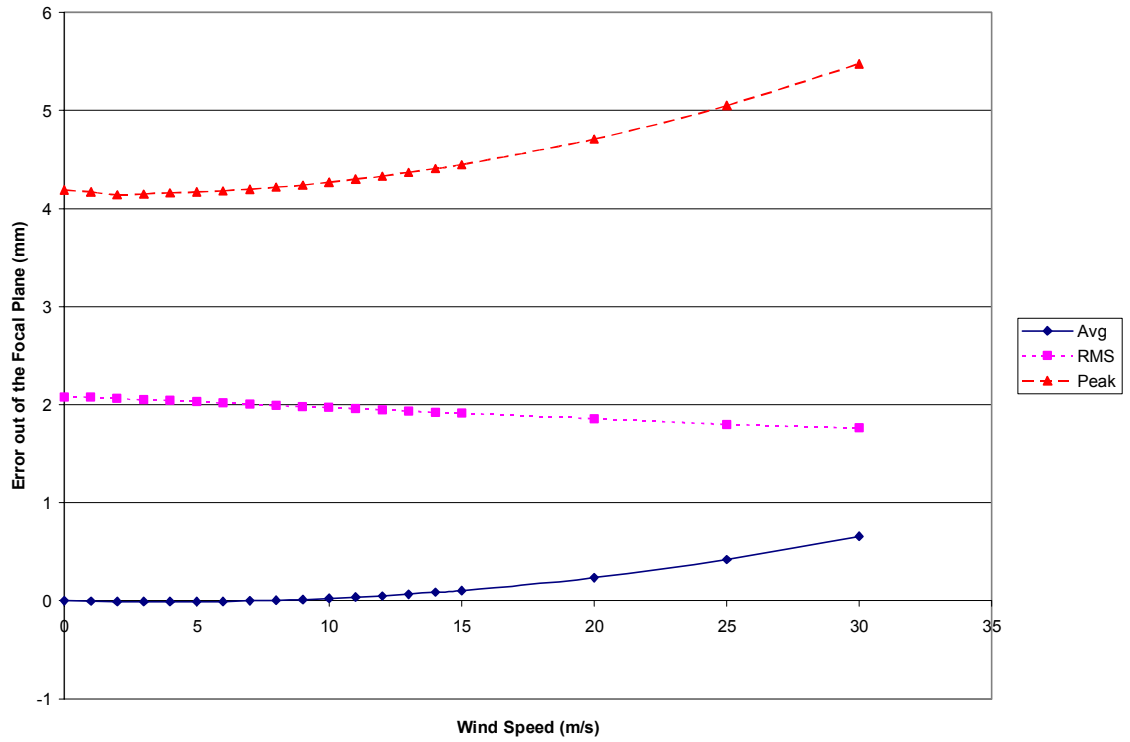

Figure 6.6b - Error Out of the Focal Plane vs Wind Speed

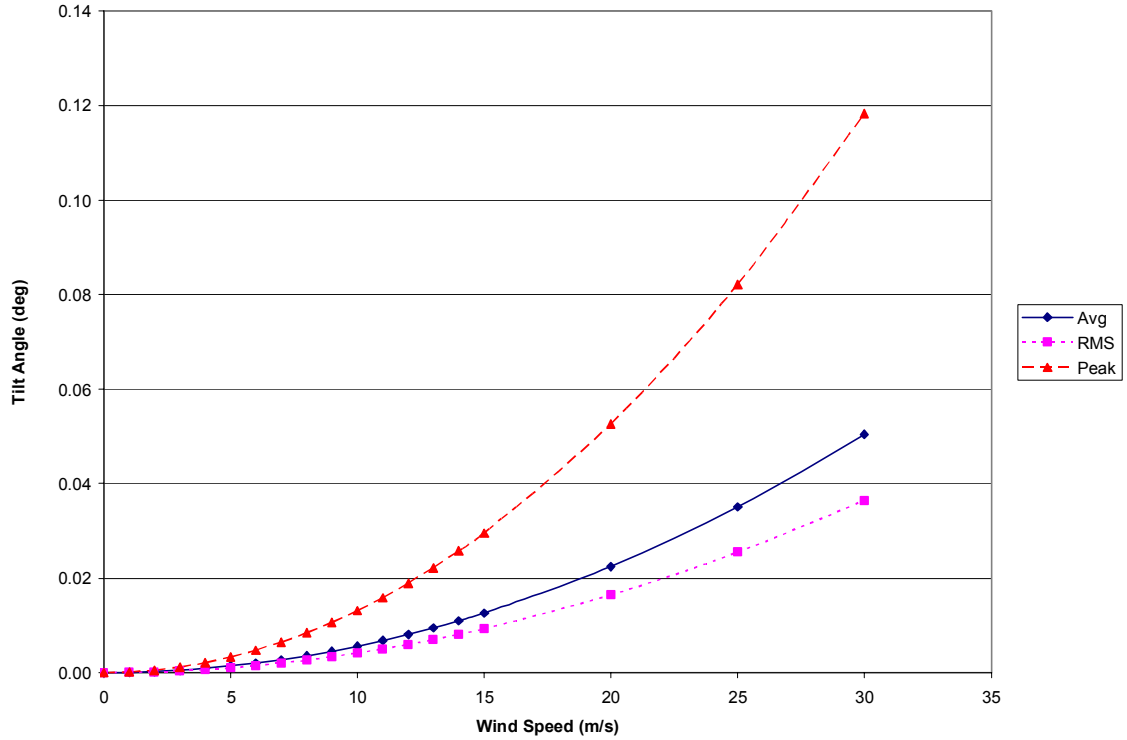

Figure 6.6c - Platform Tilt Angle vs Wind Speed

We notice that the error in the focal plane as well as the tilt angle seem to fit a quadratic shaped curve with increasing wind speed, and that the error out the focal plane is rather insignificant. We can also conclude that the original Arecibo model, even at high wind speeds, is subject to motion on the order of centimeters or tens of millimeters. The tilt angle is also very small at an average of approximately 0.02° (or $3.5\times10^{-4}\,rad$) even at 20 m/s wind speeds. At this wind speed the tilt angle is in fact greater than the desired and "ambitious goal" (but not required) of $2.4\times10^{-5}\,rad$ [5]. The peak tower deflection, even at the hurricane wind speed of 30 m/s, was found to be 6.2 mm which is well within the permissible limit of 2 inches, or 50.8 mm [13].

6.7.2 Effect of Wind Direction

The effect of wind direction was tested at a constant wind speed of 10 m/s and with no turbulent conditions. The wind direction was increased from 0° to 120° in increments of 15°. The following figures present the performance metrics versus wind direction for the original Arecibo model.

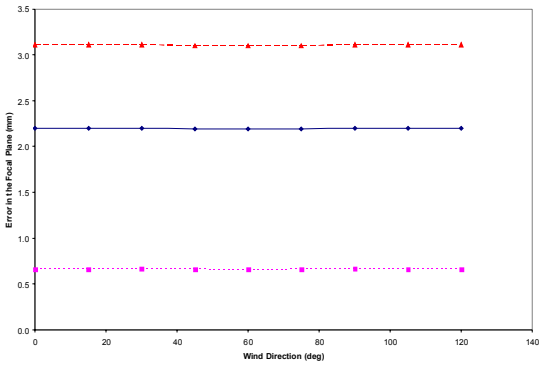

Figure 6.7a - Error In the Focal Plane vs Wind Direction

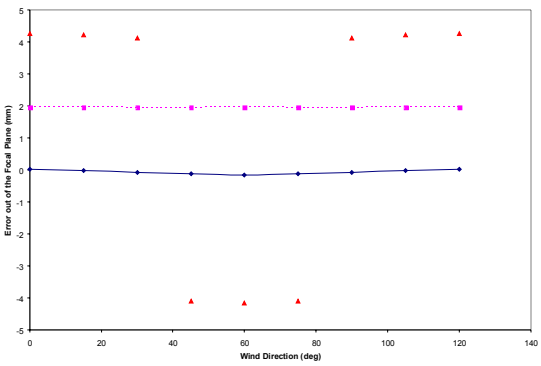

Figure 6.7b - Error Out of the Focal Plane vs Wind Direction

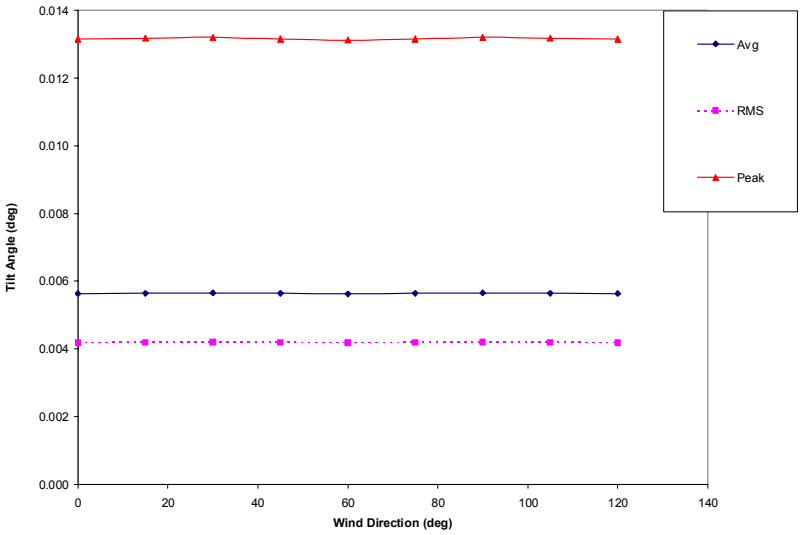

Figure 6.7c - Platform Tilt Angle vs Wind Direction

The above figures show that the wind direction has little effect on the performance of the system. It is interesting however to observe the cable tensions and tower-top deflections versus wind direction. The following figures show the symmetry of the system as the wind direction changes from 0° along the T1 radial line and 120° along the T2 radial line. Notice that at exactly 60° the tension in the first cable elements of T1 and T2 are equal while the tension in T3 is at its maximum value (demonstrating a form of symmetry). Also note that the tower-top deflections (denoted B1, B2, B3 corresponding to towers T1, T2, T3, respectively) follow an identical symmetry as the tension.

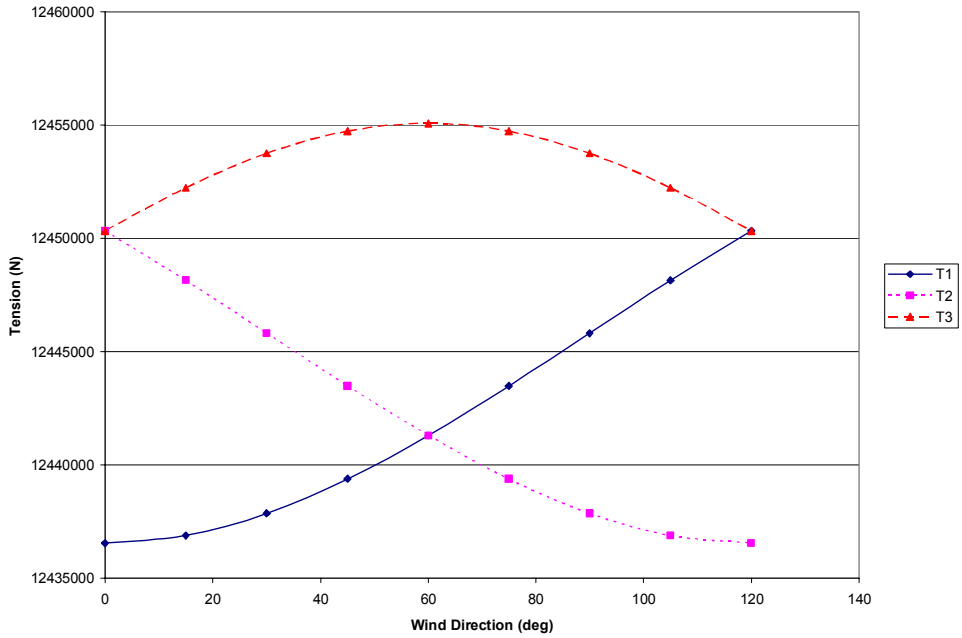

Figure 6.7d - Average Cable Tension vs Wind Direction

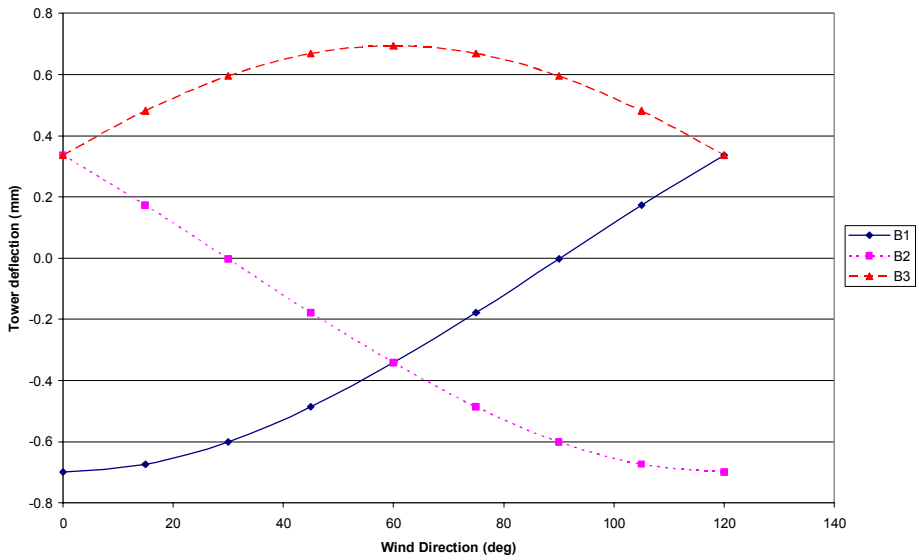

Figure 6.7e - Average Tower Deflection vs Wind Direction

6.7.3 Effect of Turbulence

Both the wind and the turbulence model employed herein are taken from the wind and turbulence model used in the LAR system. For details regarding the turbulence model, the reader is referred to [6] in which it is stated that the turbulent gusts, imposed on the mean wind, "were generated with the desired gust statistical properties, including turbulence intensity, scale length, and spectra". The turbulence model acts to vary the wind speed above and below its mean value in an intentionally random manner. The effects of the turbulent wind conditions are evaluated by considering the wind direction constant at 0° and varying the mean wind speed from 0 to 15 m/s. The turbulent results are superimposed onto the results obtained for the same constant wind speed for a basis of comparison. The following figures show the performance metrics in turbulent conditions.

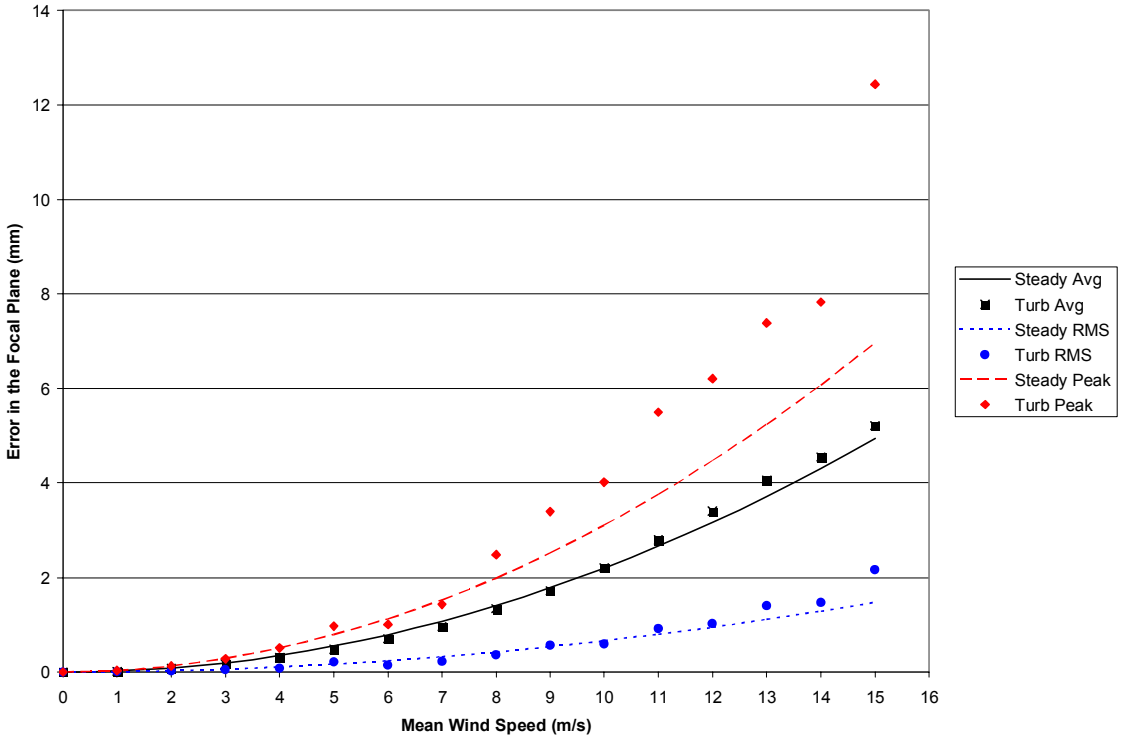

Figure 6.8a - Error in the Focal Plane vs Turbulent Mean Wind Speed

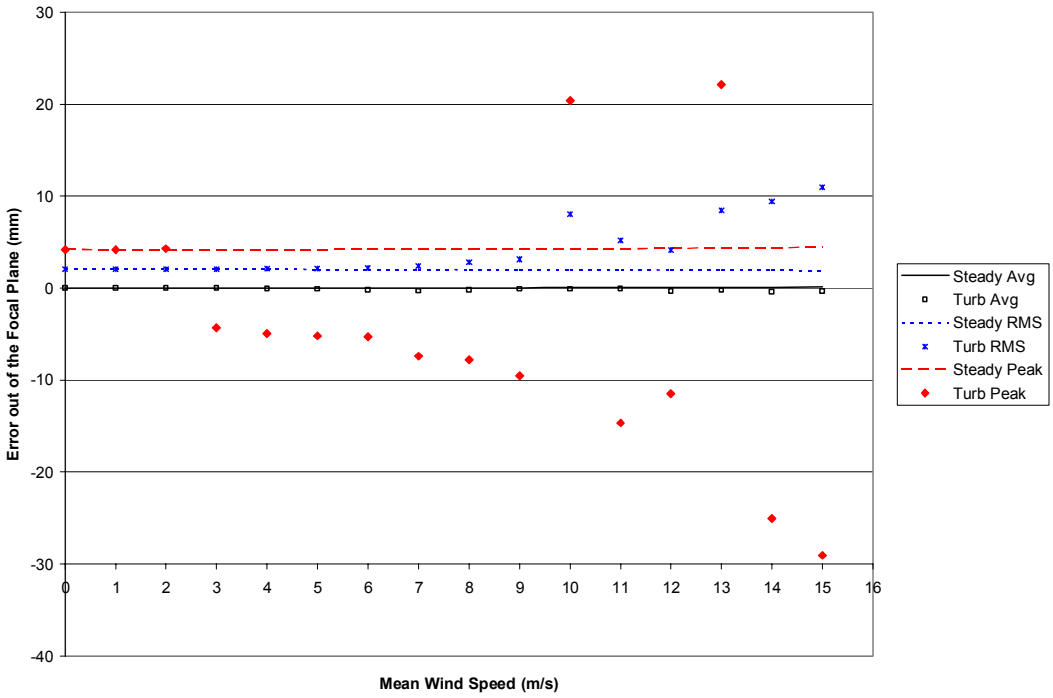

Figure 6.8b - Error out of the Focal Plane vs Turbulent Mean Wind Speed

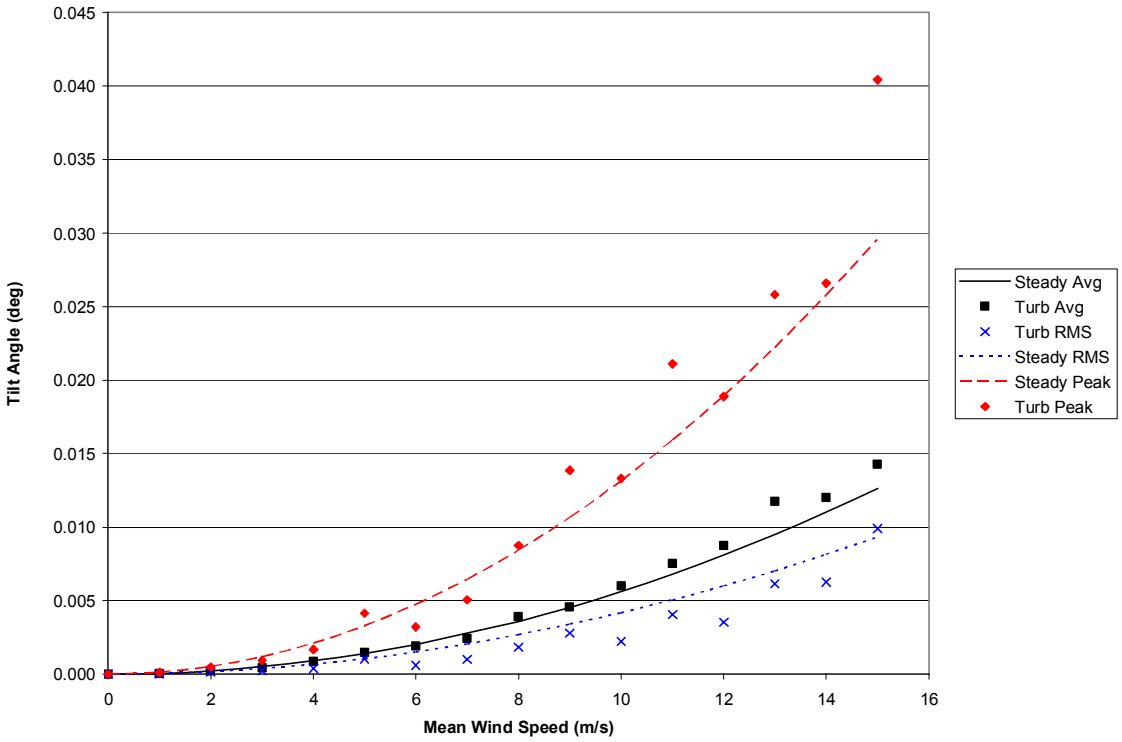

Figure 6.8c - Platform Tilt Angle vs Turbulent Mean Wind Speed

Under turbulent conditions particularly at velocities greater than 10 m/s, the most obvious effect is an increase in the average and peak performance metrics. This can be reasoned by considering the non-linear relationship between mean wind speed and the performance metrics (as shown in Figures 6.8 a, b, c). Let us assume that over a long enough time, the turbulent model gusts the wind, in a random manner, above and below the mean wind speed by an equal amount. When the turbulence model gusts the wind above its mean value, the error is affected (increased) more than it is affected when the turbulence gusts the wind below its mean value. Hence, we see that when turbulence is applied the errors increase and the performance of the system is very slightly degraded. However, even under these turbulent conditions the original Arecibo model proves to be a well performing and stable system with very small positional and rotational errors.

6.8 Upgraded Arecibo Configuration

One of the advantages of having developed a model of the original Arecibo configuration is that we may evaluate the effect of the some of the recent design changes [2]. After two big upgrades, the "upgraded" Arecibo configuration is very different from the "original" in terms of the cable system layout, the mass of the platform, and the receiver system. In this section we would like to compare the "original" Arecibo model as per Table 6.1 with the "upgraded" Arecibo model. Again, we must be clear on exactly what features of the upgraded system are being modeled. Table 6.3 gives the details of the "upgraded" Arecibo configuration and how it differs from the actual Arecibo construction after the two major upgrades.

	Actual Construction of the Upgraded Arecibo	**Model of the Upgraded Arecibo**	**Model of the Original Arecibo**
platform mass	815 000 kg	815 000 kg	550 000 kg
receiver drag	Gregorian System	Gregorian treated as a sphere	Line feed neglected
Mainstay Cables	4 cables per tower d = 3"	4 cables per tower d = 3"	4 cables per tower d = 3"
Backstay Cables	5 cables per tower d = 3.25"	5 cables per tower d = 3.25"	5 cables per tower d = 3.25"
Main Auxiliary Cables	2 cables per tower d = 3.25" Attached 2/3 of the way along the sides of the triangular truss	2 cables per tower d = 3.25" Added to the effective area of the mainstay cables. Attachment points not considered	N/A
Backstay Auxiliary Cables	2 cables per tower d = 3.625"	2 cables per tower d = 3.625"	N/A
Tie Down Cables	6 cables total d = 1.5" Two cables run vertically from each corner of the platform. Active Control: Jacks which can exert up to 60 tons of vertical force. [2]	N/A	N/A

Table 6.3 - The Upgraded Arecibo Configuration

In order to model the recent design changes, the mass of the platform was increased from 550 tons to 815 tons. The new mass moment of inertia of the platform was recalculated using the CAD software:

Mass	Ix	Iy	Iz
kg	kgm^2	kgm^2	kgm^2
550000	1.0316E+08	1.0316E+08	1.9866E+08
815000	1.5277E+08	1.5277E+08	2.9420E+07

Table 6.4 -Upgraded Platform Mass Moment of Inertias

The new effective tower stiffness (with the new auxiliary backstay cables) was found using the method outlined in Section 4.3 to be:

$$k_{eff} = 1.977 \times 10^7 \ N/m \tag{6.11}$$

The new auxiliary mainstay cables were added to the overall effective area of the existing mainstay cables. Important to note here are that the attachment points and any added rotational stability achieved by the auxiliary mainstay cables were not taken into account.

$$A_{eff} = 0.0289 \ \text{m}^2 \tag{6.12}$$

Finally the drag of the Gregorian receiver (as outlined in Section 5.5.5) was added to the overall drag of the platform and treated as acting through the platform's centre of mass. With the changes in place, we let the new upgraded configuration come to a new equilibrium and we compare the average performance metrics of the two configurations over a range of wind speeds. Note that the equilibrium heights of the original and upgraded configurations (even with the large mass and cable property changed) are within 0.6 m of each other. This was reassuring, since the number and sizes of the auxiliary cables added during the upgrade had the purpose of keeping the platform exactly where it always had been, while using the three existing towers.

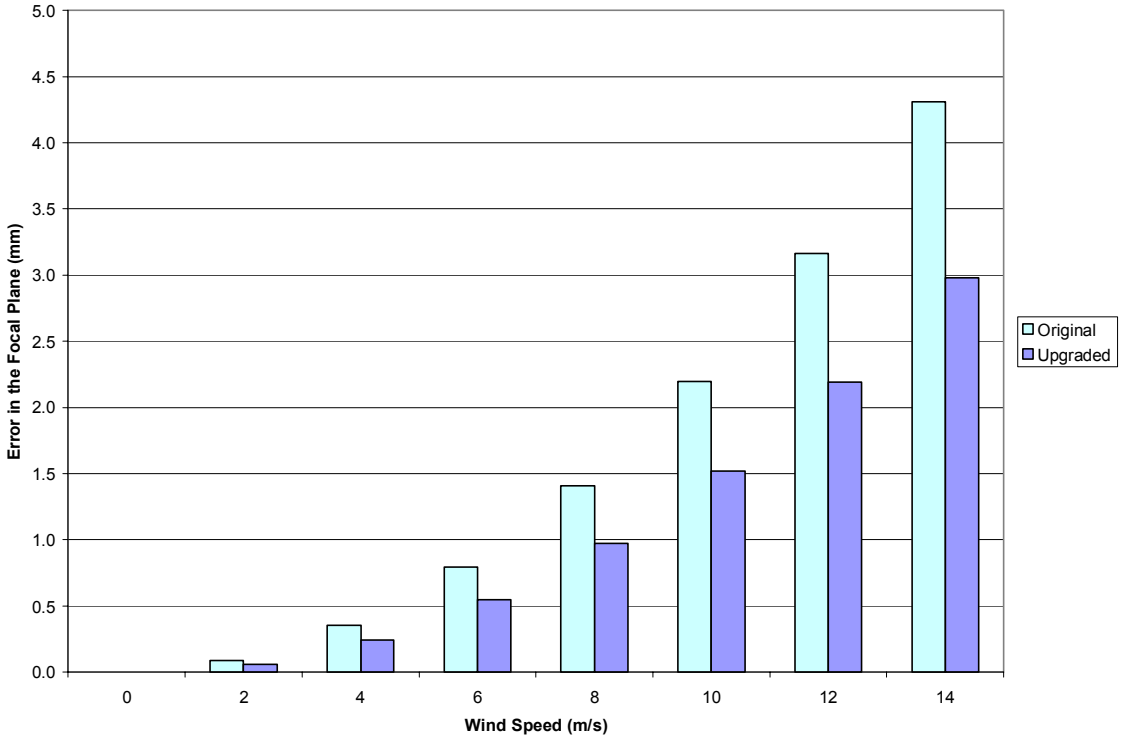

Figure 6.9 - Average Error in the Focal Plane vs Wind Speed

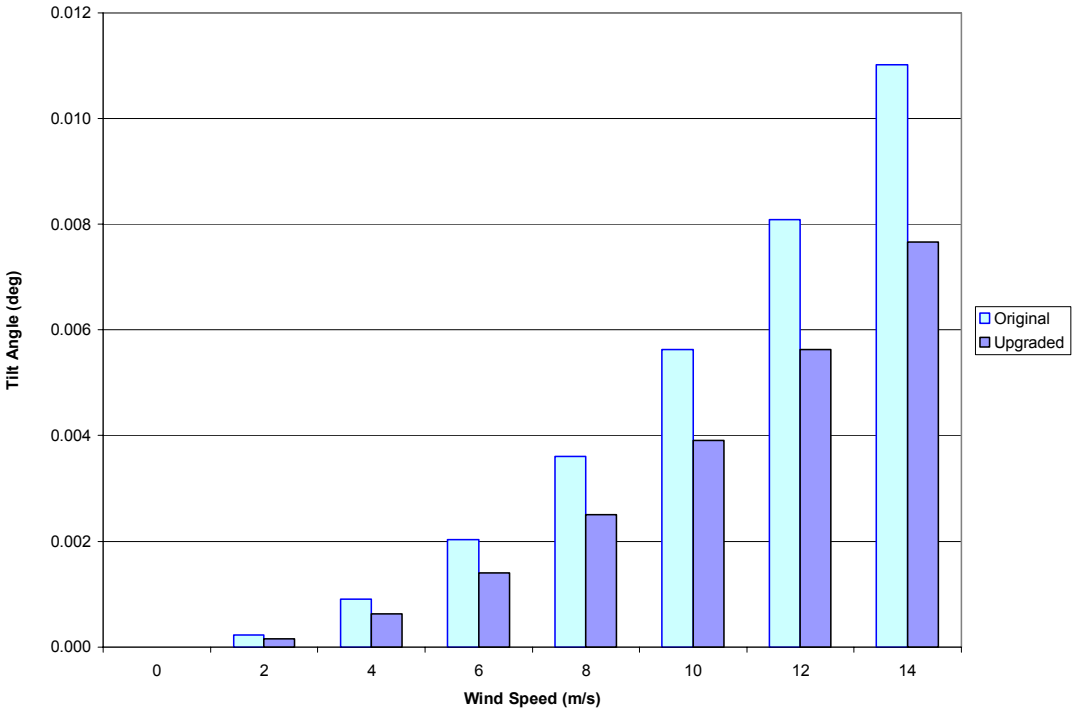

Figure 6.10 - Average Platform Tilt Angle vs Wind Speed

The errors *out* of the focal plane in both cases proved to be insignificant (of the order of 0.01 mm) and are not shown here. The results for both the error in the focal plane and the platform tilt angle are shown to be significantly less for the upgraded model than for the original model. Thus we can conclude that the recent design changes (studied in the context of these models) were in fact beneficial to the system's performance.

6.9 Selected Cases

Before moving on to the sensitivity analysis in the next chapter, it is of interest to study selected cases in more detail. In fact, two cases based on the original Arecibo model will be displayed here to better our understanding of the system's behavior, if not for the purposes of demonstrating the output capabilities of the Arecibo model. The first case (case A) is for a wind speed of 10 m/s, wind direction of 60°, and with no turbulence effects. The second case (case B) is for a wind speed of 10 m/s, wind direction of 0°, and with the turbulence active. The following output demonstrates the system's behavior over a 70 second period. Depending on the specific information required; the Arecibo model is capable of presenting a variety of data. For Case A, we see how the performance metrics and platform position and rotation each vary with time under the constant wind speed.

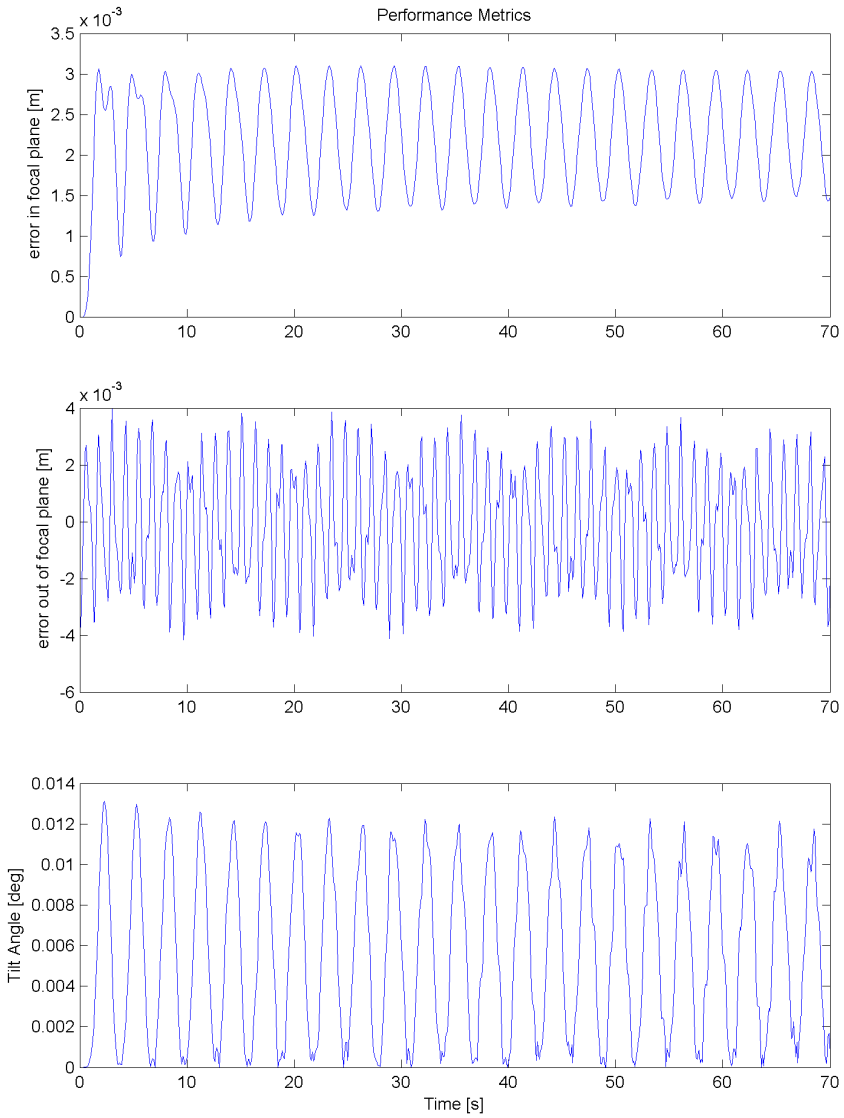

Figure 6.11 - Case A Performance Metrics

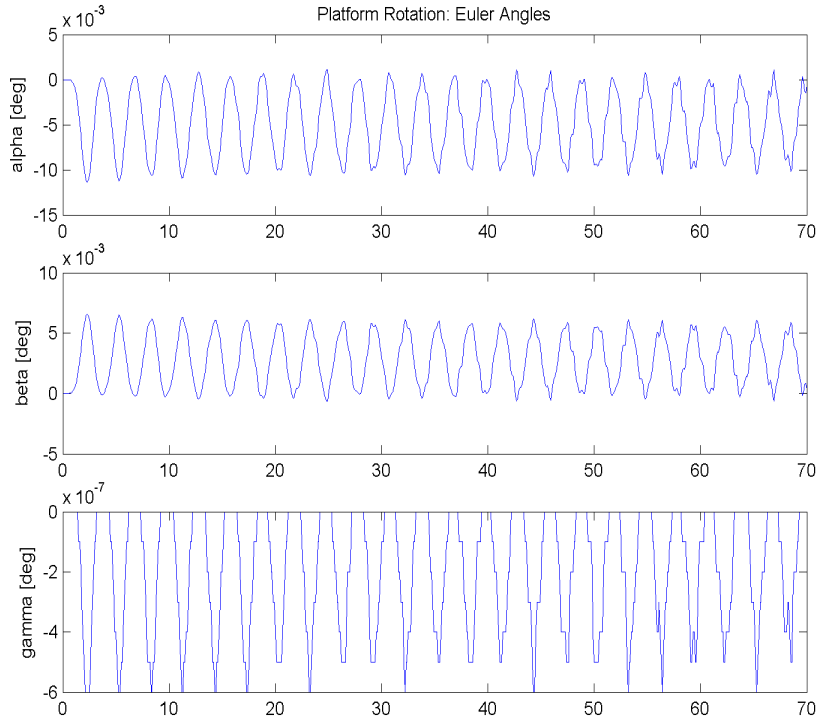

Figure 6.12 - Case A Platform Rotation

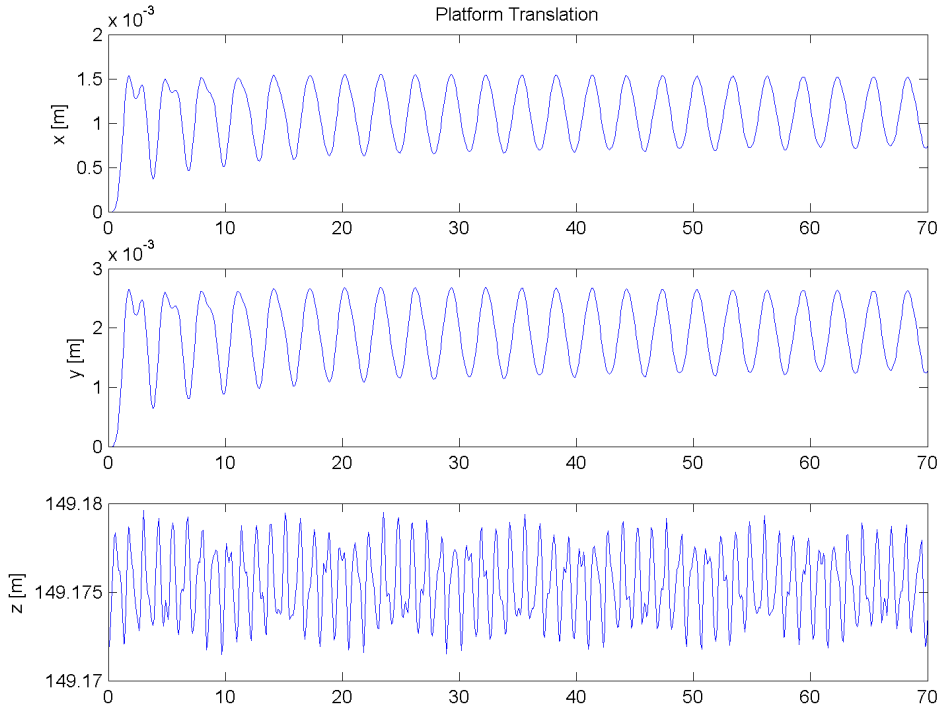

Figure 6.13 - Case A Platform Translation

In Figure 6.12, the y-axis angles alpha, beta, and gamma, refer to the Z-Y-X Euler angles of ϕ, θ, Ψ respectively. Notice that the wind direction of 60° has caused the platform to be displaced by a positive x and positive y component. The initial transient of the wind increasing to full speed in the first second may be seen (especially for the error in the focal plane). The following output is for Case B: Wind speed 10 m/s, wind direction 0°, with turbulence.

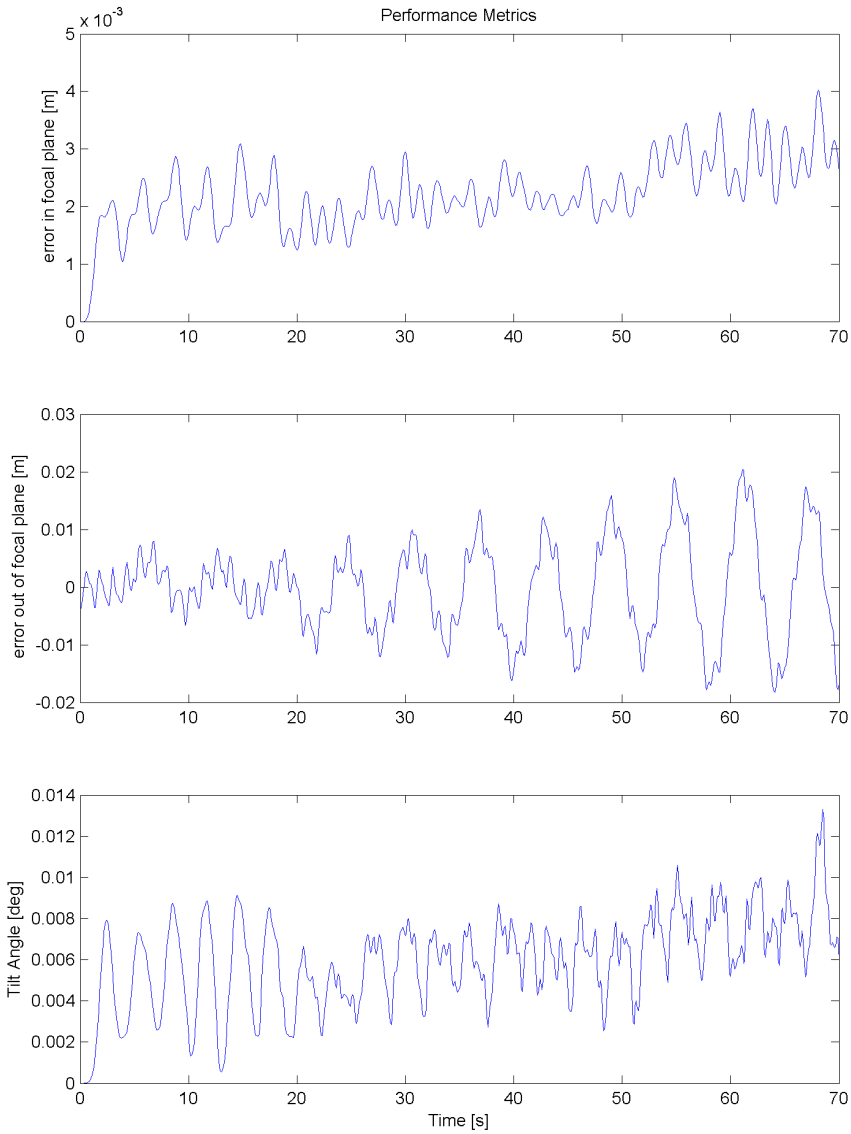

Figure 6.14 - Case B Performance Metrics

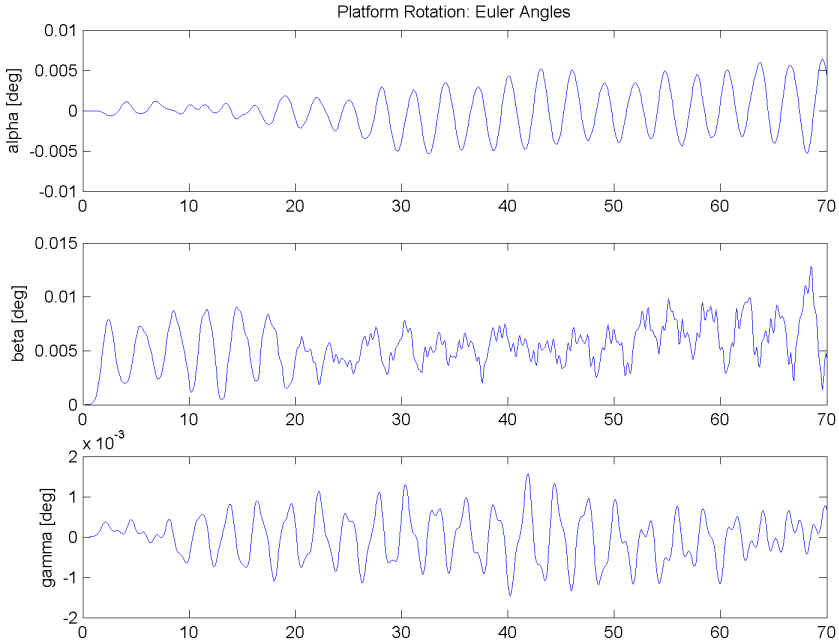

Figure 6.15 - Case B Platform Rotation

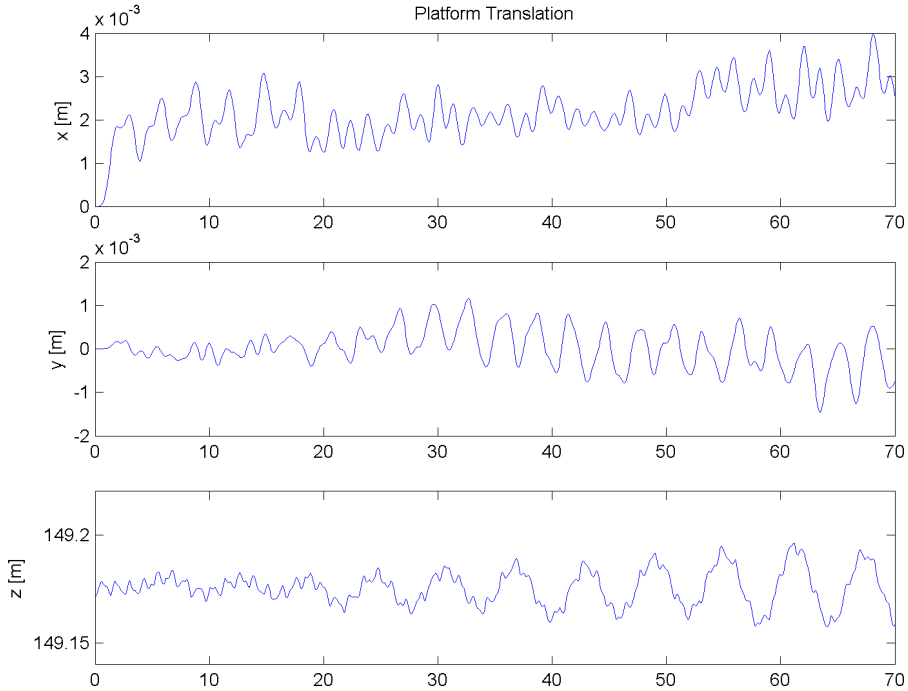

Figure 6.16 - Case B Platform Translation

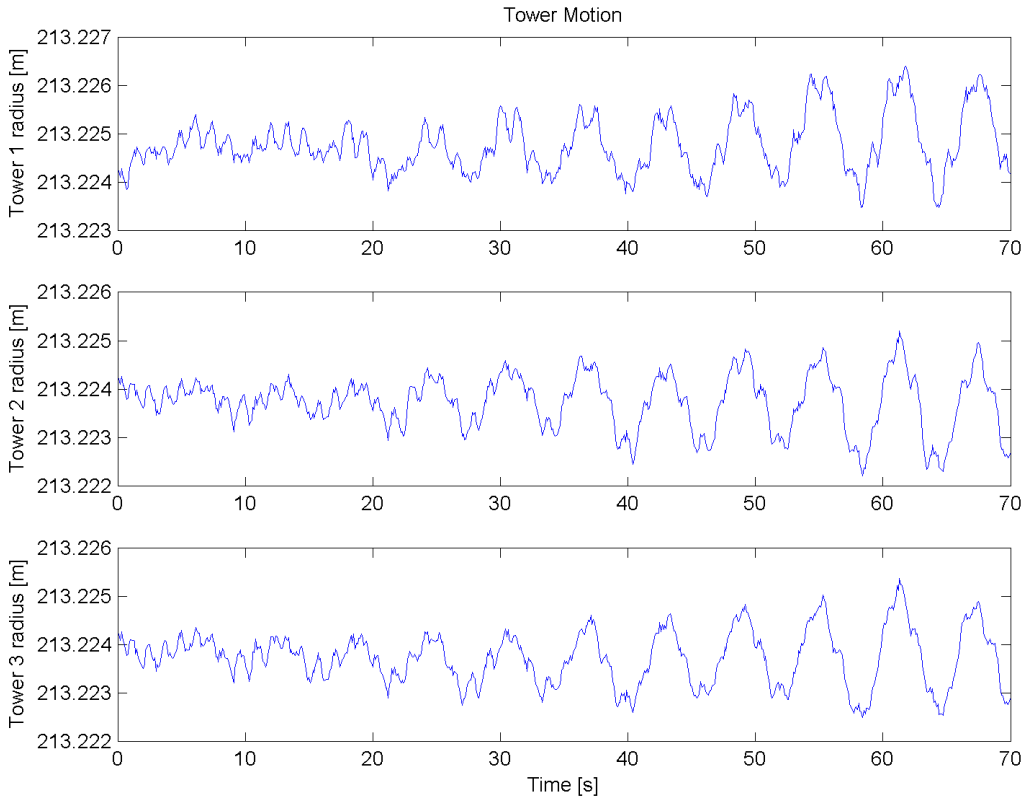

Figure 6.17 - Case B: Tower-Top Motion

For Case B, we have also included the tower-top motion, represented by the radius, from the inertial Z_i-axis, of the tower-tops in their horizontal plane of motion. Note that in Case B, the random effects of turbulence are present and observed. However the system's motion, even under turbulent conditions, is still on the order of millimeters. In the sensitivity analysis of the next chapter we will see figures that give the average, root-mean-square, and peak motion for a variety of different system configurations.

Chapter 7 Sensitivity Analysis

Often one is interested in knowing which physical parameters of a given system, if changed or redesigned, could improve the system's performance. In our sensitivity analysis, the following six parameters are varied individually while keeping all else constant:

(i) Number of Mainstay Cables
(ii) Tower Radius (Cable Length)
(iii) Effective Tower Stiffness (Number of Backstay Cables)
(iv) Mass of the Platform
(v) Cable-Platform Attachment Points
(vi) Mainstay Cable Properties (Plasma Rope)

It should be clearly noted that the following sensitivity analysis has been performed on the original Arecibo model as described in Table 6.1. Also, each test case of this sensitivity analysis presents a new physical configuration. Therefore, for each case, the system must be allowed to come to a new equilibrium condition before applying the given winds (see Section 6.6).

7.1 Test Matrix

The following Table 7.1 presents the test matrix employed in our sensitivity analysis, with the highlighted values referring to the nominal or original Arecibo model values.

Test #	Configuration	Configuration	Speed	Direction	Turbulence
			m/s	deg	
46	Effective Mainstay Cable Area - incremented by the number of mainstay cables per tower	No. of Cables = 3	10	0	No
47		No. of Cables = 4	10	0	No
48		No. of Cables = 5	10	0	No
49		No. of Cables = 6	10	0	No
50		No. of Cables = 7	10	0	No
51	Tower Radius - increases cable length	rad = 150 m	10	0	No
52		rad = 180 m	10	0	No
53		rad = 213 m	10	0	No
54		rad = 240 m	10	0	No
55		rad = 270 m	10	0	No
56	Effective Tower Stiffness - Incremented by the number of backstay cables per tower	No. of Cables = 0	10	0	No
57		No. of Cables = 1	10	0	No
58		No. of Cables = 3	10	0	No
59		No. of Cables = 5	10	0	No
60		No. of Cables = 7	10	0	No
61		No. of Cables = 9	10	0	No
62		No. of Cables = 11	10	0	No
63		k_{eff} = infinity (No Tower Motion)	10	0	No
64	Platform Mass	m_p = 400 tons	10	0	No
65		m_p = 550 tons	10	0	No
66		m_p = 700 tons	10	0	No
67		m_p = 850 tons	10	0	No
68		m_p = 1000 tons	10	0	No
69	Cable-Platform Attachment Points	rad_p = 20 m	10	0	No
70		rad_p = 30 m	10	0	No
71		rad_p = 38 m	10	0	No
72		rad_p = 50 m	10	0	No
73	Cable Properties: Plasma Rope	dc = (six 2" cables)/tower ρ = 840 kg/m^3 E = 37.4e9 N/m^2	2	0	No
74			4	0	No
75			6	0	No
76			8	0	No
77			10	0	No
78			12	0	No
79			14	0	No

Table 7.1 - Test Matrix for the Sensitivity Analysis

7.2 Number of Mainstay Cables

As per the test matrix, the number of mainstay cables has been incremented from 3 to 7 cables per tower in increments of 1. This was done by increasing the effective area of the mainstay cables using Equation 3.1. The following Table 7.2 presents the effective mainstay cable areas used for each test case.

No. of Mainstay Cables	Effective Area
	[m^2]
3	0.014
4	0.018
5	0.023
6	0.027
7	0.032

Table 7.2 - Mainstay Cable Effective Areas

Figure 7.1 shows that as we increase the number of mainstay cables, the effective stiffness of the cables increases such that the equilibrium height of the platform increases.

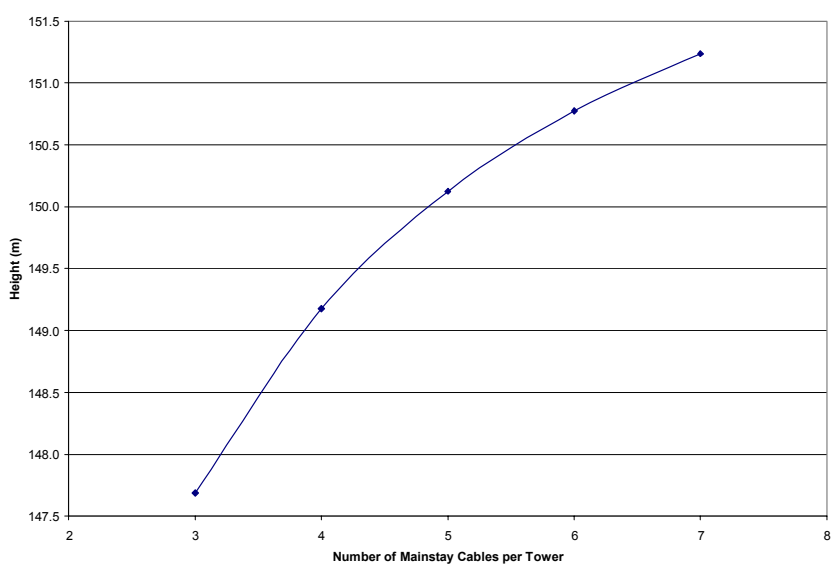

Figure 7.1 - Equilibrium Platform Height vs No. of Mainstay Cables

Figure 7.2 shows that the as the number of mainstay cables are increased, the equilibrium tensions *per cable* is decreased.

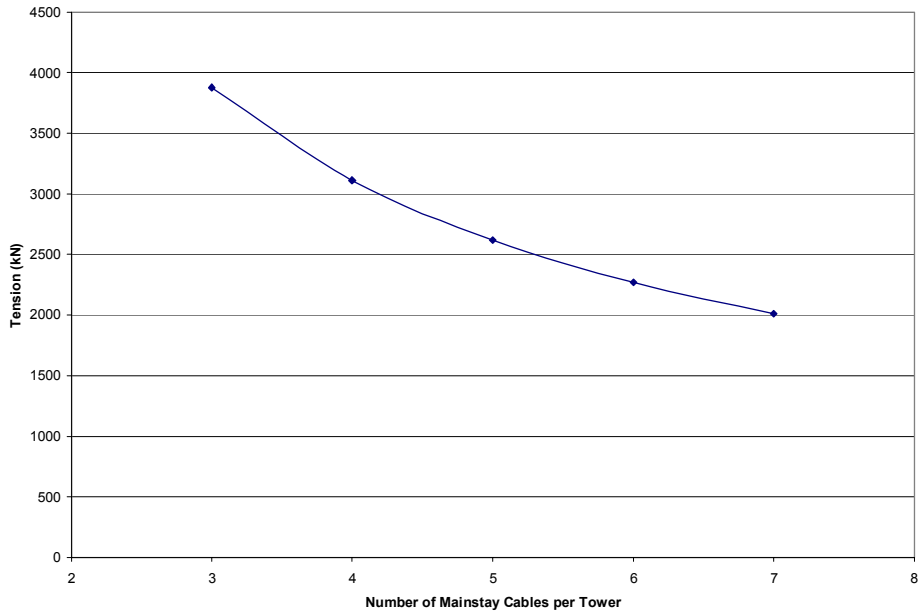

Figure 7.2 – Equilibrium Tensions per Cable vs Number of Cables

In terms of the performance metrics when the system was subjected to a wind of 10 m/s it was found that increasing the number of mainstay cables improves the system's performance by decreasing the error in the focal plane. By increasing the number of cables from 3 to 7 the $\Delta Error_{in} = -0.8\ mm$. There was no significant change to the error out of the focal plane or to the tilt angle.

7.3 Tower Radius

Changing the radius of the towers (taken from the centre of the collector dish) is essentially one way of also changing the total lengths of the cables. It was found that when increasing the tower radius, the only metric affected was the error in the focal plane. Figure 7.3 shows that for a tower radius increase from 150 m (right at the edge of the collector dish) to 270 m, the error in the focal plane is increased by approximately 0.5 mm. Each test case is for a constant mean wind of 10 m/s observed over 70 seconds. Of course, this could be looked at in the reverse manner, such that decreasing the tower radius would serve to better the performance of the system.

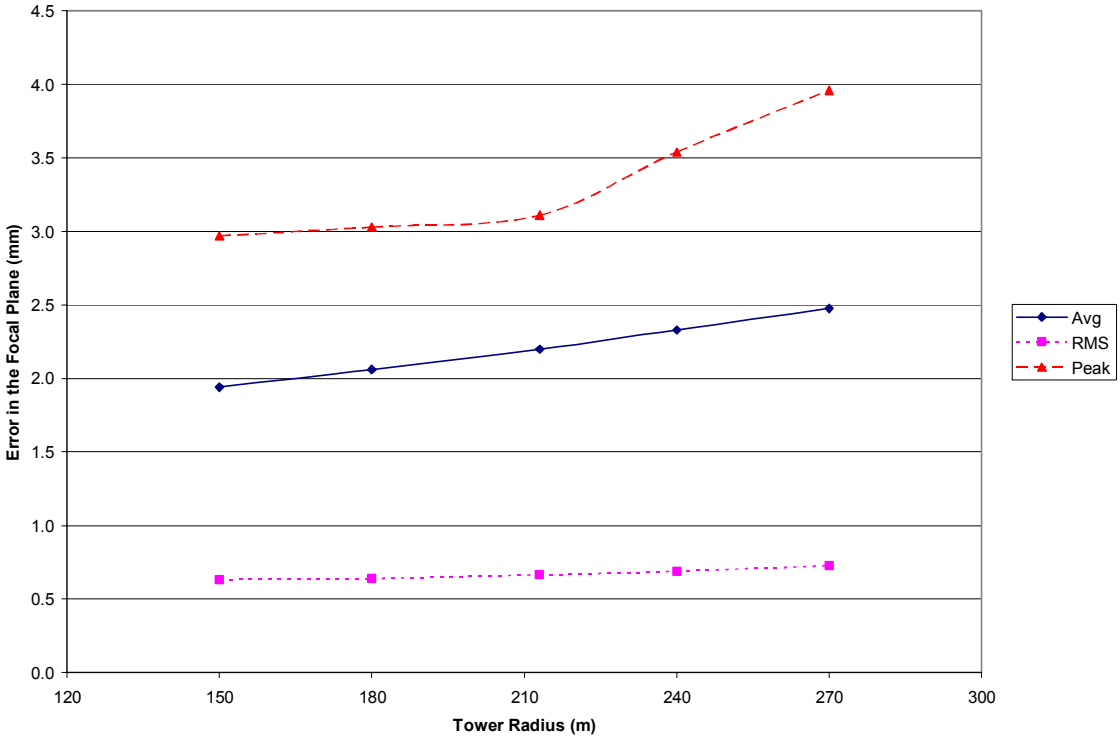

Figure 7.3 - Error in the Focal Plane vs Tower Radius

7.4 Effective Tower Stiffness

In order to evaluate the effect of the tower-top deflection on the performance of the system, we vary the effective tower stiffness by incrementing the number of backstay cables and recalculating the effective tower stiffness for each case, as per Section 4.3. Each test case is for a constant mean wind of 10 m/s at 0° observed over 70 seconds. The following Table 7.3 presents the average effective tower stiffnesses calculated for each increment of backstay cable. For the extreme case of no tower-top motion, we let the effective stiffness go to infinity. Specifically, we use the value $k_{eff} = 1.0 \times 10^{20} N/m$ as the infinite condition (any further increase has no effect to the system dynamics).

No. of Backstay Cables	Effective Area [m^2]	Average Effective Stiffness [N/m]
0	0.0000	3.458E+05
1	0.0054	2.946E+06
3	0.0161	8.146E+06
5	0.0268	1.335E+03
7	0.0375	1.855E+07
9	0.0482	2.375E+07
Infinite	Infinite	1.000E+20

Table 7.3 Average Tower Effective Stiffness

It is observed that the effective tower stiffness plays a very important role in the performance of the system. Especially concerning the error in the focal plane and the tilt angle metrics. The following figures present the results while indicating the ideal case of $k_{eff} = \infty$ and zero tower-top deflection. As the effective tower stiffness is increased the error and tilt angle drop rapidly from 0 to 3 backstay cables. The error then begins to asymptote toward the $k_{eff} = \infty$ limit.

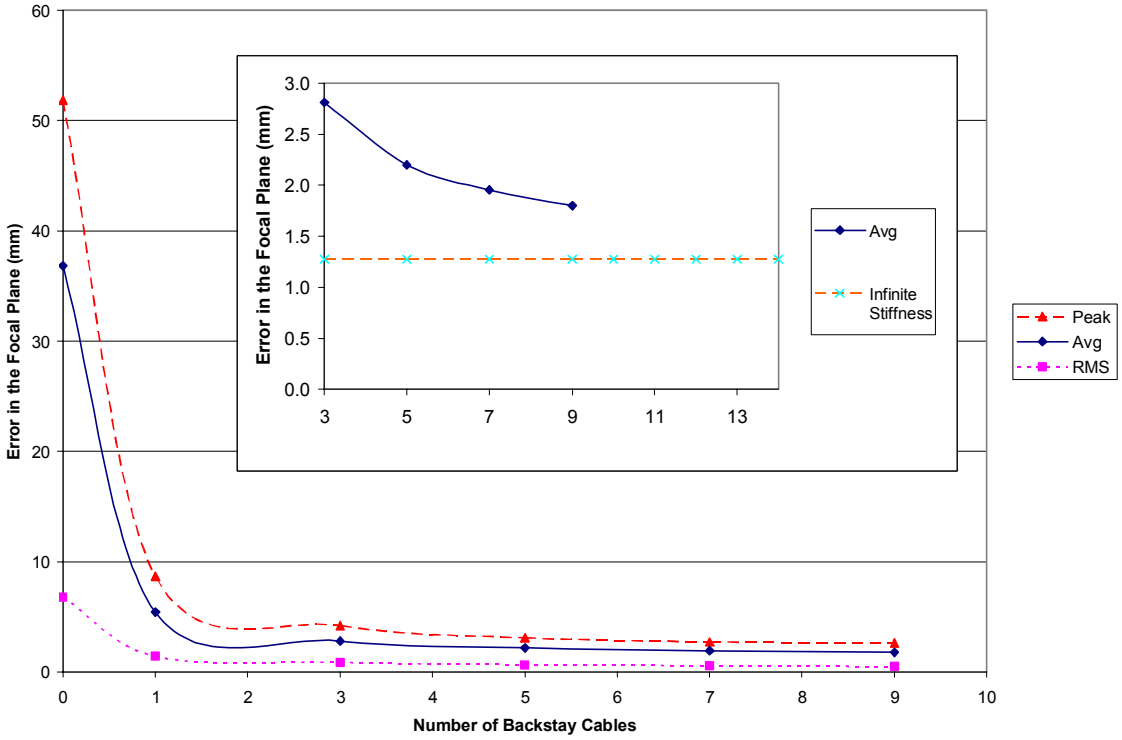

Figure 7.4a - Error in the Focal Plane vs Number of Backstay Cables

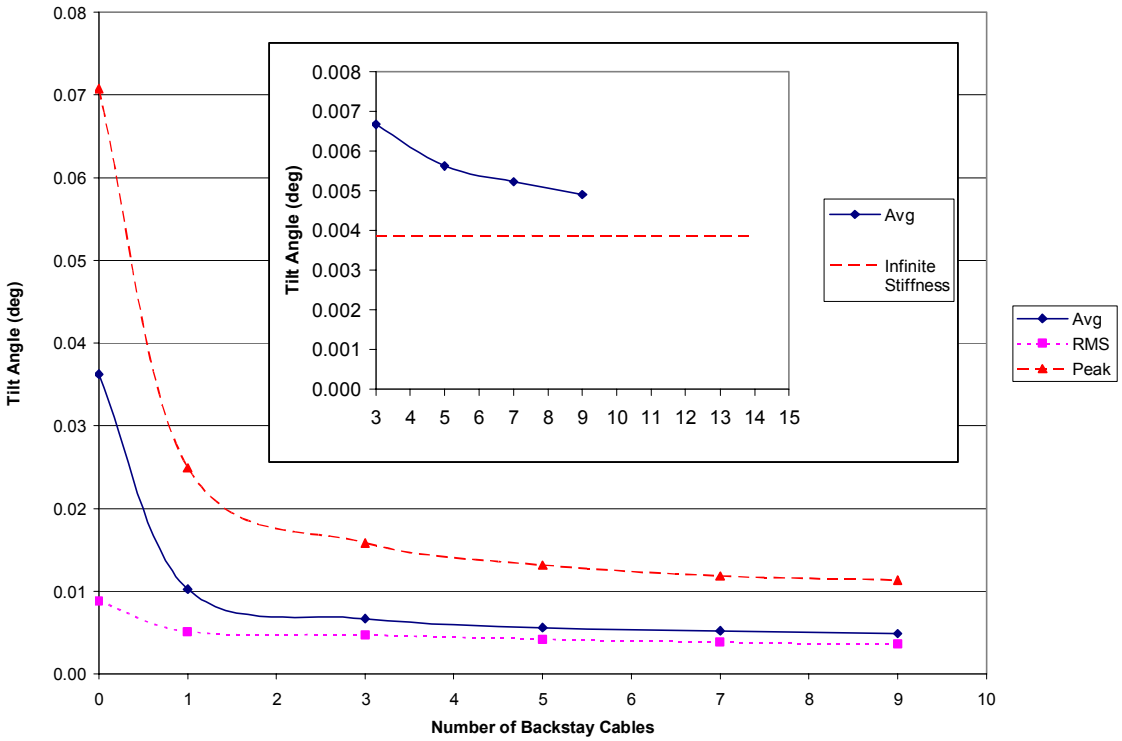

Figure 7.4b -Platform Tilt Angle vs Number of Backstay Cables

Also of interest is Figure 7.4c which shows the tower-top deflection as a function of the number of backstay cables for a wind speed of 10 m/s at 0°. Notice that the tower-top deflection approaches zero as k_{eff} approaches infinity.

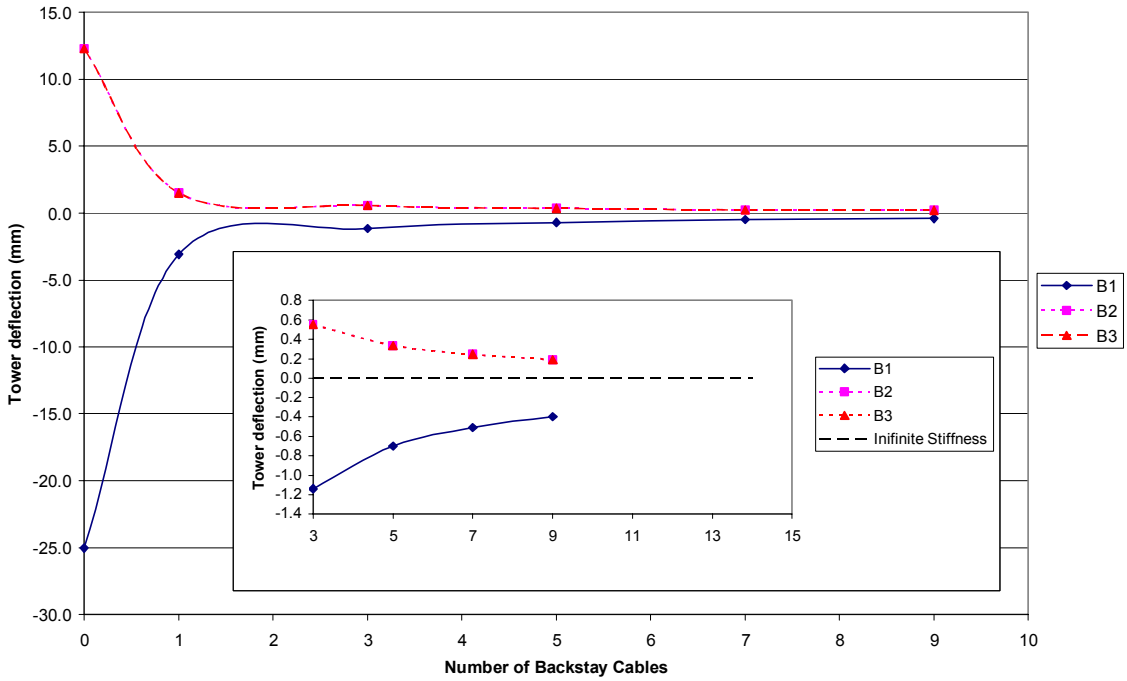

Figure 7.4c - Average Tower Deflection vs Number of Backstay Cables

7.5 Platform Mass

One of the most astounding features of the Arecibo Radio Telescope is the mass of the suspended platform structure. At 550 tons in the original Arecibo configuration it was later increased to 815 tons in 1997 [2]. With the use of our original Arecibo model we will vary the platform mass in order to evaluate what effects it may have on the system's performance. Recall that in Section 5.3 the platform's mass moment of inertia (used in the rotational equations of motion) was found using CAD software and a uniform density triangular shaped section. In order to perform this sensitivity analysis,

not only must we change the platform mass, but we must also recalculate the mass moments of inertia for each case. Table 7.4 gives the mass moment of inertia for the various platform masses. Recall that the cross terms are in fact zero due to the symmetry of our modeled platform.

Mass	Ix	Iy	Iz
kg	kgm^2	kgm^2	kgm^2
550000	1.0316E+08	1.0316E+08	1.9866E+08
815000	1.5277E+08	1.5277E+08	2.9420E+07
400000	7.5028E+07	7.5028E+07	1.4448E+08
700000	1.3130E+08	1.3130E+08	2.5284E+08
850000	1.5925E+08	1.5925E+08	3.0703E+07
1000000	1.8757E+08	1.8757E+08	3.6121E+07

Table 7.4 – Platform Mass-Moment of Inertia

Figure 7.5 shows that as the mass of the platform is increased, for the same number of cables, the equilibrium height of the platform decreases.

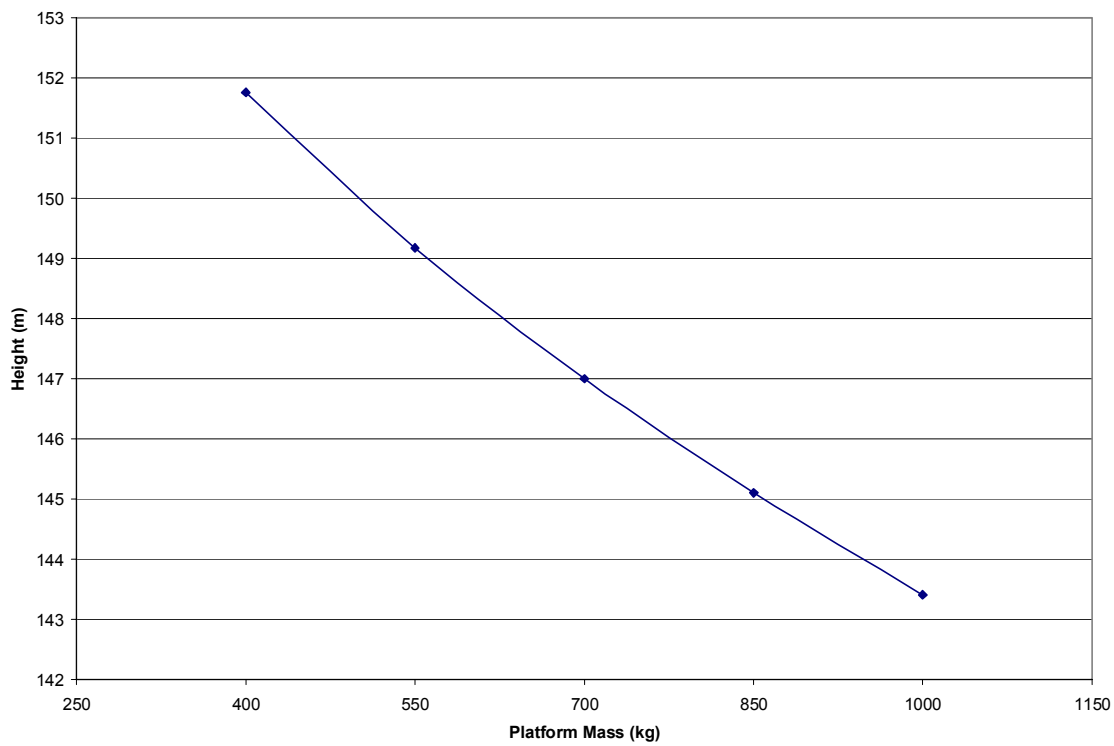

Figure 7.5 - Equilibrium Platform Height vs Platform Mass

Running the test cases for a wind speed of 10 m/s, a wind direction of 0° and no turbulence it was interesting to find that increasing the platform mass had essentially no effect on the platform's positional error. It did however reduce the platform's tilt angle error as shown in Figure 7.6, which makes sense in terms of an increasing mass-moment of inertia.

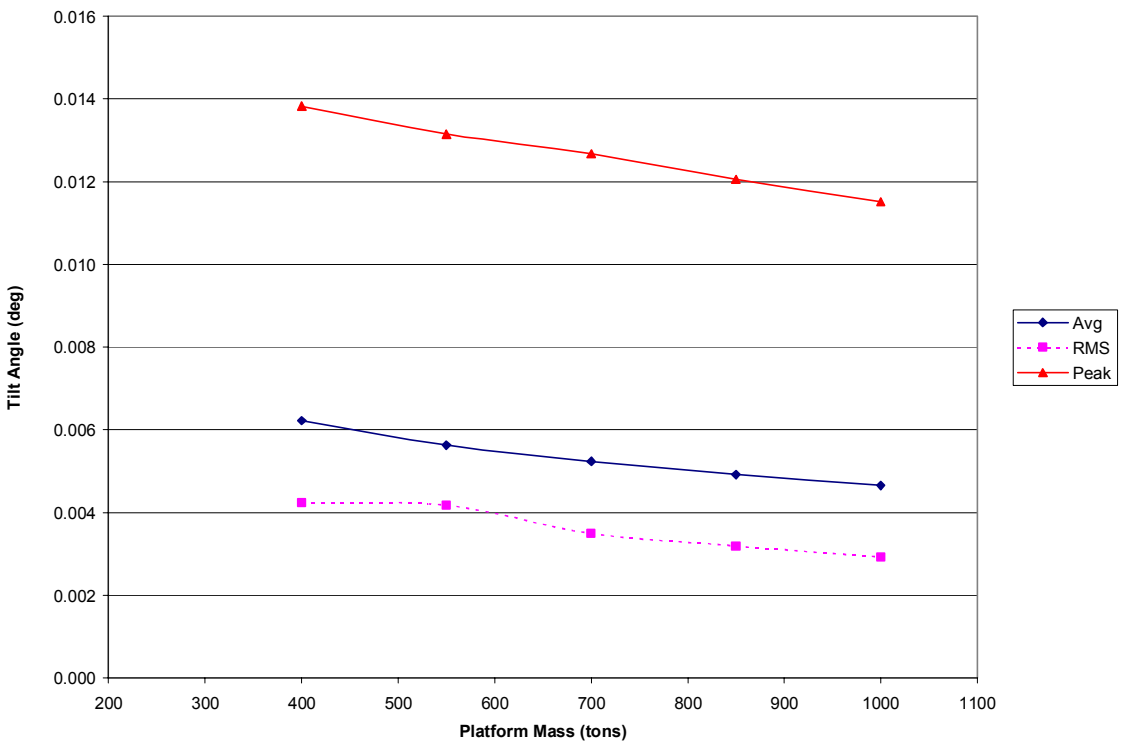

Figure 7.6 – Platform Tilt Angle vs Platform Mass

The following Table 7.5 gives the minimum cable breaking strength of the cables as found in the available AutoCAD drawings [14].

	Mainstay Cables		Backstay Cables	
	[in & kips]	[m & N]	[in & kips]	[m & N]
Total Number of Cables	12	12	5	5
Diameter of each cable	3	0.0762	3.25	0.08255
Minimum breaking strength	1044	4.6439E+06	1212	5.3912E+06

Table 7.5 – Minimum Breaking Strength of Cables

According to the original Arecibo model, the minimum breaking strength is reached at a platform mass of 1000 tons, giving a tension of approximately $4.5\times10^{6}\,N$ per cable.

7.6 Cable-Platform Attachment Points

Next we look to evaluate the effect of moving the cable-platform attachment point closer in and further out from the platform's centre of mass. The variable rad_p will be used to denote the radial distance at which the mainstay cables are attached to the triangular truss platform (see Figure 7.7). Note that here we are only changing the attachment point and not the dimension of the platform itself (as used in the drag model and mass moment of inertia calculations). Changing rad_p will have a direct effect on the moments acting on the platform, and our goal here is to find out how important this parameter is to the performance of the Arecibo Radio Telescope.

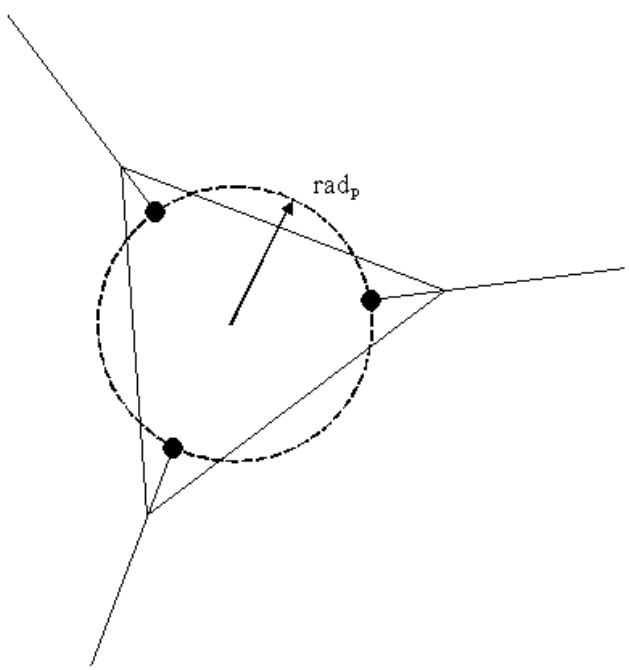

Figure 7.7 – Cable-Platform Attachment Points

Setting up the test runs as per the test matrix in Table 7.1, we obtained some interesting results. Figure 7.8 shows there to be a relatively significant increase to the error in the focal plane of the platform with increasing attachment point radius (rad_p), which is obviously not good. However, Figure 7.9 shows there to be a decrease in the average tilt angle with increasing attachment point radius. Thus, the optimal attachment point distance would require some sort of compromise between the performance metrics. Also, there was no significant change to the error out of the focal plane with increasing attachment point radius.

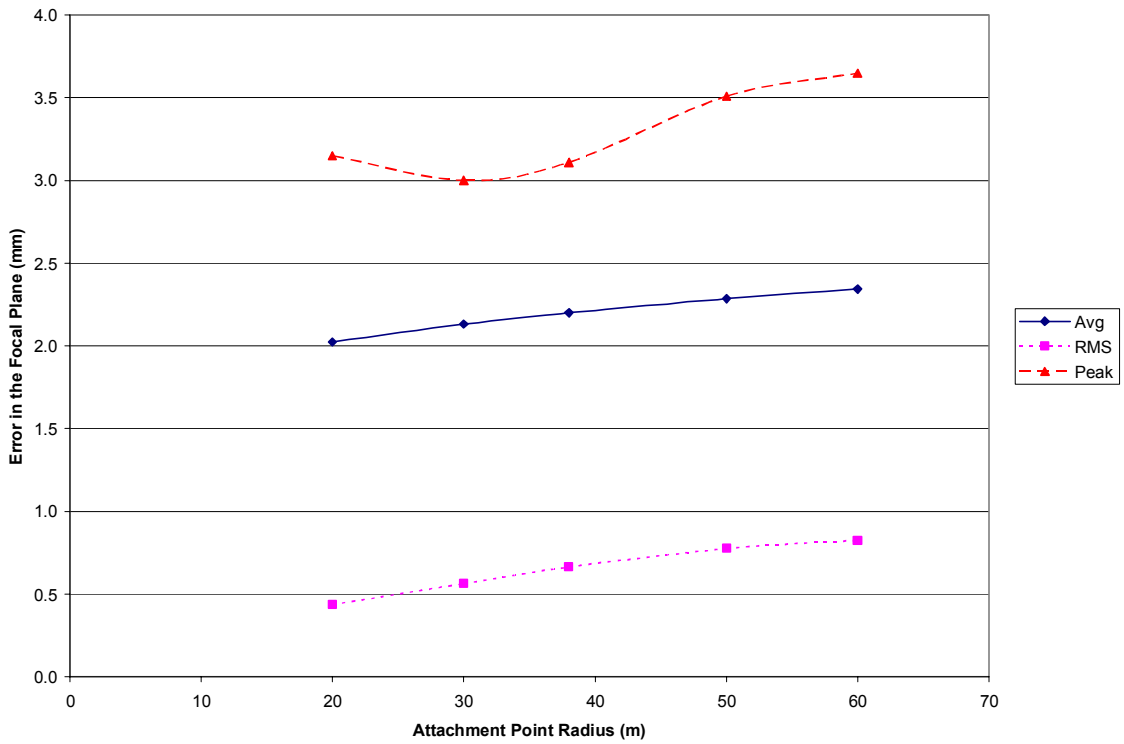

Figure 7.8 - Error in the Focal Plane vs Platform-Cable Attachment Radius

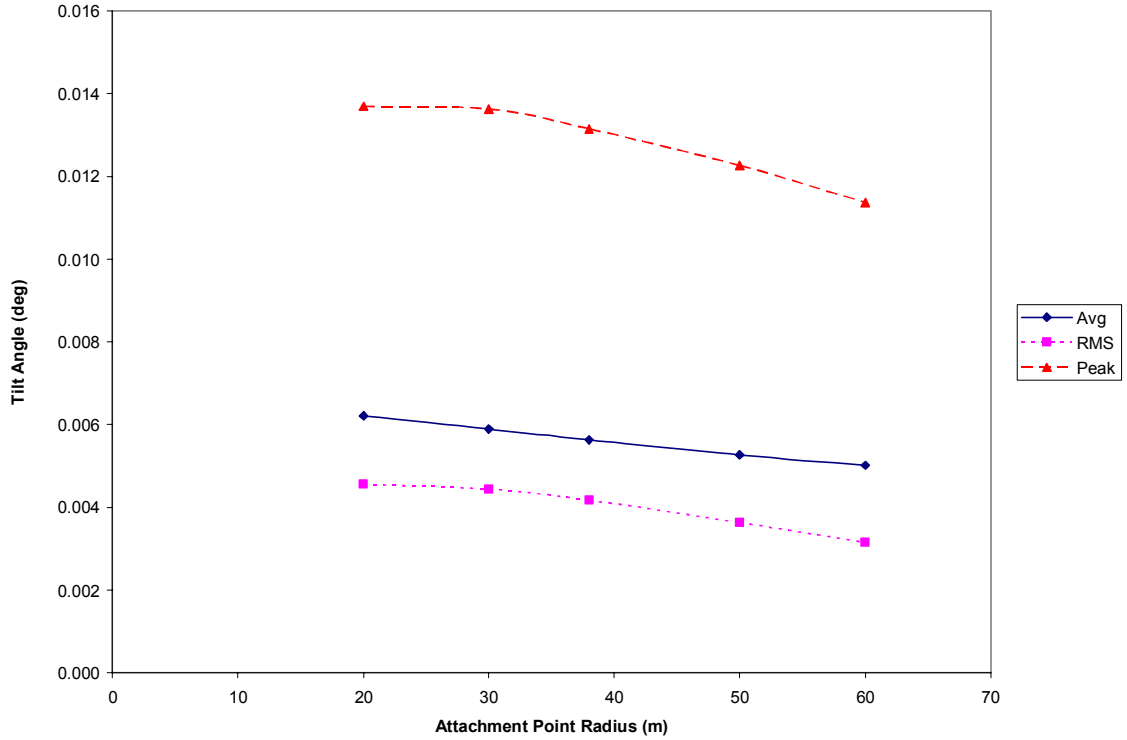

Figure 7.9 - Platform Tilt Angle vs Platform-Cable Attachment Radius

7.7 Mainstay Cable Properties: Plasma Rope

The final parameter of our sensitivity analysis satisfied our curiosity regarding the use of a completely different type of mainstay cable. We chose to replace the braided steel cables with the so-called "plasma rope" that is being used for the LAR system. The main advantage of plasma rope is that it is the "world's strongest rope for its weight" [26]. Presumably, a light weight material has no particular advantage in the Arecibo system in improving its performance, so it was interesting to investigate the feasibility of using Plasma rope for the Arecibo mainstay cables. Table 7.6 gives the cable properties used for plasma rope in this analysis [26].

Plasma Rope			
Property	**Symbol**	**Value**	**Units**
Density	ρ	840	kg/m^3
Elastic Modulus	E	37.4	GPa
Damping Ratio	ζ	0.015	

Table 7.6 – Plasma Rope Properties

The choice of the effective area to be used for the plasma rope was next considered. It was decided to use an effective area of the plasma rope that would give the plasma cables the equivalent stiffness as the braided steel mainstay cables:

$$(EA_{eff})_{steel} = (EA_{eff})_{plasma} \tag{7.1}$$

$$\begin{aligned} A_{eff\ plasma} &= \frac{(EA_{eff})_{seeel}}{E_{plasma}} \\ &= \frac{(1.0\times10^{11})(4.56\times10^{-3})}{37.4\times10^{9}} \\ &= 0.01219\ m^2 \end{aligned}$$

This effective area may be realized by employing six, 2 inch tethers $(A_{eff} = 0.01216m^2)$ per tower or even three, 3 inch tethers $(A_{eff} = 0.01368m^2)$ per tower. Finally to ensure that the plasma cables have enough strength to carry the load we perform a rough strength calculation:

$$T_{total} = \frac{m_p g}{\sin\theta} = \frac{550000(9.81)}{\sin(12^o)} = 25.950kN \tag{7.2}$$

$$T_{per\,cable} = \frac{T_{total}}{3\times6} = 1.441kN$$

Where m_p is the mass of the platform, g is the gravitational constant, and θ is the approximate angle of the cables at the cable-platform attachment. The tension per plasma cable is found to be approximately 1.441 kN which is under (but close to) the minimum tensile strength of 1.579 kN for a 2 inch stand [26].

Figure 7.10a shows that average error in the focal plane over a range of wind speeds is significantly higher when using plasma rope.

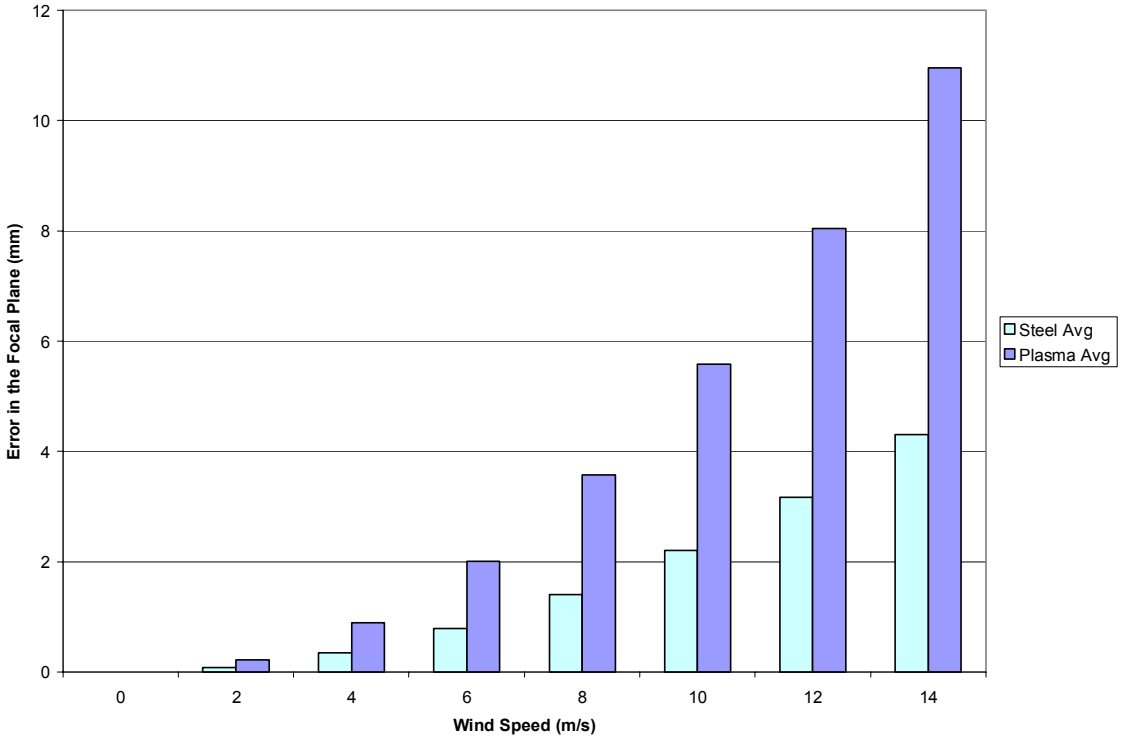

Figure *7.10 a – Average Error in the Focal Plane vs. Wind Speed for Plasma Rope*

The same is true for the remaining performance metrics as is shown in the following figures. Therefore, we can conclude that using plasma rope for the Arecibo Radio Telescope degrades the system's performance.

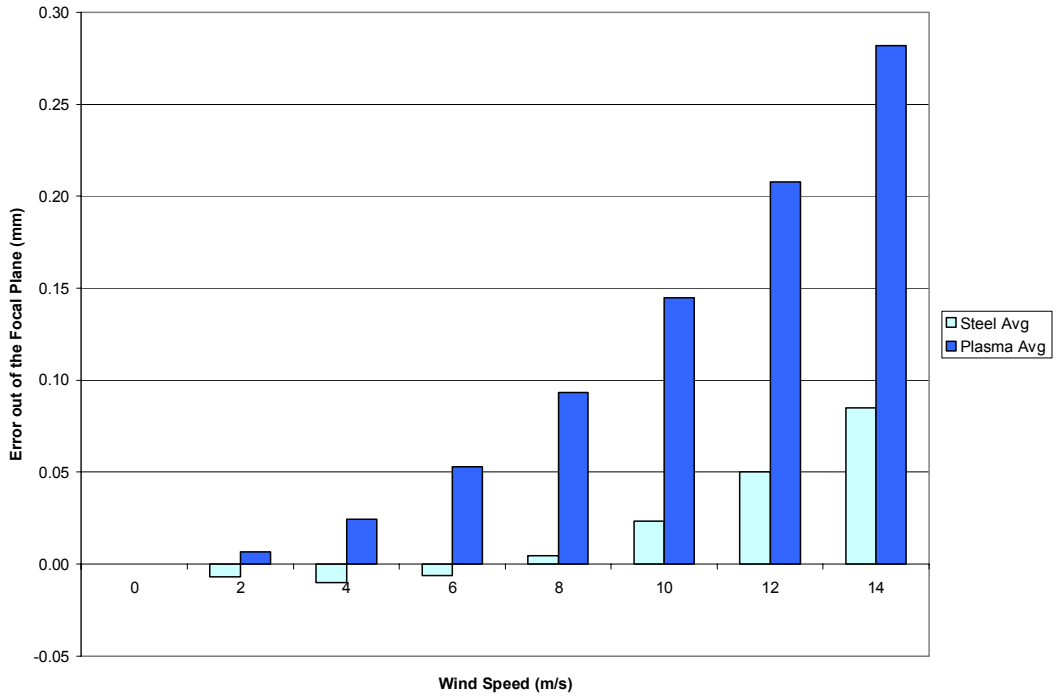

Figure 7.10b – Average Error out the Focal Plane vs. Wind Speed for Plasma Rope

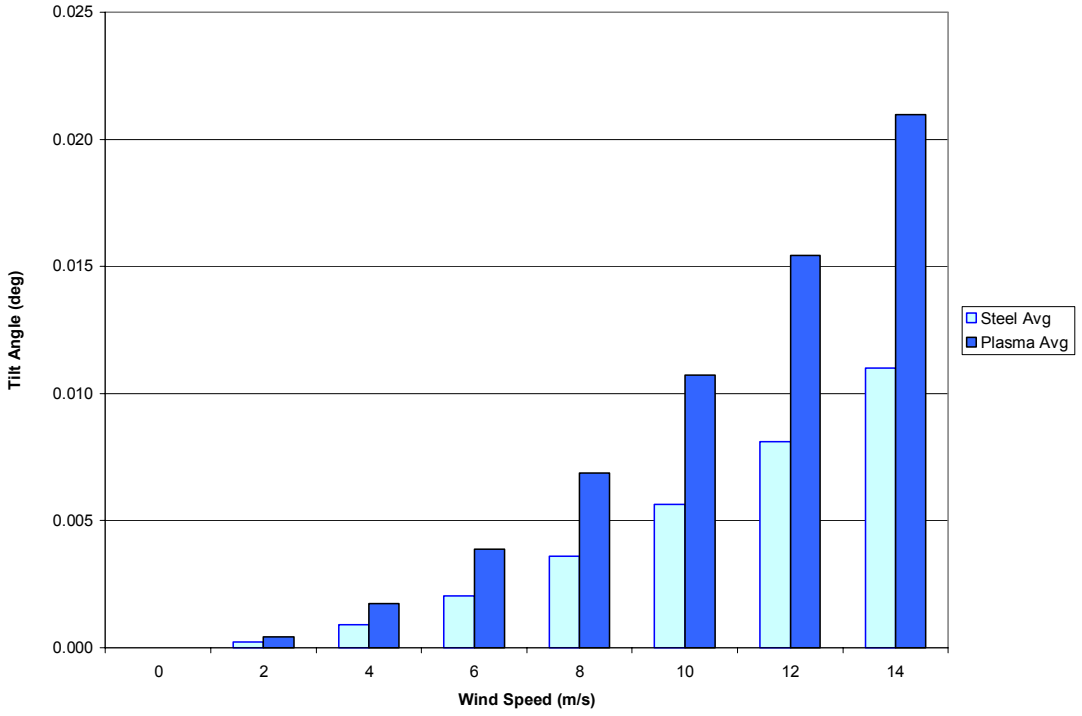

Figure 7.10c – Tilt Angle vs. Wind Speed for Plasma Rope

7.7 Summary

Having successfully completed a sensitivity analysis on the original Arecibo model, we present the Table 7.7 that qualitatively summarizes the results of the investigation. It should be kept in mind that these results are for a wind speed of 10 m/s and a wind direction of 0°, with no turbulence (except for the case of the Plasma Rope which was tested over range of wind speeds). Also note that the general trends presented in this section are for the average values of the performance metrics observed over a time of 70 seconds.

Variable	Error In FP	Error Out FP	Tilt Angle	Tension	Tower-Top Deflection
Increase No. of Main Cables	Decreases	Constant	Decreases	Tension per cable decreases	Constant
Increase Tower Radius (cable length)	Increases	Constant	Constant	Increases	Constant
Increase Platform Mass	Constant	Constant	Decreases	Increases	Constant
Increase Tower Stiffness (No.of bacstay cables)	Decreases significantly	Constant	Decreases significantly	Mainstay cable tension increases	Decreases
Increase Cable-Platform Attachment Radius	Increases	Constant	Decreases	Decreases	Constant
Using Plasma Rope	Increases	Increases	Increases	Decreases	Constant

Table 7.7 – Qualitative Summary of Sensitivity Analysis

Chapter 8 – Conclusions

8.1 Final Remarks

In summary, a basic model for the dynamics of the Arecibo Radio Telescope has been developed. The development of the model successfully stemmed from an earlier version of a dynamics model of the LAR system [6]. Upon developing the model, a successful performance evaluation and sensitivity analysis was carried out. The following is a list of the key conclusions that were drawn from the performance evaluation:

- The original Arecibo model, even at very high wind speeds, is subject to motion on the order of tens of millimeters.
- The tilt angle is also very small, even at high wind speeds: approximately 0.02° (or $3.5\times10^{-4}\,rad$) at a wind speed of 20 m/s.
- The peak tower deflection, even at the hurricane wind speed of 30 m/s, was found to be very small (6.2 mm), which is well within the permissible limit of 2 inches, or 50.8 mm [13] for the tower-top deflection.
- Wind direction has negligible effect on the performance of the system
- Turbulent wind, particularly at mean wind speeds in excess of 10 m/s, has the effect of increasing the average and peak performance metrics, thus degrading the system's performance. However the system's motion, even under turbulent conditions, is still on the order of centimeters.
- The recent design changes (studied in the context of these models) were in fact beneficial to the system's performance.

From the information gathered in the sensitivity analysis, the following final remarks address the question: What general trends or changes to the physical construction of the Arecibo Radio Telescope would *improve* the system's performance?

- Increasing the number of mainstay cables
- Decreasing the tower radius
- Increasing the effective tower stiffness (i.e. the number of backstay cables)
- Increasing the platform's mass

8.2 Recommendations for Future Work

The advantage of computer modeling is once again demonstrated in this section. Upon development of a basic model, such as the Arecibo model, there is always room for improvement and added features. The key target areas of the model which should be considered in future development are:

- Tiedown Cables: A large effort was in fact put forward in trying to implement the tie down cables (specifically the vertical tiedowns for the upgraded Arecibo configuration). Unfortunately, time was a limiting factor and it was decided that the tie downs were beyond the scope of this thesis. For this reason, the next feature that should be added to the basic Arecibo model is the tie down cables. There are two possible approaches:
    - Develop a code that introduces 3 new cables that are self-contained.
    - Set the number of cables in the existing code to 6, with different base point specifications for the mainstay and tiedown cables.

  In either case a new method for determining the unstretched length of the tiedowns must be devised. Finally, it should be noted that the vertical tiedowns of the upgraded Arecibo and the off vertical catenaries of the original Arecibo present the same challenges or problems in terms of model development. When one problem is solved, the other follows.

- Gregorian Positioning: Devise a feature, either in the dynamics model itself or offline, to take into account the different zenith and azimuth angles that the Gregorian system may take. To do this, the mass-moment of inertia of the platform may no longer be assumed as a uniform density triangular section that includes the mass of the Gregorian. Also, the drag of the Gregorian should no longer be taken at the centre of mass of the platform (this will introduce a moment force acting on the platform due to its own drag).
- Platform Drag Model: Improvements to the triangular truss platform drag model should be a goal of future development. The drag through multiple truss frame sections (i.e. more than a pair) should be researched and the platform drag coefficients should be improved.

References

1. Kutner, M.L., *Astronomy: A Physical Perspective*, Cambridge University Press, United Kingdom, 2003.

2. Goldsmith, P.F., 'The Second Arecibo Upgrade: A Reflection of How Technology Has Changed', *IEEE Potentials*, 1996, Vol. 15, No. 3, pp. 38-43.

3. Burke, B.F., Graham-Smith, F., *An Introduction to Radio Astronomy*, 2nd ed., Cambridge University Press, Great Britain, 2002.

4. Gordon, W.E., LaLonde, L.M., 'The Design and Capabilities of an Ionospheric Radar Probe', *IRE Transactions on Antennas and Propagation*, 1961, Vol. AP-9, pp.17-22.

5. LaLonde, L.M., 'The Upgraded Arecibo Observatory', *Science*, 1974, Vol. 186, pp. 213-218.

6. Nahon, M., 'Dynamics and Control of a Novel Radio Telescope Antenna', *AIAA Paper*, 99-4120.

7. Baraff, D., *Physically Based Modeling,* <http://www/pixar.com/companyinfo/research/index.html>, Accessed 2004 November.

8. Press, W.H., Flannery, B.P., Teukolsky, S.A., Vetterling, W.T., *Numerical Recipes in C: The Art of Scientific Computing*, Cambridge University Press, 1988.

9. Driscoll, A.H., *Handbook of Oceanographic Winch, Wire, and Cable Technology*, Institute of Ocean Sciences, British Columbia, 1982.

10. Inman, D.J., *Engineering Vibration*, Prentice-Hall, Inc., New Jersey, 1996.

11. Hamilton, J.M., 'Vibration-Based Techniques for Measuring the Elastic Properties of Ropes and the Added Mass of Submerged Objects', *Journal of Atmospheric and Oceanographic Technology*, 1999, Vol.17, pp.688-697.

12. Torchinsky, S., 2004 August 31, 'AutoCAD Drawing of Arecibo', [Personal Email], Accessed 2004 September.

13. Altschuler, D.R., 'The National Astronomy and Ionosphere Center's (NAIC) Arecibo Observatory in Puerto Rico', *Single-Dish Astronomy: Techniques and Applications*, ASP Conference Proc., Astronomy Society of the Pacific, San Francisco, 2002, Vol. 278, pp.1-24.

14. Torchinsky, S., 2004 June 19, 'AutoCAD Drawings of Arecibo', [Personal Email], Accessed 2004 June.

15. Baumeister, T., *Standard Handbook for Mechanical Engineers,* 7th ed., McGraw-Hill, Inc., New York, 1967.

16. Gaylord, Jr., E.H., Gaylord, C.N., *Structural Engineering Handbook*, McGraw-Hill, Inc., New York, 1968.

17. Meriam, J.L., Kraige, L.G., *Engineering Mechanics Volume 2: Dynamics*, 4th ed., John Wiley & Sons, Inc., New York, 1998.

18. Lambert, C., Nahon, M., 'Stability Analysis of a Tethered Aerostat', *Journal of Aircraft*, 2003, Vol. 40, No. 4, pp. 705-715.

19. Simiu, E., Scanlan, R.H., *Wind Effects on Structures*, 2nd ed., John Wiley & Sons, Inc., New York, 1986.

20. McCormick, B.W., *Aerodynamics, Aeronautics, and Flight Mechanics*, 2nd ed., John Wiley & Sons, Inc., New York, 1995.

21. Hoerner, S.F., *Fluid-Dynamic Drag*, S.F. Hoerner, New Jersey, 1958.

22. Hibbeler, R.C., *Engineering Mechanics: Dynamics*, 7th ed., Prentice-Hall, Inc., New Jersey, 1995.

23. Russell, J.B., *Performance and Stability of Aircraft*, John Wiley & Sons, Inc., New York, 1996.

24. Zhao, X., *Statics and Dynamics Simulations of a Multi-Tethered Aerostat System*, Masters Thesis, University of Victoria, Victoria, British Columbia, 2004.

25. Torchinsky, S., 2005 January 6, 'Arecibo Performance Metrics', [Personal Email], Accessed 2005 January.

26. Puget Sound Rope, <http://www.psrope.com/psrope/>, Accessed 2005 January.

27. Evans, J.P., *Dynamics Modeling and Performance Evaluation of an Autonomous Underwater Vehicle*, Masters Thesis, McGill University, Montreal, Quebec, Canada, 2003.